Unexpected Spin Echoes in Dipolar Solids: Intrinsic Effects of Finite Pi Pulses on Quantum Coherence

A Dissertation
Presented to the Faculty of the Graduate School
of
Yale University
in Candidacy for the Degree of
Doctor of Philosophy

by
Dale Li

Dissertation Director: Professor Sean E. Barrett

December 2007

Abstract

Unexpected Spin Echoes in Dipolar Solids:
Intrinsic Effects of Finite Pi Pulses on Quantum Coherence

Dale Li

2007

This doctoral dissertation is a detailed examination of the effects of strong π pulses applied to a large system of spin-1/2 nuclei. Nuclear magnetic resonance experiments in a variety of dipolar solids are shown to defy conventional expectations set by the delta-function pulse approximation. Observed effects include multiple π-pulse echo trains with measurable coherence well beyond the expected T_2 for short delays between pulses, an even-odd asymmetry in the echo amplitudes where even-numbered echoes are larger than odd-numbered echoes for long delays between pulses, a fingerprint pattern in the echo train for intermediate delays between pulses, and a strong dependence of the echo train decay rate on the π pulse phase.

Many advanced pulse sequences and proposed quantum algorithms frequently rely on the delta-function pulse approximation to describe how a spin system evolves under the action of many pulses. In particular, it is assumed that π pulses do not refocus the dipolar coupling. However, the action of the system's internal Hamiltonian during a real finite pulse opens new coherence transfer pathways that lead to the observed effects. Visualization of the entire density matrix shows a unique flow of quantum coherence from non-observable to observable cells when applying repeated π pulses. This work uses Average Hamiltonian theory, combined with exact quantum calculations, to show that the pulse power required to approximate a real pulse as a delta-function pulse appears to be arbitrarily large and depends on the system size, spin-spin coupling strength, rapidity of applied pulses, and the spread of local magnetic fields.

For my grandmother

張群妹

(1904-2007)

and my parents

黎登全

何翠珠

Contents

List of Figures

List of Tables

Words of Acknowledgment

Conventionally, it is the graduate student's habit of writing this section on the very last day before official submission and after all the interested readers have already been overly subjected to the entire dissertation's idiosyncratic nuances. I choose not to make that mistake and offer here some acknowledging words for the people to whom I am deeply indebted while they may still be inclined to read them. At the end, I leave space for comments from my dissertation committee about physics or anything else.

It has taken me close to seven years to prepare the work associated with this manuscript. Most of the time was spent with my advisor and fellow graduate students constructing and deconstructing our view of the accumulating data as we faced a constant uphill battle to present the merits of our work. NMR specialists at every conference that we attended had no shortage of questions and impassioned arguments about why "everything is already understood". It didn't feel good to think that my work was irrelevant while many of my colleagues had such outstanding cutting-edge research.

While the impressions I received at my first March Meeting in 2002 were of genuine intrigue at the thought of finding something puzzling to do with quantum coherence, over the years, the general consensus degenerated to more and more overall skepticism about our experimental methods. These concerns were legitimate and consumed most of my scientific work on the subject stemming from my own disbelief that something could take so long to reason out without being some kind of naïve flaw in the experiments themselves. At many times I wanted to throw in the towel to work on something else that would yield a new skill or at least a less controversial result to make me more desirable in the job market.

It was Sean's true expertise and unwavering tenacity that inspired us all to continue our research when the rest of the scientific community whispered words like "uninteresting"

and “simplistic”. I remember manning a poster at the Gordon Conference one year, fielding a scientific barrage of questions from skeptics, all the while wishing that Sean would hurry up and relieve me of my duties so that I could retreat to lick my wounds. Sure enough, Sean arrived to gently quell the brewing mob. Sometimes it felt as though he was training me in self-reliance. I truly admire Sean’s patience and kind spirit that so easily wins over even the staunchest pundits. But above all, I admire Sean’s diligence to his students and his uncompromising support.

In addition, I’m lucky to have been mentored by my favorite Russian of all time, Anatoly Dementyev. His calm nature and depth of knowledge is refreshingly understated and always seemed to put me at ease. From Tolya I acquired necessary strengths in physics and in life.

Rona Ramos and Yanqun Dong came into the lab at roughly the same time and are genuine blessings to our group. Our lab dynamic became a family as we struggled together with the many facets of our research. I felt proud to be able to teach anything that I could and equally proud to learn an immeasurable amount from them in return.

At Yale, undergraduate research would often times cross paths with our lab by the way of the undergraduate senior project. It was very rewarding to be able to interact with so many bright young students. In particular Kenny MacLean and John Murray were of the brightest. They’re hard work brought significant contributions to our projects. I am grateful also for their friendship.

There was a fair share of support for our work within our own community from my colleagues as well as from professors Steven Girvin, Kurt Zilm, and Jack Sandweiss. Without their well-informed opinions and mutual respect, this work would have remained unfinished. Additionally, we had many visitors to our lab who graciously took the time to see all of our evidence and slowly allowed us to change their minds about what is or isn’t expected.

Though the mind is one of the most difficult things to change, that truly rare event is, in my opinion, the most beautiful experience.

Sincerely,

Dale Li

COMMENTS:

Chapter 1

The Basic Problem

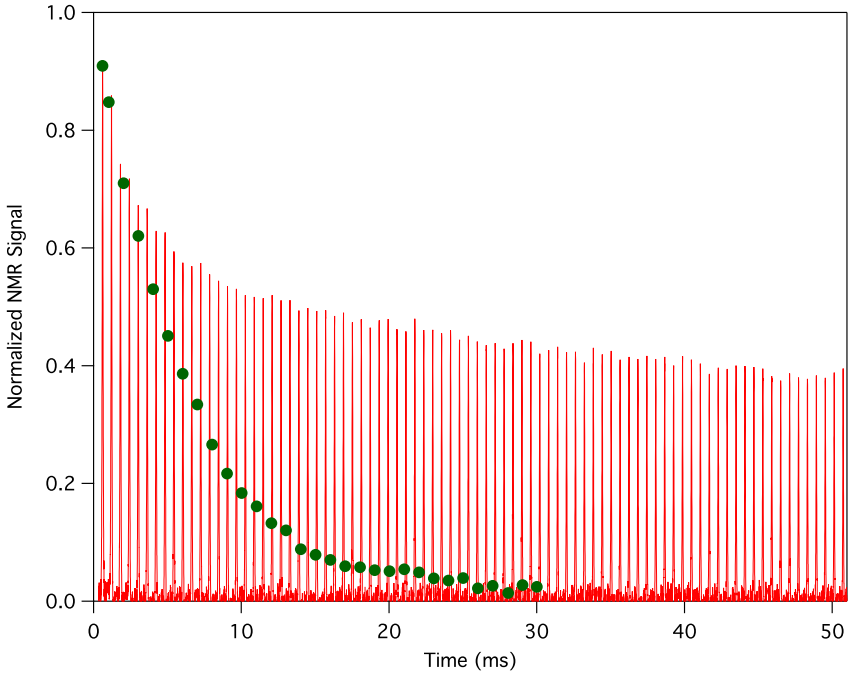

In the most general sense, this thesis is concerned with the experimental observation and subsequent theoretical explanation of the discrepancy between the two trends shown in the above graph. Both the green dots and the peaks of the red trace are expected to agree from well-established principles of nuclear magnetic resonance. It is clear, however, that they do not. In order to appreciate the significance of this discrepancy some background about how it is measured and what is expected fills a considerable portion of this work. Also presented is a preponderance of supporting experiments that attempt to correct extrinsic sources of

imperfection or find external dynamics that could be responsible. These supporting experiments have shown that the effects are universal among spin-1/2 systems (and possibly in pseudo-spin systems) and insensitive to many experimental parameters.

The different trends represent two standard measures of the transverse spin relaxation time T_2. Initially we proposed to measure T_2 in one sample as a simple first step to understanding the principles of decoherence in other materials. However, the striking difference between the two trends required an explanation. This discrepancy may have occasionally been observed in other work but attributed to experimental imperfections or to the difficulty achieving strong enough pulses. While it is certainly possible to produce similar looking graphs by introducing such imperfections, many experimental improvements that are currently achievable have not made the effect disappear.

This basic problem relates to quantum control because the two sets of data in the above graph are generated by π pules. These π pulses are ubiquitous in the design of quantum algorithms for use in a quantum computer. For example, bang-bang control sequences consisting of repeating blocks of π pulses have been proposed to help isolate a spin system from its environment [93]. Furthermore, the nuclear spin system studied here can be considered an ideal system of many qubits where the magnetic coupling between spins serves as the entanglement process. Therefore, these nuclear magnetic resonance experiments provide a forward test of the most fundamental principles that are being built upon in the emerging field of quantum information processing.

In particular, this thesis finds that the application of many real π pulses (red peaks) to a large spin system has completely different effects than applying a single π pulse (green dots) to the same system. Most surprisingly, these finite pulse effects are not perturbative. That is, no small correction to the conventional expectations can predict the correct behavior.

To solve the problem, average Hamiltonian theory was applied to this new regime of strong but finite pulses. From this theoretical work, an understanding of quantum coherence transfer pathways led to the discovery that the coupling between spins is a large-scale many-body effect that cannot be ignored even during the fastest realizable pulses. This result is entirely new and only requires either strong coupling between few neighbors, or weak coupling between many neighbors.

The following is a chapter by chapter synopsis for the reader who may wish to jump to

sections more pertinent to his/her interests:

Chapter 2 develops some simple intuitions about spin and the techniques with which to solve for its behavior. Because nuclear magnetic resonance rests on such a solid theoretical background, it is superfluous to summarize it here. For a well-written course, see reference [79]. Nevertheless, I feel compelled to offer some important guiding concepts that are frequently revisited in later chapters including the concept of precession, spin interactions, relaxation, superposition states, expectation value, the Bloch sphere, the density matrix, and commutability. Other theoretical concepts are presented later in the context in which they are needed.

Chapter 3 is an overview of the required tools used to perform high-resolution nuclear magnetic resonance experiments including a description of a high-field superconducting magnet, a schematic for heterodyne detection, two designs for resonant tank circuits, a description of pulse attributes, and an introduction to the Fourier transform. This thesis work did not create any new equipment, any new samples, or any new techniques of measurement. The results of this thesis can be obtained from the careful application of basic tools and principles of magnetic resonance or even in analogous systems with the same Hamiltonian.

Chapter 4 presents the many puzzling experiments with π pulses that originally inspired this thesis. In addition to the discrepancy between the trends of the green dots and red peaks, observed effects include an even-odd asymmetry between the heights of even-numbered echoes and odd-numbered echoes when τ becomes large, a repeating fingerprint in subsets of the echo train for intermediate τ, and a sensitivity of the echo train to π pulse phase. In the initial phase of discovery, many experiments were performed that examined different aspects of the puzzle. This thesis focuses of the few experiments that yielded the most repeatable and most pronounced effects. In addition, this chapter describes some three-pulse experiments that produced strikingly unexpected results, but unfortunately did not lead to a deeper understanding of the source cause for the effects.

Chapter 5 outlines methods of calculating the evolution of the measurable coherence using the delta-function pulse approximation and the Zeeman and dipolar Hamiltonians. Using these approximations, the experiments that produce the two trends in the first figure are expected to decay identically. This chapter quantifies the conventional expectations for

delta-function π pulses.

Chapter 6 details many experiments that explore extrinsic effects in the pulse quality and the total system Hamiltonian. These experiments helped to develop an understanding the real pulse as it differs from the idealized delta-function pulse. Studies include analysis of the nutation experiment, tests of rf field inhomogeneity, measurement of pulse transients, dependence of effects on pulse strength, and improvements through composite pulses.

Chapter 7 details more experiments that search for contributions to the system's free-evolution besides the dipolar coupling and Zeeman interaction. These studies include non-equilibrium effects, temperature effects, different systems of spin-1/2 nuclei, a single crystal, and magic angle spinning.

Chapter 8 presents a series of exact calculations using the constraints imposed by the the many experiments of Chapters 6 and 7. The first attempt at simulating the observed results because the calculations involved a small number of spins with the weak natural coupling of silicon. Because many experiments were performed in other dipolar solids, we attempted to simulate the observed effects using much stronger couplings. These calculations qualitatively reproduced the long-lived coherence and the sensitivity on π pulse phase.

Chapter 9 presents more analytical calculations seeking insight into the physics of the exact calculations. The pulse sequences are analyzed using average Hamiltonian theory. From this analysis, special terms are identified that contribute to the extension of measurable coherence in simulations with strong but finite pulses. Furthermore, the echo train tail height is sensitive to the total number of spins that are included in the calculation. This dependence on system size suggests that real pulses applied to a macroscopic number of spins may lead to the observed behaviors.

Chapter 10 visualizes the entire density matrix to show the effects of the new terms identified in Chapter 8. Regions of the density matrix that are normally inaccessible in the delta-function pulse approximation are connected to the measurable coherence by novel quantum coherence transfer pathways that play an important role in the long-lived tail.

Chapter 11 explores possible ways to exploit the behavior of the many spin system during multiple finite pulses. We present multiple pulse analogies of the Hahn echo and the Magic echo. Future work in this area is currently underway to include pulse sequences engineered for imaging research.

Chapter 12, in conclusion, presents a summary of the implications of this work for quantum computation. Quantum algorithms in the future will need to take into account the always-on interactions between qubits or find a clever way of setting the interactions identically to zero during pulses.

This work involved close collaboration with other members of the lab who made crucial contributions to the understanding of the problem. With pleasure, I will try to highlight their specific contributions in this thesis where appropriate.

Chapter 2

Spin Control

What is spin? In the context of this thesis, "spin" refers to intrinsic quantized angular momentum, but the ordinary notion of spinning objects is not an entirely ill-suited analogy. This introduction to magnetic resonance spectroscopy begins with the common intuitions of spin in the tangible macroscopic world to help describe those elusive properties in the intangible microscopic world.

While, ultimately, the solution to the basic problem of Chapter 1 requires a quantum description as introduced in section 2.3 and detailed in Chapters 5, 8, and 9, the classical equations of motion described in this section are useful in determining the general aspects of spin control.

2.1 Classical Precession and Relaxation

Edward Mills Purcell and Felix Bloch won the Nobel Prize in physics in 1952 for their independent discovery of Nuclear Magnetic Resonance (NMR). Since then the study of nuclear spins has led to tremendous developments in medical imaging as well as local probes of condensed matter physics problems. Many wonderful introductory texts describe the basic theories of NMR in great detail. For example, see references: [1, 23, 79]. In this thesis, a variety of supporting experiments and calculations are presented with their guiding principles as they are needed. Thus, instead of presenting the full gamut of NMR theory at the outset, let us only build an intuition of magnetic resonance with the familiarity of the spinning top.

The natural tendency of a top-heavy object, such as a toy top, is to fall over due to gravity.

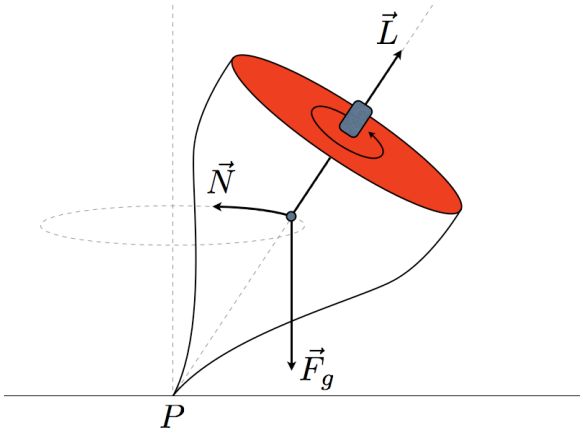

Figure 2.1: A spinning top obeys the classical laws of motion by precessing in a cone. Important parameters are the angular momentum $\vec{L}$, the force due to gravity $\vec{F}_g$, and the torque $\vec{N}$. All vectors are drawn from the top's center of mass. The vector between the pivot point P and the center of mass is $\vec{r}$ (not shown).

Without spinning, it is virtually impossible to stand the top on its base point P (See Figure 2.1). Set it spinning, though, and the top seems to defy gravity as it stands on a table. The force of gravity has not vanished, it still acts on the spinning top, but with a different result.

We can describe the natural tendencies of the spinning top by employing the basic laws of mechanics introduced by Sir Isaac Newton. Newton's second law states that the force acting on any free body is equal to its change in momentum. This law can be extended to spinning objects by setting the *torque* equal to the change in *angular momentum*.

$$\vec{N} = \frac{d\vec{L}}{dt} \tag{2.1}$$

For a toy top, the spin angular momentum vector $\vec{L}$ is aligned along its symmetry axis as shown in Figure 2.1. Therefore, equation (2.1) describes how the spinning top will move as it struggles to maintain balance. In the case of a classical top, the force of gravity $\vec{F}_g$ generates the torque

$$\vec{N} = \vec{r} \times \vec{F}_g \tag{2.2}$$

where $\vec{r}$ is parallel to $\vec{L}$ and points from P to the center of mass. The direction of the torque $\vec{N}$ is perpendicular to both $\vec{F}_g$ and $\vec{L}$ (Figure 2.1). Since the angular momentum $\vec{L}$ follows $\vec{N}$ according to equation (2.1), the spinning top will precess in a cone about its pivot point P as shown in Figure 2.1.

This notion of precession is the same for a magnetic dipole moment $\vec{\mu}$ in a magnetic field $\vec{B}$. The magnetic field generates a torque on $\vec{\mu}$ much in the same way that gravity generates a torque on the spinning top. However, in the case of magnetic fields, the force is always perpendicular so that

$$\vec{F}_B = (\vec{\mu} \times \vec{\nabla}) \times \vec{B} \tag{2.3}$$

where $\vec{\nabla}$ is the differential operator in space. This force results in a torque after suitable integration[1].

$$\vec{N}_B = \vec{\mu} \times \vec{B} \tag{2.4}$$

For an idealized dipole, its total angular momentum $\vec{J}$ is related to its magnetic dipole moment through the gyromagnetic ratio γ.

$$\vec{\mu} = \gamma \vec{J} \tag{2.5}$$

Putting all of these together we obtain the equation of motion for an isolated magnetic dipole moment in a magnetic field that is not too different from the toy model.

$$\frac{d\vec{\mu}}{dt} = \gamma(\vec{\mu} \times \vec{B}) \tag{2.6}$$

Equation (2.6) is the basis of classical spin control. We rely on this simple description for the general behavior of spins such as in Figures 4.6 and 4.9. For control, the experimentalist manipulates the strength and direction of $\vec{B}$, which changes the precessional behavior of $\vec{\mu}$ accordingly. For the experiments described in this thesis, a strong externally applied field of order 10 Tesla (1 Tesla = 10^4 Gauss) is fixed along $\hat{z}$ while a perturbative oscillatory field of order 10$\sim$1000 Gauss may be additionally applied in the xy-plane.

Because the externally applied magnetic field $\vec{B} = B^{\text{ext}}\hat{z}$ is so much larger than the perturbing field, it is convenient to transform to a frame rotating about the z-axis where the $\hat{x}$ and $\hat{y}$ coordinate vectors rotate with angular velocity $\vec{\omega} = -\omega_0 \hat{z}$

$$\frac{d\hat{x}}{dt} = \vec{\omega} \times \hat{x} \tag{2.7}$$

$$\frac{d\hat{y}}{dt} = \vec{\omega} \times \hat{y}. \tag{2.8}$$

[1]Actually, the full derivation of the force and torque on a magnetic dipole moment in a magnetic field requires a rather tedious multipole expansion inside the integrand, which I have selectively swept under the rug. See Jackson's graduate text in eletrodynamics [33].

Then equation (2.6) becomes

$$\frac{\delta\vec{\mu}}{\delta t} = \vec{\mu} \times (\gamma B^{\text{ext}} - \omega_0)\hat{z} = \vec{\mu} \tag{2.9}$$

where $\omega_0 = \gamma B^{\text{ext}}$ is the *Larmor precession frequency*, named after Sir Joseph Larmor, and the time derivative $\frac{\delta}{\delta t}$ is taken in the rotating frame. The sense of the rotation is dependent on the sign of γ.

Equation (2.9) states that a magnetic dipole moment $\vec{\mu}$ is stationary in the rotating frame so long as the only applied magnetic field is the external magnetic field. Chapter 3 will describe the application of additional magnetic fields in the rotating frame that act to change the direction of $\vec{\mu}$.

In NMR experiments we measure the total magnetization of an object, which is the vector sum of all the nuclear magnetic dipole moments.

$$\vec{M} = \sum_{i=1}^{N} \vec{\mu}_i \tag{2.10}$$

Typically, the polarization of nuclei reaches about $10^{-5}\sim10^{-6}$ in a 10 Tesla field. In many respects, the total magnetization behaves like a simple magnetic dipole moment. However, in NMR measurements, the macroscopic magnetization usually decays in a process called *spin relaxation*.

The process of spin relaxation can be considered phenomenologically by introducing a new term in each component of the torque equation for the magnetization.

$$\frac{dM_z}{dt} = \gamma(\vec{M} \times \vec{B})_z - \frac{M_z - M_0}{T_1} \tag{2.11}$$

$$\frac{dM_x}{dt} = \gamma(\vec{M} \times \vec{B})_x - \frac{M_x}{T_2} \tag{2.12}$$

$$\frac{dM_y}{dt} = \gamma(\vec{M} \times \vec{B})_y - \frac{M_y}{T_2} \tag{2.13}$$

Equations (2.11), (2.12), and (2.13) are commonly referred to as the Bloch equations where the magnetization is given by the three-component vector $\vec{M} = (M_x, M_y, M_z)$ and the relaxation times are given by T_1 and T_2. Note that as time progresses, the magnetization in the transverse plane (xy-plane) tends to decay to zero while the magnetization along the z-axis tends to return to its equilibrium value M_0.

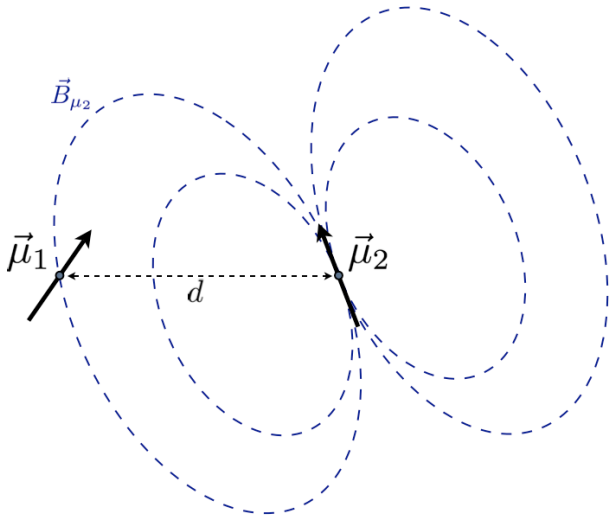

Figure 2.2: The magnetic field produced by $\vec{\mu}_2$ affects the motion of $\vec{\mu}_1$ and vice versa.

T_1 is referred to as the *spin-lattice relaxation time* and results from interactions between nuclei and their environment. These interactions serve to relax the nuclear spins so that they eventually align with the external field. In this thesis, T_1 times range from seconds to hours. The other relaxation time, T_2, is referred to as the *transverse relaxation time* because it is perpendicular to the external magnetic field. Unlike spin-lattice relaxation, transverse relaxation results from spin-spin interactions that conserve the total energy of the system. Measured values of T_2 are typically in the range of milliseconds.

This thesis focuses on the underlying dynamics that cause T_2, particularly in the presence of applied pulses of magnetic fields. In terms of measurement, equations (2.11)-(2.13) qualitatively predict the the correct behavior of the macroscopic magnetization $\vec{M}$. However, the underlying dynamics of T_2 require a quantum mechanical description. First, let us develop our classical intuitions a bit further to understand how the interaction between spins can lead to decay.

2.2 Classical Interaction of Magnetic Moments

Consider just two magnetic dipole moments $\vec{\mu}_1$ and $\vec{\mu}_2$ a distance d apart as shown in Figure 2.2. We can describe the effect that $\vec{\mu}_2$ has on $\vec{\mu}_1$ by noting that a magnetic dipole moment produces its own local magnetic dipole field.

The total effective magnetic field experienced by $\vec{\mu}_1$ is obtained by adding the small local magnetic field induced by $\vec{\mu}_2$ to the large external magnetic field $\vec{B}$. Then by equation (2.6), $\vec{\mu}_1$ will precess about this total effective magnetic field. However, to complicate matters, this local magnetic field changes in time as $\vec{\mu}_2$ precesses. Even worse, the motion of $\vec{\mu}_2$ is determined in part by the motion and subsequent magnetic field of $\vec{\mu}_1$.

The detailed balance of all of these dynamics is a daunting task. An elegant method for solving the behavior of the entire system involves the quantum mechanical description of spin. As a feature, the quantum description includes properties such as superposition that are not possible classically. Even so, the classical description fails to describe measurements of a single spin [71] or when the interaction between spins creates unobservable coherence states. We describe these unobservable coherence states and their relevance to measurable quantities further in Chapter 10.

2.3 The Quantum Description of Spin

The quantum mechanical description begins by considering transitions of the magnetic dipole moment between two energy states. The state where $\vec{\mu}$ points in the same direction as $\vec{B}$ is called *spin up* and denoted as $|\uparrow\rangle$, while the opposite direction is called *spin down* and denoted as $|\downarrow\rangle$. In addition, any linear combination of the two spin states may be written as

$$|\psi\rangle = \cos(\theta/2)\ |\uparrow\rangle + \mathrm{e}^{i\phi} \sin(\theta/2)\ |\downarrow\rangle \tag{2.14}$$

where the coefficients are chosen to enforce the normalization condition $\langle\psi|\psi\rangle = 1$ in Wolfgang Pauli's "bra-ket" notation [74]. Equation (2.14) represents the *superposition state* of a single spin.

The physical interpretation of the spin state $|\psi\rangle$ requires a mapping back to an observable quantity. This mapping is achieved by introducing the dimensionless three component spin angular momentum operator $\vec{I} = (I_x, I_y, I_z)$, parallel to the magnetic dipole moment.

$$\vec{\mu} = \gamma\hbar\vec{I} \tag{2.15}$$

The symbol $\hbar$ is Planck's constant divided by 2π, named after Max Planck who first described the theory of quantization. The appearance of $\hbar$ usually means that some quantity

in the equation only takes on discrete values. In this case, it is the spin angular momentum that is quantized.

By quantizing the spin angular momentum, the spin state is projected onto a particular axis with a fixed set of possible values. For example, if the external magnetic field is aligned along $\hat{z}$, then operating I_z on the spin up state yields the eigenvalue equation

$$I_z \left|\uparrow\right\rangle = m_z \left|\uparrow\right\rangle \tag{2.16}$$

where m_z is the projection of the spin state $|\uparrow\rangle$ onto the z-axis. For the case considered here, $m_z = +1/2$ for spin up and $m_z = -1/2$ for spin down, allowing only two possible states.

To project the state onto the x-axis and y-axis, the ladder operators are defined

$$I^+ = I_x + iI_y \tag{2.17}$$

$$I^- = I_x - iI_y \tag{2.18}$$

where

$$I^+ \left|\uparrow\right\rangle = 0 \tag{2.19}$$

$$I^+ \left|\downarrow\right\rangle = \left|\uparrow\right\rangle \tag{2.20}$$

$$I^- \left|\uparrow\right\rangle = \left|\downarrow\right\rangle \tag{2.21}$$

$$I^- \left|\downarrow\right\rangle = 0. \tag{2.22}$$

With these definitions for the spin angular momentum operators, we may calculate the expectation values that give the observable quantities

$$\langle I_x \rangle = \langle \psi | I_x | \psi \rangle = \frac{1}{2} \sin(\theta) \cos(\phi) \tag{2.23}$$

$$\langle I_y \rangle = \langle \psi | I_y | \psi \rangle = \frac{1}{2} \sin(\theta) \sin(\phi) \tag{2.24}$$

$$\langle I_z \rangle = \langle \psi | I_z | \psi \rangle = \frac{1}{2} \cos(\theta) \tag{2.25}$$

so that the classical magnetic dipole moment is recovered as

$$\langle \vec{\mu} \rangle = \gamma \hbar \langle \vec{I} \rangle = \gamma \hbar (\langle I_x \rangle \hat{x} + \langle I_y \rangle \hat{y} + \langle I_z \rangle \hat{z}) \tag{2.26}$$

Conveniently, θ and ϕ are well-suited to represent angles in a conceptual *Bloch Sphere* [79] as depicted in Figure 2.3. Spins trace a path along the surface of the Bloch Sphere

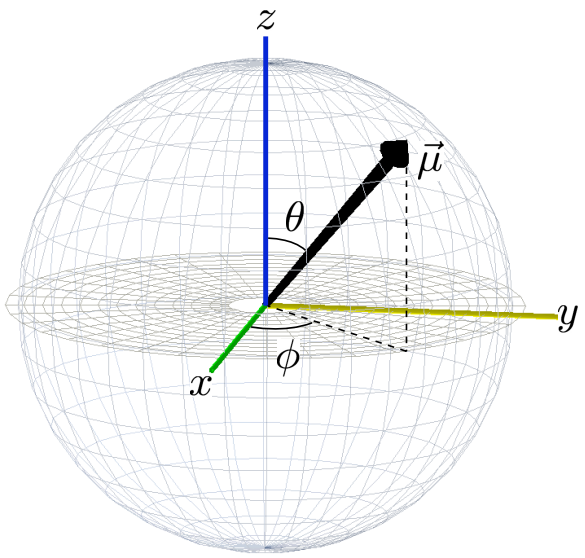

Figure 2.3: The Bloch Sphere representation of a magnetic dipole moment $\vec{\mu}$. Any orientation of $\vec{\mu}$ can be described by the two phase angles θ and ϕ.

according to their expectation values $\langle I_x(t)\rangle$, $\langle I_y(t)\rangle$, and $\langle I_z(t)\rangle$. This representation is a useful tool for visualizing the general behavior of many isolated spins as we show later in Figures 4.6 and 4.9. Additionally, from the experimentalist's perspective, the Bloch Sphere allows an easy way to see how the direction of the magnetic dipole moment may be controlled with an appropriate manipulation of θ and ϕ.

With this representation, we proceed to describe the interactions of the spins with the environment and with each other. First, the tendency for a magnetic dipole moment to align with an externally applied magnetic field is represented by an energy relationship.

$$U = -\vec{\mu} \cdot \vec{B} \tag{2.27}$$

The energy U is less if the dot product $\vec{\mu} \cdot \vec{B}$ is positive, meaning that the ground state configuration has $\vec{\mu}$ and $\vec{B}$ pointing in the same direction. For a fixed magnetic field, the two spin states will have different energies. This energy splitting is called the Zeeman energy splitting after Dutch physicist Pieter Zeeman.

In quantum mechanics, the energy is converted to an operator called the Hamiltonian named after Irish mathematician Sir William Hamilton. This Zeeman Hamiltonian is written as

$$\mathcal{H}_Z = -\gamma \hbar I_z B^{\text{ext}} \tag{2.28}$$

where the magnitude of the external magnetic field is directed along $\hat{z}$.

From this Zeeman Hamiltonian of non-interacting spins, we can begin to describe the behavior of spins analogous to the classical motion as described by equation (2.6). The quantum mechanical description for the behavior of a spin state $|\psi\rangle$ is given by Schödinger's equation named after Erwin Schödinger.

$$i\hbar\frac{d}{dt}|\psi\rangle = \mathcal{H}|\psi\rangle \tag{2.29}$$

In the general case, $|\psi\rangle$ may represent the total spin state of all N spins in the system.

The solution to equation (2.29) for a constant $\mathcal{H}$ is an exponential

$$|\psi(t)\rangle = \mathrm{e}^{-\frac{i}{\hbar}\mathcal{H}t}|\psi(0)\rangle \tag{2.30}$$

where $|\psi(0)\rangle$ is the initial state ket. For example, a single spin in an external magnetic field $\vec{B} = B_0\hat{z}$ with initial state

$$|\psi(0)\rangle = \cos(\theta_0/2)\ |\uparrow\rangle + \sin(\theta_0/2)\mathrm{e}^{i\phi_0}\ |\downarrow\rangle \tag{2.31}$$

will evolve as

$$|\psi(t)\rangle = \cos(\theta_0/2)\ |\uparrow\rangle + \sin(\theta_0/2)\mathrm{e}^{i(\phi_0-\gamma B_0 t)}\ |\downarrow\rangle. \tag{2.32}$$

If we define the angular frequency

$$\omega_0 = \gamma B_0 \tag{2.33}$$

and plot the time-dependent expectation values $\langle I_x(t)\rangle$, $\langle I_y(t)\rangle$, and $\langle I_z(t)\rangle$ on the Bloch Sphere, we observe the natural precession of the spin. Namely, the spin precesses with angular frequency ω_0, the Larmor frequency, in a cone tilted at angle θ_0 with the z-axis.

Now we add the complication of interactions between spins. Generalizing equation (2.28) for magnetic fields produced by individual magnetic dipole moments yields a generalized coupling Hamiltonian

$$\mathcal{H}_c = a_{12}I_{z_1}I_{z_2} + b_{12}(I_{x_1}I_{x_2} + I_{y_1}I_{y_2}). \tag{2.34}$$

where coefficients a_{12} and b_{12} may contain many specific parameters about the orientations of the two spins and the external magnetic field B. For the special case where a_{12} is

a constant and $b_{12} = 0$, the interaction is simply the tendency for the two spins to align or anti-align in the z-direction.

Taken together, equations (2.28) and (2.34) should completely describe a closed system of spins in a magnetic field. The transverse relaxation time, T_2, can then be determined by the interactions between the spins as we describe in Chapter 4. To calculate the spin-lattice relaxation time T_1, additional external parameters about the systems environment are needed. For N total spins, the full Hamiltonian operator is written as

$$\mathcal{H} = \sum_{i=1}^{N} -\gamma\hbar I_{z_i} B + \sum_{j>i}^{N} a_{ij} I_{z_i} I_{z_j} + b_{ij}(I_{x_i} I_{x_j} + I_{y_i} I_{y_j}) \tag{2.35}$$

where the subscripts i and j denote the individual spins. To solve for the behavior of many spins at once, we use the density matrix.

2.4 The Density Matrix Representation

In this thesis, we wish to solve equation (2.29) for an ensemble of spins with many different initial states. The quantum mechanical ensemble is represented as the *density matrix*

$$\rho = \sum_{i=1}^{N} \sum_{j=1}^{N} w_{ij} |\psi_i\rangle\langle\psi_j| \tag{2.36}$$

where w_{ij} is some complex weight factor, and $|\psi_i\rangle$ is the ith possible configuration for N spins.

For example, in the z-basis with $N = 2$ spins, the density matrix is given by

$$\begin{aligned}
\rho \;=\; & w_{11} \,|{\downarrow\downarrow}\rangle\langle{\downarrow\downarrow}| + w_{12} \,|{\downarrow\downarrow}\rangle\langle{\downarrow\uparrow}| + w_{13} \,|{\downarrow\downarrow}\rangle\langle{\uparrow\downarrow}| + w_{14} \,|{\downarrow\downarrow}\rangle\langle{\uparrow\uparrow}| \\
& + w_{21} \,|{\downarrow\uparrow}\rangle\langle{\downarrow\downarrow}| + w_{22} \,|{\downarrow\uparrow}\rangle\langle{\downarrow\uparrow}| + w_{23} \,|{\downarrow\uparrow}\rangle\langle{\uparrow\downarrow}| + w_{24} \,|{\downarrow\uparrow}\rangle\langle{\uparrow\uparrow}| \\
& + w_{31} \,|{\uparrow\downarrow}\rangle\langle{\downarrow\downarrow}| + w_{32} \,|{\uparrow\downarrow}\rangle\langle{\downarrow\uparrow}| + w_{33} \,|{\uparrow\downarrow}\rangle\langle{\uparrow\downarrow}| + w_{34} \,|{\uparrow\downarrow}\rangle\langle{\uparrow\uparrow}| \\
& + w_{41} \,|{\uparrow\uparrow}\rangle\langle{\downarrow\downarrow}| + w_{42} \,|{\uparrow\uparrow}\rangle\langle{\downarrow\uparrow}| + w_{43} \,|{\uparrow\uparrow}\rangle\langle{\uparrow\downarrow}| + w_{44} \,|{\uparrow\uparrow}\rangle\langle{\uparrow\uparrow}|
\end{aligned} \tag{2.37}$$

and can be written in mattrix form as

$$\rho = \begin{pmatrix} w_{11} & w_{12} & w_{13} & w_{14} \\ w_{21} & w_{22} & w_{23} & w_{24} \\ w_{31} & w_{32} & w_{33} & w_{34} \\ w_{41} & w_{42} & w_{43} & w_{44} \end{pmatrix}. \tag{2.38}$$

As we will discuss further in Chapter 10, terms in different parts of the density matrix represent different quantum coherences of the total system. Special mechanisms will be discussed in Chapter 9 that connect different quantum coherences together to allow mixing in the density matrix.

Using the density matrix, equation (2.29) may be rewritten to the quantum mechanical form of Liouville's theorem, named after French mathematician Joseph Liouville,

$$i\hbar\frac{d}{dt}\rho = [\mathcal{H}, \rho] \tag{2.39}$$

where the brackets denote the quantum mechanical commutator [74].

The solution of equation (2.39) for a constant $\mathcal{H}$ is the exponential equation

$$\rho(t) = \mathrm{e}^{-\frac{i}{\hbar}\mathcal{H}t}\rho(0)e^{+\frac{i}{\hbar}\mathcal{H}t} \tag{2.40}$$

analogous to equation (2.30).

The observable expectation values are derived from the density matrix as follows

$$\langle I_x\rangle = \mathrm{Tr}[\rho(t)I_x] \tag{2.41}$$

$$\langle I_y\rangle = \mathrm{Tr}[\rho(t)I_y] \tag{2.42}$$

$$\langle I_z\rangle = \mathrm{Tr}[\rho(t)I_z] \tag{2.43}$$

where Tr denotes the matrix trace. The matrix form of the spin angular momentum operators are generated using the identity operator in ket-bra notation. For example, the ith row, $j$column of the matrix form for I_x is given by

$$I_{x_{ij}} = |\psi_i\rangle\langle\psi_i|I_x|\psi_j\rangle\langle\psi_j|. \tag{2.44}$$

Lastly, an important bit of information is the non-communtability of each component spin angular momentum operator.

$$[I_x, I_y] = iI_z \tag{2.45}$$

$$[I_y, I_z] = iI_x \tag{2.46}$$

$$[I_z, I_x] = iI_y \tag{2.47}$$

Non-commutability is an important aspect of quantum dynamics since the right side of equation (2.39) would be zero if the Hamiltonian commuted with the density matrix at

any point. In other words, if two operators do not commute, that is, there are no mutual eigenstates of both operators, then the action of one will always affect the state of the other. We find this to be the case for the operation of real pulses on interacting spins.

This chapter focused on the intuitive notion of spin precession as a method of spin control in NMR and gently introduced some general elements needed for the quantum description of an ensemble of spins. In later chapters these concepts are further developed for use in theoretical calculations that describe the conventional expectations of instantaneous pulses and even more calculations that introduce average Hamiltonian theory to describe our experimental data.

Chapter 3

NMR Tools

Armed with the basics of NMR theory, it makes good sense to test those principles in the real world. After all, nature surprises us the most when we find something different from what we expect. Some specialized equipment is needed to ensure precision, accuracy, and control.

3.1 A Superconducting Magnet

High resolution NMR requires the application of a strong external magnetic field that is homogeneous to less than one part in a million over the volume of the spin system under study. With such a homogeneous external magnetic field, the local field variations within a spin system are easily resolved over a macroscopic sample volume. We achieved this high quality magnetic field using a type II superconducting magnet.

The experiments described in this thesis were performed on an Oxford Instruments Teslatron. Table 3.1 summarizes the attributes of the Teslatron superconducting magnet.

One special feature of a superconducting magnet is the ability to operate in the persistent current mode. Because the magnet is superconducting, current will flow with zero resistance when the superconducting material is cooled below the critical temperature. In the case of Nb_3Sn, the critical temperature is well above the boiling point of liquid helium so that conventional cryogens are used to cool the magnet.

In the persistent current mode, the magnetic field is extremely stable. The Oxford Teslatron has a maximum attainable field of 12.0 Tesla, which is approached in two stages. Initially the target field is overshot by 0.017 Tesla and then slowly brought to the required

Attribute	Value
Maximum Central Field	12.0 Tesla
Superconducting Material	Nb_3Sn wire
Field Stability	< 0.1 ppm/hr
Operating Current	109.4 Amps at 12 Tesla
Inductance	84.9 Henries
Stored Energy	1.02 MegaJoules
Field Homogeneity	< 0.2 ppm
High Homogeneity Volume	10 mm diameter sphere
Bore Diameter	88 mm
Helium Boil-off Rate	<0.019 liters/hr
Helium Reservoir Volume	35 liters
Total Weight Empty	400 kg

Table 3.1: Oxford Instruments Teslatron Superconducting NMR Magnet

field after a 20 minute wait period. This technique ensures a field drift of less that 0.1 parts per million per hour.

Other target field values have been attained with the Oxford Teslatron including 1 Tesla, 3 Tesla, and 7 Tesla. Each of these target field values are approached in a similar manner prescribed above.

To ensure field homogeneity over a $\sim$1 cm^3 sample volume a process called "shimming" was performed to cancel $\frac{\partial}{\partial z}$, $\frac{\partial^2}{\partial z^2}$, $\frac{\partial}{\partial x}$, $\frac{\partial}{\partial y}$, $\frac{\partial^2}{\partial x \partial y}$, $\frac{\partial^2}{\partial x^2}$, and $\frac{\partial^2}{\partial y^2}$ field gradients using the pre-installed superconducting shim coils in the Oxford Teslatron. First, spatial mapping of the magnetic field was done using the deuterium NMR signal from a $\sim$1 mm^3 droplet of D_2O in a specially designed probe. Then the six superconducting shim coils were calibrated by measuring the contribution to the total magnetic field due to a given current through each coil. Finally, the appropriate current for each shim coil was calculated and applied so that the corresponding spatial derivative would be cancelled. This procedure allowed us to achieve a $\sim$0.2 ppm magnetic field homogeneity over a $\sim$1 cm^3 sample volume at the center of the field.

3.2 Circuitry of Spectroscopy

The general schematic outline for heterodyne spectroscopic NMR detection is given in Figure 3.2. The basic idea is to apply a square pulse of oscillating magnetic fields at the Larmor precession frequency of the particular nucleus under study. Then detection is achieved by measuring the induced electro-motive force by the total magnetic moment of the nuclei in the sample.

Both the creation of the perturbing pulse and the detection begin with a continuous wave carrier source dialed to the Larmor precession frequency of the nucleus of interest. This carrier source is "split" into two identical transmission lines, one line used to create the pulse, and the other used for detection.

To create the proper pulse, this oscillating voltage source is first attenuated with a digital attenuator that controls the height of the pulse. Next, the source is electronically gated close to a square pulse with a controllable time duration. The gated oscillating pulse is then fed into a power amplifier and then a series of crossed diodes to protect the amplifier from

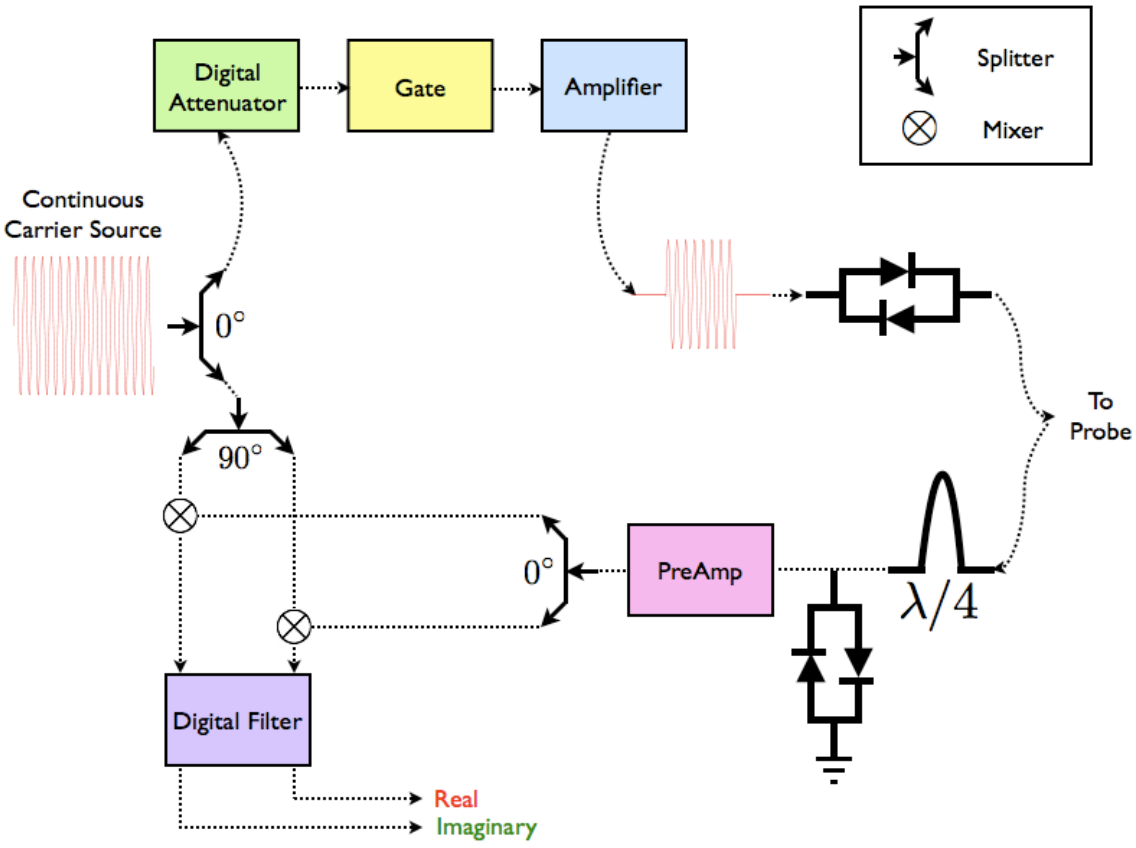

Figure 3.1: A schematic of the NMR electronics for heterodyne detection.

reflected voltage. Finally, the pulse is transmitted to the NMR tank circuit.

Immediately after the pulse is applied, detection is possible via a quarter-wavelength ($\lambda/4$) transmission line coupled to the tank circuit. The $\lambda/4$ cable acts as an impedance transformer about the characteristic circuit impedance of 50 Ohms. In other words, the high voltage of the pulse at the carrier frequency exhibits a peak voltage at the side of the tank circuit but a tiny voltage at the opposite end of the $\lambda/4$ cable. Thus, the high voltage pulse is applied to the tank circuit and not to the detection circuit while the small voltage signal induced by the sample is received predominately by the detection circuit.

Crossed diodes to ground is another protection element after the $\lambda/4$ cable. The preamplifier then amplifies the signal before proceeding to another splitter that creates a pair of duplicate signal lines. One signal line is mixed with the original carrier source. We commonly refer to this signal line as the "real channel". The other signal line is mixed with a 90° phase shifted copy of the original carrier source. This second signal line is commonly referred to as the "imaginary channel".

The actual output of the circuit mixers is the product of the two input sources. Since the original carrier source and the NMR signal are both oscillating signals, the product takes the form of the sum and difference of the two frequencies. For example, assume that the carrier has a frequency ω_a while the NMR signal has a frequency ω_b, then the mixer outputs

$$\cos(\omega_a t) \otimes \cos(\omega_b t) \rightarrow \cos(\omega_a t)\cos(\omega_b t) = \cos((\omega_a - \omega_b)t) + \cos((\omega_a + \omega_b)t) \quad (3.1)$$

If the original carrier source ω_a is set close to the natural Larmor precession frequency ω_b then $\omega_a - \omega_b \approx 0$ while $\omega_a + \omega_b \approx 2\omega_0$. By sending both the real and imaginary channels though a digital low-pass filter, we focus on detecting the difference signal. The act of subtracting out the carrier source is same as transforming to the rotating reference frame.

Two NMR tank circuit designs are depicted in Figure 3.2. The choice of circuit to use depends on the desired resonance frequency. Both circuit designs feature two tunable capacitors with variable capacitances C_T for the tuning capacitor and C_M for the matching capacitor. These two capacitors are used to tune the NMR tank circuit to the desired resonance frequency while maintaining the total impedance of the circuit at 50 Ohms.

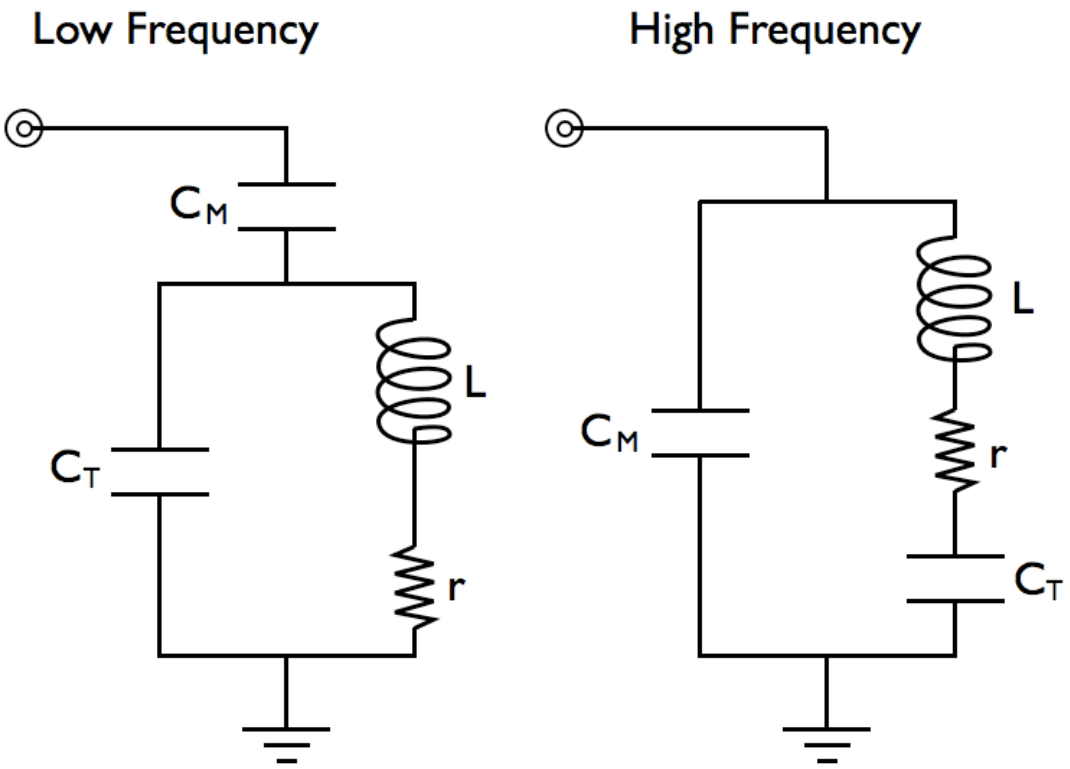

Figure 3.2: Two NMR tank circuit designs for low frequency (< 50 MHz) resonance and high frequency (> 50 MHz) resonance. The NMR sample is inserted inside the copper coil with inductance L. The typical range of values is $10 \sim 100$ micro-Henries for L, $1 \sim 300$ pico-Farads for C_M and C_T, $1 \sim 5$ Ohms for r, and $10 \sim 200$ MHz for the resonance frequency. The tank circuit impedance is usually matched at 50 Ohms.

3.3 The Pulse

The NMR apparatus allows five basic controls to manipulate the nuclear spins in the sample. All of these controls are focused on the application of radio frequency (rf) pulses to the tank circuit, which are absorbed into the sample. The controls are pulse strength, pulse duration, pulse frequency, pulse phase, and the delay between pulses.

For nuclear magnetic spins, the important feature of an rf pulse is the oscillating magnetic field. Nuclear spins naturally precess about the fixed z-magnetic field supplied by the superconducting magnet but always in one sense of rotation. An rf pulse tuned at the proper Larmor precession frequency of the nuclei and applied to the NMR coil can be considered as two counter-rotating magnetic fields, which sum to give the simple linearly-polarized oscillatory field produced by the inductor L. One of these rotating magnetic fields rotates in the same sense as the nuclei in the sample and can be considered static in that rotating frame. The other rotating magnetic field rotates at twice the Larmor frequency when seen by the nuclei in their rotating frame. The *rotating wave approximation* discards this fast rotating field by noting that the time average field in the rotating frame of the nuclei is zero.

In the rotating frame of the nuclei, the spins will precess about this new magnetic field produced by the pulse just as it would precess about any other magnetic field. The pulse strength then determines how fast the spins will precess (i.e. the Rabi frequency ω_1) while the pulse duration determines how long the spins will continue to precess. Together, these two parameters determine the overall angle that the nuclear spins have changed during the action of the pulse.

Since the NMR coil is typically perpendicular to the fixed z-field of the superconducting magnet, the magnetic field generated from the rf pulses is constrained to the transverse plane. This is not a limitation if the phase of the rf pulse can be controlled. By controlling the phase, the pulses can be applied along the x-axis, the y-axis, or any angle ϕ away from the x-axis. Conventionally, pulses along $\hat{x}$ and $\hat{y}$ are sufficient to manipulate the nuclear spins to any orientation in the Bloch sphere (see Chapter 2).

Finally, the delay between pulses controls the timing when spins align with each other. When spins are aligned, this creates the biggest NMR signal because the precession of the total magnetic moment of the sample induces a voltage in the NMR coil. A spin echo occurs

when the spins align at a specified delay after a pulse.

3.4 The Fourier Transform

Perhaps the most important tool in high resolution NMR is the *Fourier Transform* named after French mathematician Baron Jean Baptiste Joseph Fourier. This unique tool allows the transformation of an observed free induction decay in the time domain to a spectrum in the frequency domain [4].

The fundamental principle of the Fourier Transform is the idea that any curve with domain $[t_1, t_2]$ may be written as an infinite series of sine and cosine functions

$$f(t) = \frac{1}{2}a_0 + \sum_{n=1}^{\infty} a_n \cos(\omega_n t) + b_n \sin(\omega_n t) \tag{3.2}$$

where $\omega_n = n\frac{2\pi}{T}$ is the nth harmonic of the function $f(t)$ with period T. The Fourier coefficients are given by

$$a_n = \frac{2}{T}\int_{t_1}^{t_2} f(t)\cos(\omega_n t)dt \tag{3.3}$$

$$b_n = \frac{2}{T}\int_{t_1}^{t_2} f(t)\sin(\omega_n t)dt. \tag{3.4}$$

From the Fourier Series, we obtain the complex Fourier Transform between the time domain and the frequency domain

$$f(t) = \frac{1}{\sqrt{2\pi}}\int_{-\infty}^{+\infty} F(\omega')\mathrm{e}^{i\omega' t}d\omega' \tag{3.5}$$

$$F(\omega) = \frac{1}{\sqrt{2\pi}}\int_{-\infty}^{+\infty} f(t')\mathrm{e}^{-i\omega t'}dt'. \tag{3.6}$$

In practice, the digitized signals are processed with an efficient algorithm called the *Fast Fourier Transfrom* (FFT) that computes the discrete Fourier Transform from of an array of complex numbers. The "real" and "imaginary" parts of $f(t)$ are produced by the phase-sensative detection used in Figure 3.1.

Figure 3.3 shows an example of the FFT from a real time resolved signal of a decaying voltage received in the NMR coil to a well-defined spectrum in frequency.

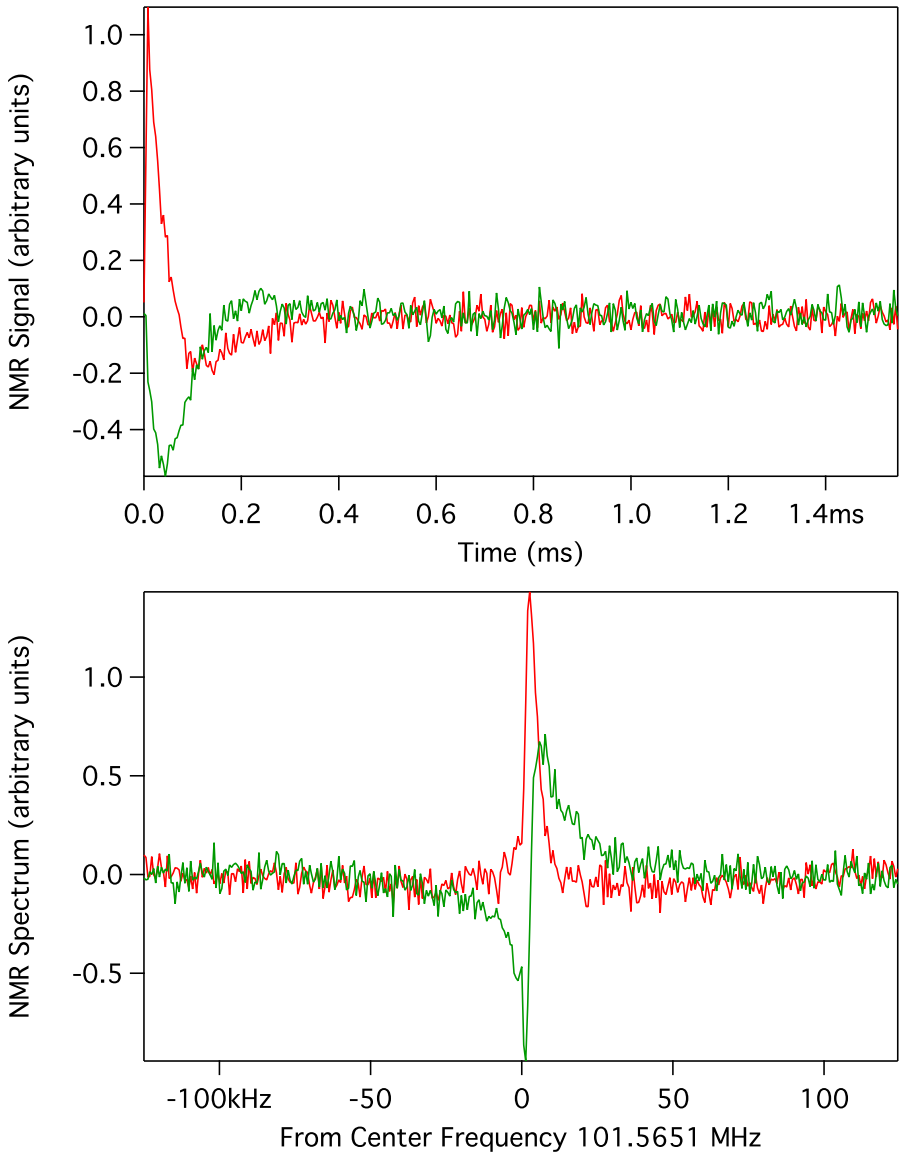

Figure 3.3: An example of the Fourier Transform applied to a free induction decay signal in time. At time $t = 0$ a 90_X pulse is applied in the rotating frame to the spin system in equilibrium. Since the NMR coil is perpendicular to the external field, it measures a decaying oscillatory voltage in the transverse direction induced by the precessing magnetic moment of the sample. Once the the carrier frequency is mixed away, the resulting NMR signal looks like the top graph. The red trace is the in-phase component (in this case, along the y-axis in the rotating frame), while the green trace is the out-of-phase component (in this case, along the $-x$-axis). The Fourier transform is applied and the characteristic shape of the spectrum in frequency is obtained in the bottom graph.

Chapter 4

Quantum Coherence Measurements

The turn of the twenty-first century saw a new branch of physics called Quantum Information Processing (QIP) gaining incredible momentum. At the heart of the study is the promise to build a device known as a quantum computer that would exploit the features of quantum mechanics in algorithms that are thought to compute the impossible [15].

Much fundamental work is needed to establish the feasibility of such a device. One important study is determining how long potential qubits can maintain a special kind of stability known as quantum coherence. For practical purposes, the quantum coherence time constrains the amount of time in which a quantum algorithm may be performed. In order to discuss this aspect further, we must make the connection between quantum computation and nuclear magnetic resonance.

4.1 Solid State Qubits

In the simplest definition a *qubit* is a quantum bit. Much like the classical notion of a computational bit, a qubit takes on one of only two possible states when measured. In analogy to spin states we shall make the assignment that the "0" state corresponds to the spin down state $|\downarrow\rangle$ while the "1" state corresponds to the spin up state $|\uparrow\rangle$.

A qubit has a special property in addition to the two measured states. This property is known as the superposition principle where the state of a qubit may actually be in a linear combination of both the spin down state and the spin up state

$$|\psi\rangle = a\,|\downarrow\rangle + b\,|\uparrow\rangle \tag{4.1}$$

where $|a|^2+|b|^2 = 1$. Furthermore, upon measuring the state of the qubit, the only possible outcomes are spin down with probability $|a|^2$ or spin up with probability $|b|^2$. This "collapse" of the state $|\psi\rangle$ to a probabilistic outcome is perhaps one of the most philosophically difficult concepts to interpret. Nevertheless, this representation gives the correct physical description.

Another property known as *entanglement* is thought to be important for the development of a quantum computer. Two spins are entangled when their total state ket cannot be represented as a product state of the two individual spins. For example, the two-spin singlet state is given by

$$|\psi_s\rangle = \frac{1}{\sqrt{2}}(|\downarrow\uparrow\rangle - |\uparrow\downarrow\rangle) \tag{4.2}$$

where the arrow on the left represents the state of the first spin while the arrow on the right represents the state of the second spin.

The two spins in the singlet state are considered entangled since the measurement of only the first spin uniquely determines the state of the second spin and vice versa. The measurement of each spin will yield either spin up or spin down with equal probability, but there is a perfect anti-correlation between the two spins.

It makes sense, maybe in an anthropomorphic way, that entanglement is only possible if the two qubits have shared an interaction (either direct or indirect) in at least one point in their history. To further the analogy with spins, the interaction between two magnetic dipole moments can serve to establish such an entanglement.

Many other entanglement schemes are possible between two quantum objects such as electrons in quantum Hall effect materials, electrons in quantum dots, electrons in the superconducting state, an array of trapped atoms, or nuclear spins in semiconductors. An important attribute that determines feasibility of any of these schemes is the scalability of the qubit system. For this reason, solid state qubits have been at the forefront of many QIP studies.

4.2 Measuring the Transverse Relaxation Time in Two Ways

The *quantum coherence time* gives the length of time that the state of a qubit will evolve as expected. As an analogy, we may think of the state of a qubit as the hour-hand on a clock.

Then if we start the clock at 1:00 and come back 2 hours later, we should expect to observe that the hour-hand has advanced to 3:00. If the time is wrong or if the hour-hand is missing, then the coherence time has been exceeded.

In the nuclear spin system, an important mechanism that contributes to the coherence time is the interaction between spins. Thus, the transverse relaxation time, or T_2, is an accepted measure of coherence time in NMR.

We initially set out to measure the transverse spin relaxation time T_2 for both ^{31}P and ^{29}Si in silicon [3, 24, 40, 78, 82] doped with phosphorous, motivated by proposals to use spins in semiconductors for quantum computation [15, 34, 35, 38, 65, 94]. In doing so, we discovered a startling discrepancy between two standard methods of measuring T_2 using the NMR spin echo [79].

The first method is the Hahn echo (HE), where a single π pulse is used to partially refocus magnetization [29].

$$\mathrm{HE}: \quad 90_X - \tau - 180_Y - \tau - \mathrm{echo}$$

The pulses are represented as their intended rotation angle with their phase as subscripts. For this sequence, each Hahn echo [Figure 4.1(green dots)] is generated with a different time delay τ.

The second method is the Carr-Purcell-Meiboom-Gill (CPMG) echo train [9, 58]

$$\mathrm{CPMG}: \quad 90_X - \tau - \{180_Y - \tau - \mathrm{echo} - \tau\}^n$$

where the block in brackets is repeated n times for the nth echo. Note that CPMG is identical to HE for $n = 1$. In contrast to the series of Hahn echo experiments, the CPMG echo train [Figure 4.1(red lines)] should give T_2 in a single experiment.

As Figure 4.1 shows, the T_2 inferred from the echo decay is strikingly different depending on how it is measured. Admittedly, two different experiments that give two different results is not uncommon in NMR. In fact, in liquid state NMR, the CPMG echo train is expected to persist after the Hahn echoes have decayed to zero. In the liquid state, spins can diffuse to different locations in a static inhomogeneous magnetic field [9, 22, 79]. This diffusion leads to a time-dependent fluctuation in the local field for individual spins, which spoils the echo formation at long τ. By rapidly pulsing a liquid spin system, it is possible to render

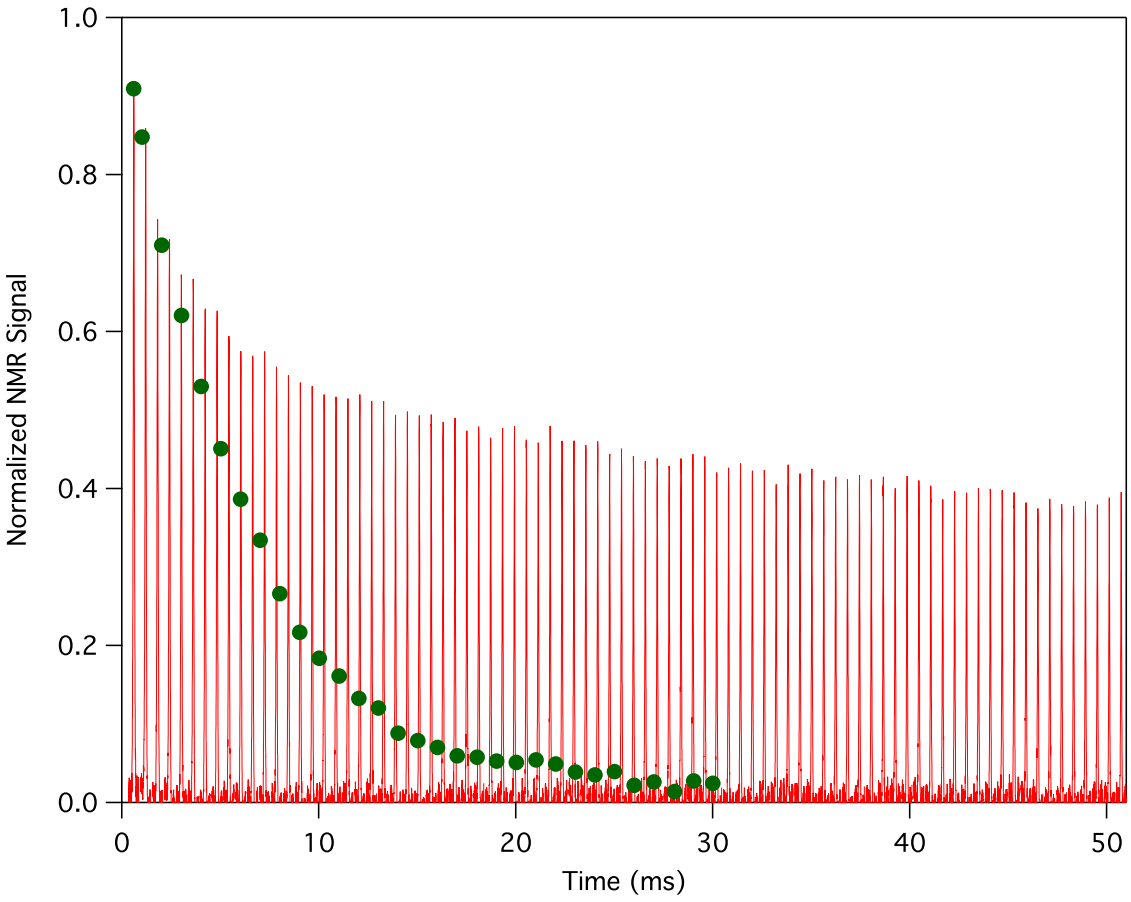

Figure 4.1: Two NMR experiments to measure T_2 of ^{29}Si in a crushed powder of Silicon doped with Phosphorous (3.94×10^{19} P/cm^3). Hahn echo peaks (dots) are generated with a single π pulse. The CPMG echo train (lines) is generated with multiple π pulses spaced with delay $2\tau = 592$ μs. Normalization is set by the initial magnetization after the 90_X pulse. Data taken at room temperature in a 12 Tesla field.

these diffusive dynamics quasi-static. In this case, the coherence from one echo to the next is maintained by resetting the start of the precession at each echo. As a consequence, the CPMG echo train can, under ideal circumstances, approach the natural diffusion-free T_2 limit. In contrast, the Hahn echo experiment with only one refocussing pulse can decay faster due to diffusion. However, in the solids studied here, the lack of diffusion makes the local field time-independent so the Hahn echoes and CPMG echo train are expected to agree, at least for delta-function π pulses.

The expected behavior of the CPMG sequence can be modeled using the density matrix $\rho(t)$, which represents the full quantum state of the system [18, 79]. The time-evolution of the density matrix is expressed as

$$\rho(t) = \{\mathcal{V}\mathcal{P}\mathcal{V}\}^n \rho(0) \left\{\mathcal{V}^{-1}\mathcal{P}^{-1}\mathcal{V}^{-1}\right\}^n, \tag{4.3}$$

where n is the number of π pulses applied. The total evolution time $t = n \times (2\tau + t_p)$ depends on τ, the duration of the free evolution period under $\mathcal{V}$, and t_p, the duration of the pulse period under $\mathcal{P}$. The form of the unitary operators $\mathcal{P}$ and $\mathcal{V}$ are not yet specified, so while equation (4.3) is complete, it is not yet very useful. We return to equation (4.3) as a model for our calculations in Chapters 5 and 8.

In the next sections of this chapter, we present additional NMR data [46], which further defy the conventional expectations that strong pulses should act like delta-function pules.

4.3 Other Strange Results with Multiple Pulses

Before calculating what we mean precisely by the expectations of delta-function π pulses, we present a series of NMR measurements that are surprising even for simple intuitive expectations. These NMR experiments try to illuminate different facets of the results from Figure 4.1.

Our first reaction to the long-tail in the CPMG echo train was to assume that the π pulses were somehow locking the magnetization along our measurement axis [52, 53, 54, 62, 72, 73, 83]. Increasing the time delay τ between π pulses reduces the pulse duty cycle down to less than 0.04% but the NMR signal still did not exhibit the expected behavior. Figure 4.2 shows three CPMG echo trains with three different interpulse time delays. For short

delays between π pulses, the CPMG echo train exhibits a long tail [Figure 4.2(top)]. For intermediate delays, some slight modulation develops in the echo envelope [Figure 4.2(middle)]. For much longer delays, we observe an even-odd effect where even-numbered echoes are much larger than odd-numbered echoes that occur earlier in time [45, 14, 21] [Figure 4.2(bottom)].

The slight modulation of the echo envelope for the middle graph of Figure 4.2 is more visible when we perform the same CPMG experiment on a Silicon sample with a lower doping. Figure 4.3 shows CPMG echo trains in Si:P (3×10^{13} P/cm^3) and Si:B (1.43×10^{16} B/cm^3). Here, the echo shape is much wider in time than for the higher doped Si:P (10^{19} P/cm^3) sample because the Zeeman spread is much smaller. The heights of the echoes in Figure 4.3 modulate in a seemingly noisy way. However, when sampling short segments of echoes, an unusual fingerprint pattern emerges repeatedly throughout the echo train. Sections of the echo train are highlighted and overlapped to help guide the eye. Figures 4.2 and 4.3 are evidence of complicated coherent effects.

From the analysis of Chapter 4, the calculated envelope $|\langle I_{y_1}(t)\rangle|$ is expected to be insensitive to the π pulse phase. We define the following four pulse sequences

$$\begin{aligned}
\text{CP} &: 90_X - \tau - \{180_X - 2\tau - 180_X - 2\tau\}^n \\
\text{APCP} &: 90_X - \tau - \{180_{\bar{X}} - 2\tau - 180_X - 2\tau\}^n \\
\text{CPMG} &: 90_X - \tau - \{180_Y - 2\tau - 180_Y - 2\tau\}^n \\
\text{APCPMG} &: 90_X - \tau - \{180_{\bar{Y}} - 2\tau - 180_Y - 2\tau\}^n
\end{aligned}$$

where $\bar{X}$ indicates rotation about $-\hat{x}$ and $\bar{Y}$ indicates rotation about $-\hat{y}$. The Carr-Purcell (CP) sequence [9] features π pulses along $\hat{x}$, the CPMG sequence [58] features π pulses along $\hat{y}$, and the alternating phase (AP-) versions flip the phase after each π pulse. The spin echoes form in the middle of each 2τ time period. For CP and APCP, the spin echoes form alternatingly along $\hat{y}$ and $-\hat{y}$, while in CPMG and APCPMG they form only along $\hat{y}$. Though all of these sequences are expected to decay with the same envelope, they differ drastically in experiment (Figure 4.4). The CP sequence decays extremely fast, while the APCP and CPMG sequences have extremely long-lived coherence. The pulse sequence sensitivity exhibited in Figure 4.4 demonstrates that the π pulses play a key role in the system's response.

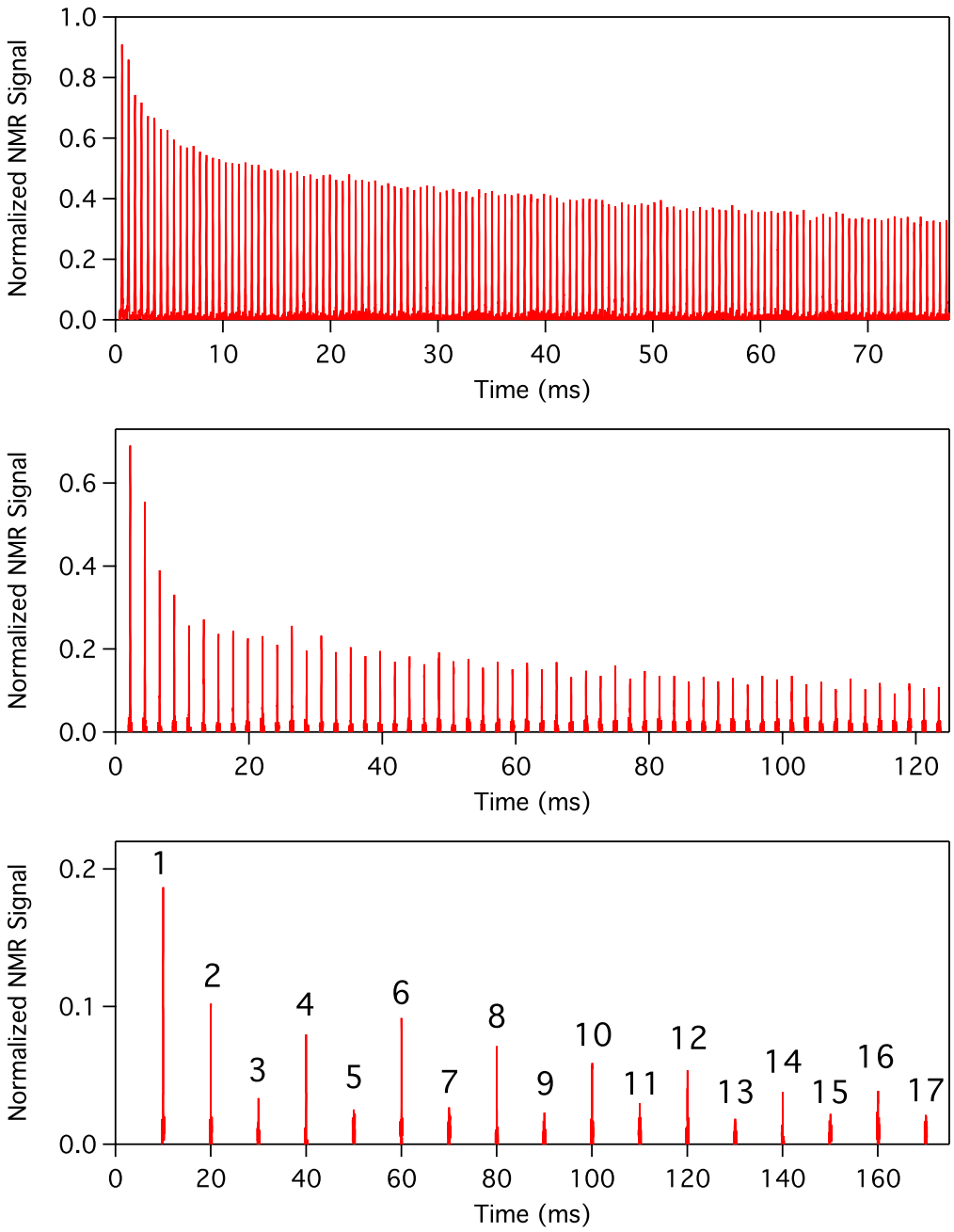

Figure 4.2: CPMG echo trains of ^{29}Si in Si:P (3.94×10^{19} P/cm^3) with three time delays between π pulses. (Top) $2\tau = 592$ μs. (Middle) $2\tau = 2.192$ ms. (Bottom) $2\tau = 9.92$ ms. For comparison, $T_2 = 5.6$ ms in silicon as measured by the Hahn echoes and as predicted by the delta-function pulse approximation. Data taken at room temperature in a 12 Tesla field.

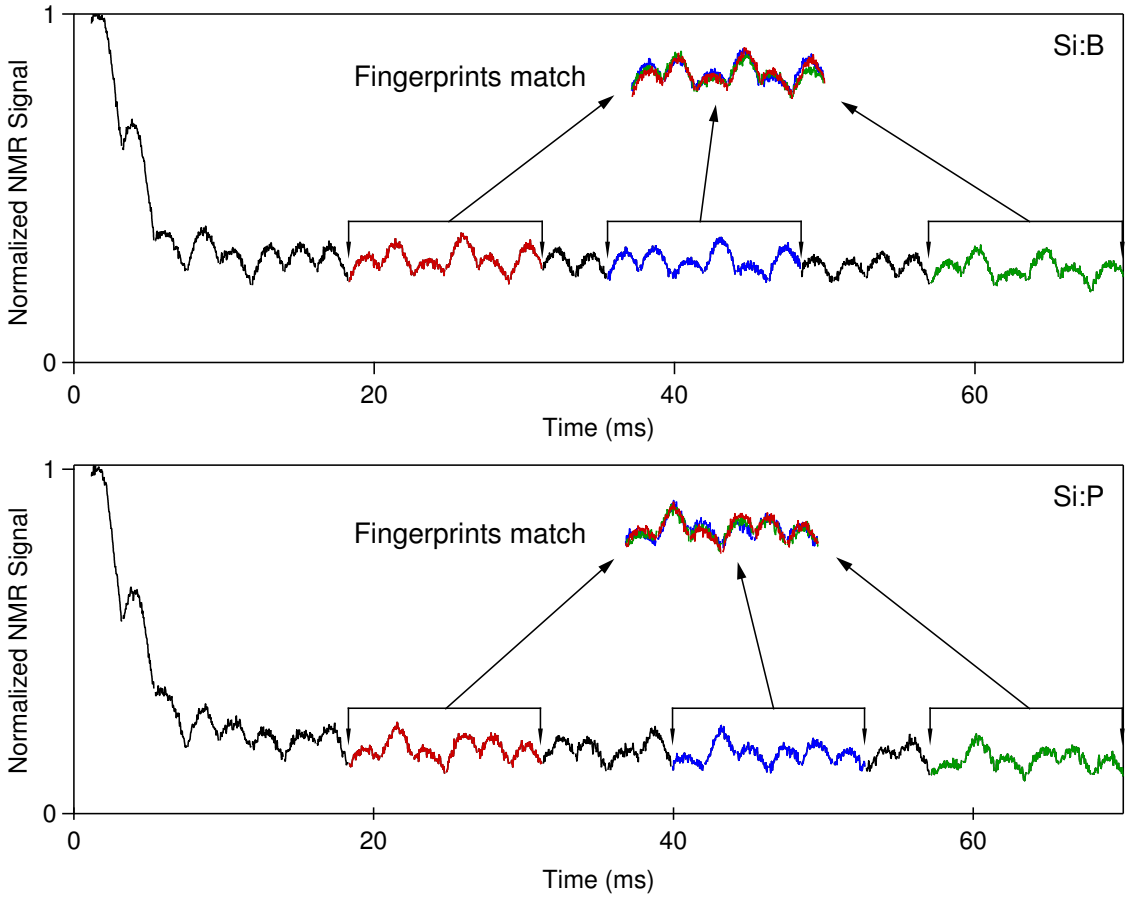

Figure 4.3: Repeated fingerprint patterns in the CPMG echo train with $2\tau = 2.192$ ms. Two different samples are shown: (top) Si:B (1.43×10^{16} B/cm^3), and (bottom) Si:P (3×10^{13} P/cm^3). Data taken at room temperature in a 7 Tesla field.

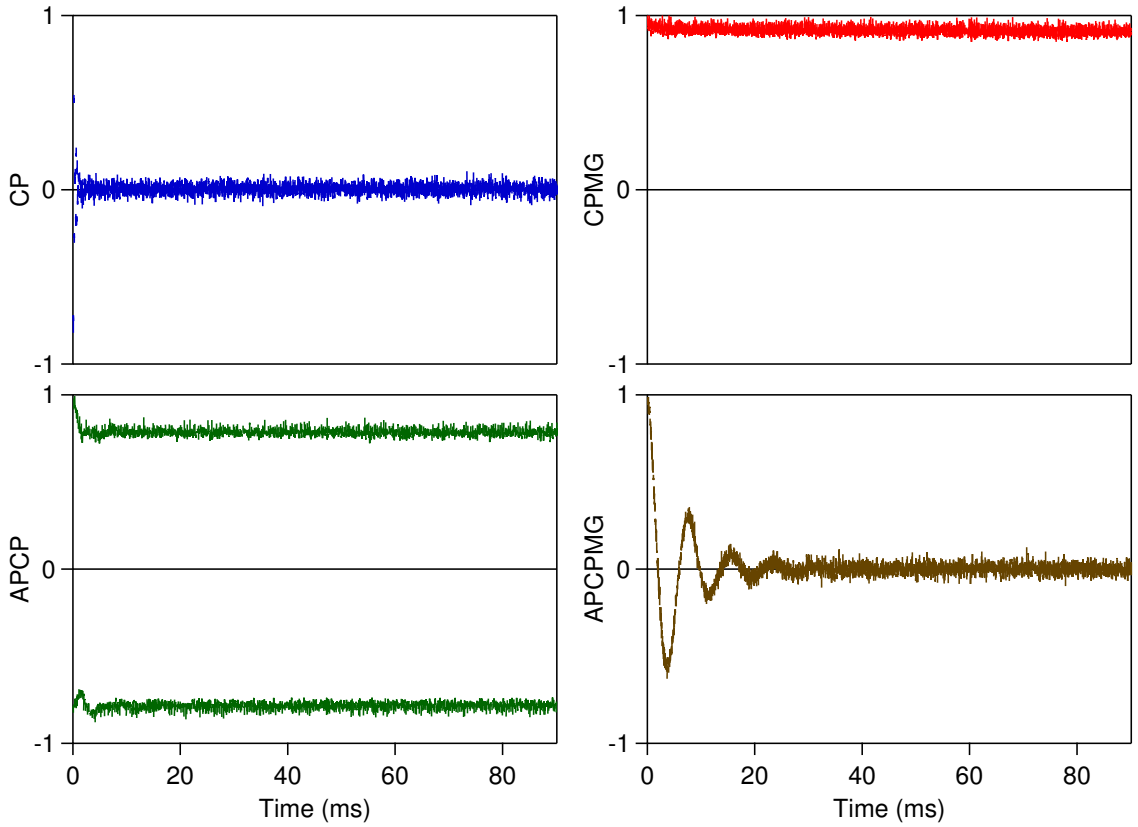

Figure 4.4: Four pulse sequences with π pulses of different phases applied to ^{29}Si in Si:Sb (2.75×10^{17} Sb/cm^3). (Top Left) CP, (Top Right) CPMG, (Bottom Left) APCP, (Bottom Right) APCPMG. All are expected to yield identical decay curves. $2\tau = 72$ μs, $T = 300$ K, and $B^{\text{ext}} = 11.74$ Tesla.

4.4 The Anomalous Stimulated Echo

The peculiarities of the even-odd effect at the bottom of Figure 4.2 led us to pursue the degree to which the even echoes were larger than odd echoes that came earlier in time.

Figure 4.5 shows the first two echoes in the CPMG echo train for extremely long delays between π pulses. Since $T_{2_{\mathrm{HE}}} \approx 5.6$ ms as measured by Hahn echoes in silicon, it is not surprising that the first echo (SE1) has such a small amplitude. However, the second echo (SE2) is substantially larger, simply because it occurs after two π pulses instead of only one. After doubling the delay between π pulses, SE1 is lost in the noise even though it is supposed to appear at the same absolute time as the SE2 from the above graph. Though SE1 is absent, SE2 is clearly visible, which begs the question of the echo's source.

This extreme version of the even-odd effect requires only three pulses: the initial 90_X pulse, and two 180_Y pulses. In literature searches for special NMR experiments involving only three pulses, we stumbled upon the stimulated echo [7].

The standard form of the stimulated echo consists of three 90 degree pulses. Figure 4.6 outlines the standard placement of the pulses in the stimulated echo sequence. It is important to note that the timing between the first and second pulse is TE/2 while the timing between the second and third pulse is TM. In general, TM$\neq$TE.

The formation of the standard stimulated echo requires the action of all three pulses. Using the Bloch Sphere with non-interacting spins, we can demonstrate how the pulses bring about the stimulated echo at the proper time.

In equilibrium the spins have a net magnetization aligned with the external magnetic field B^{ext} parallel to $\hat{z}$ [Figure 4.6(a)].

After the first pulse, 90_X, the spins are brought into the xy-plane and begin to precess in the presence of the external magnetic field. Different spins experience slightly different local magnetic fields B^{loc} due differences in their local environments, such as impurities. Therefore, each spin i precesses at a slightly different resonance frequency $\omega_{0_i} = \gamma(B^{\mathrm{ext}} + B_i^{\mathrm{loc}})$. Because of the different frequencies present, the spins develop a phase shift between one another, fanning out in the xy-plane. The resultant magnetization thus decays [Figure 4.6(b)] with time constant $T_2^\star$. This decay is known as the *free induction decay* (FID) since it is observed as an oscillating voltage.

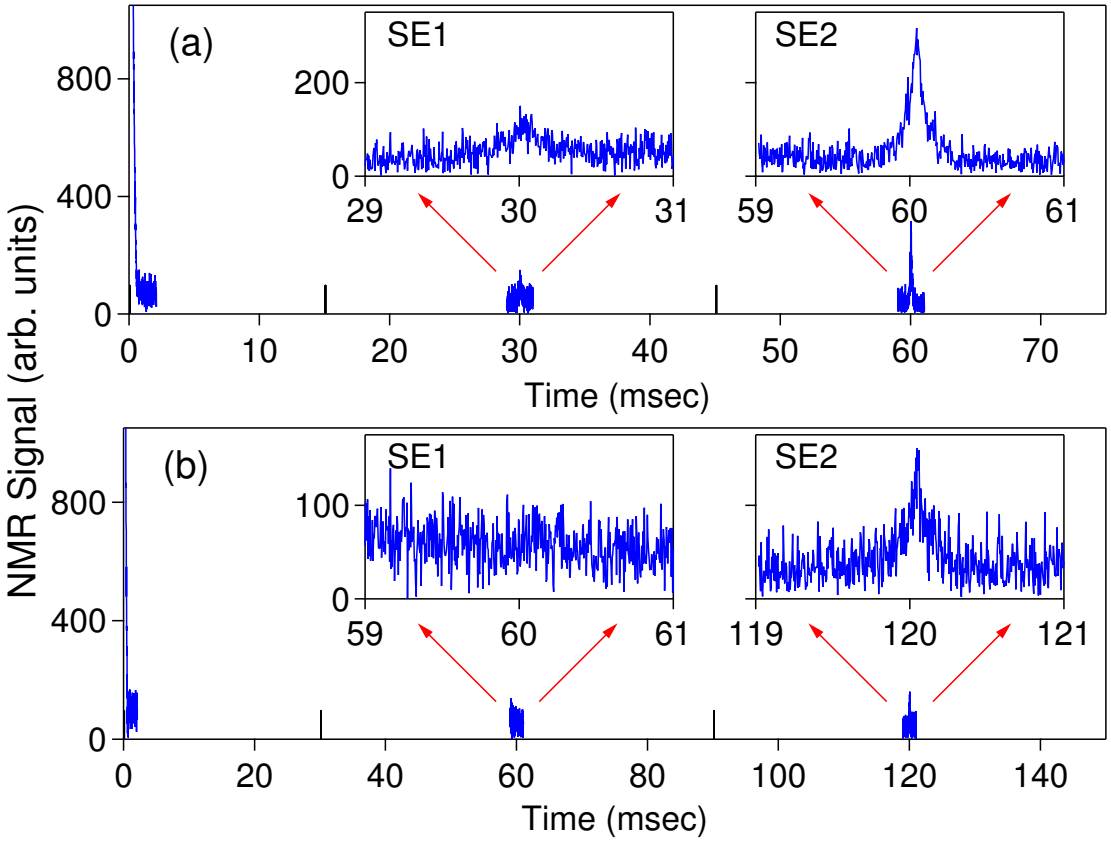

Figure 4.5: The first two echos in a CPMG echo train in silicon doped with phosphorous (Si:P, 10^{19} P/cm^3). (Top) a time delay of 30 ms between π pulses shows a very small peak for the first echo as is expected since $T_{2_{\rm HE}} \approx 5.6ms$. The second echo appears larger even though it occurs at 60 ms. (Bottom) Most surprising, when the delay between π pulses is doubled, the first echo is lost in the noise, while the second echo appears. For comparison, the height of the initial polarization is 14,600 on the same scale. Data taken at room temperature in a 7 Tesla field.

The second pulse, 90_Y, is applied some time after the initial decay. The delay between the first two pulses is defined as TE/2. Another delay of TE/2 after the second pulse gives the timing for the 90-90 SE1 illustrated as a three dimensional figure-8 on the Bloch Sphere [Figure 4.6(c)].

The third pulse, another 90_Y, is applied a delay of TM>TE after the second pulse. Though the location of the spins is more complicated on the Bloch Sphere [Figure 4.6(d)] the fixed precession of the individual spins results in four echoes. The first echo in time is the stimulated echo [Figure 4.6(e)], followed by the 90-90 SE2, and two additional 90-90 echoes caused by the second and third pulses, or the first and third pulses in respective order.

An important feature of the standard stimulated echo is that it requires all three pulses to form, unlike the other generated echoes. An easier way to understand how the stimulated echo forms is to consider just two spins. The first pulse, 90_X, puts the two spins into the xy-plane. After an ideal amount of time, the spins have precessed from the y-axis to the x-axis with one spin parallel to $+\hat{x}$ and the other parallel to $-\hat{x}$. The second pulse, 90_Y, moves these two spins to the $\pm z$-axis where they stop precessing and are protected from most decay mechanisms. The final pulse, 90_y, brings these spins back down to the $\pm x$-axis where they require the same amount of time to refocus as the delay between the first and second pulses. Consequently, the stimulated echo should be independent of TM.

We performed the standard 90-90-90 stimulated echo sequence in Si:P (10^{19} P/cm^3) to see if the unexpected results from the multiple π pulse experiments carried over. Figure 4.7 shows that the standard stimulated echo data agreed with conventional expectations. The data decay at the same rate as the 90-90 SE1 and the 90-90 SE2. Additionally, since there is a required lag time for spins to reach the $\pm x$-axis, after the first pulse, we expect a smaller stimulated echo for shorter TE/2 delays. Experiments using 90 degree pulses therefore have fulfilled our expectations.

Energized with the fresh confidence from these results, we extended the three pulse stimulated echo sequence to include π pulses. The sequence

$$90_X - \mathrm{TE}/2 - 90_Y - \mathrm{TM} - 90_Y$$

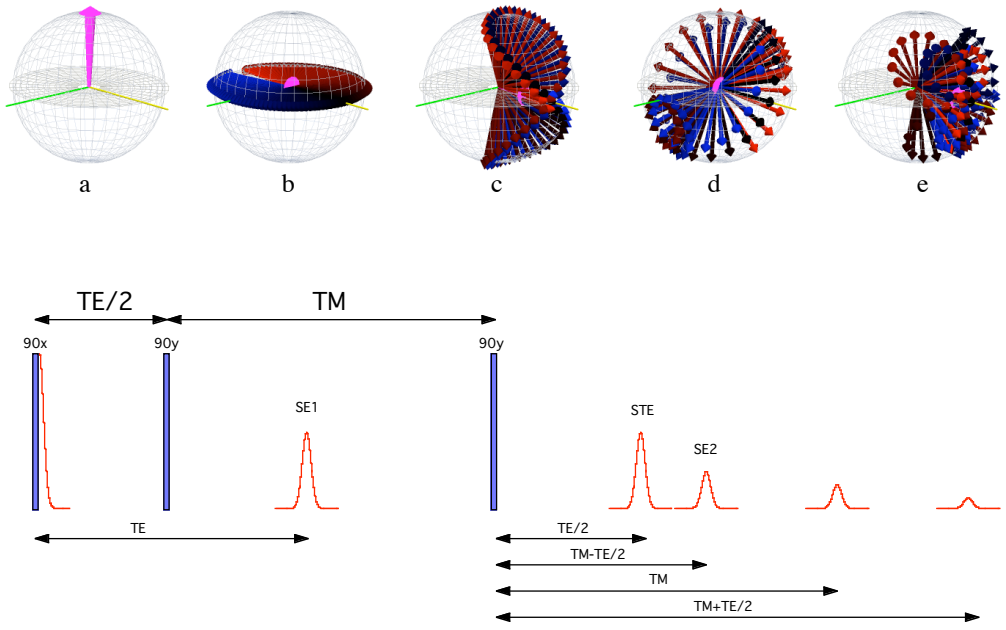

Figure 4.6: The stimulated echo sequence [7] with all 90 degree pulses can be understood using the Bloch Sphere with non-interacting spins. (a) the spins start at equilibrium aligned along $\hat{z}$, (b) after the first 90_X pulse, the spins fan out in the xy-plane because of slightly different local Zeeman energies, (c) at time TE/2 after the second pulse (the first 90_y) the figure-8 echo forms, (d) at time TM after the first 90_y pulse, a second 90_y pulse (third overall pulse) is applied, (e) the stimulated echo forms at a time TM-TE separated from the usual spin echo number 2 (SE2).

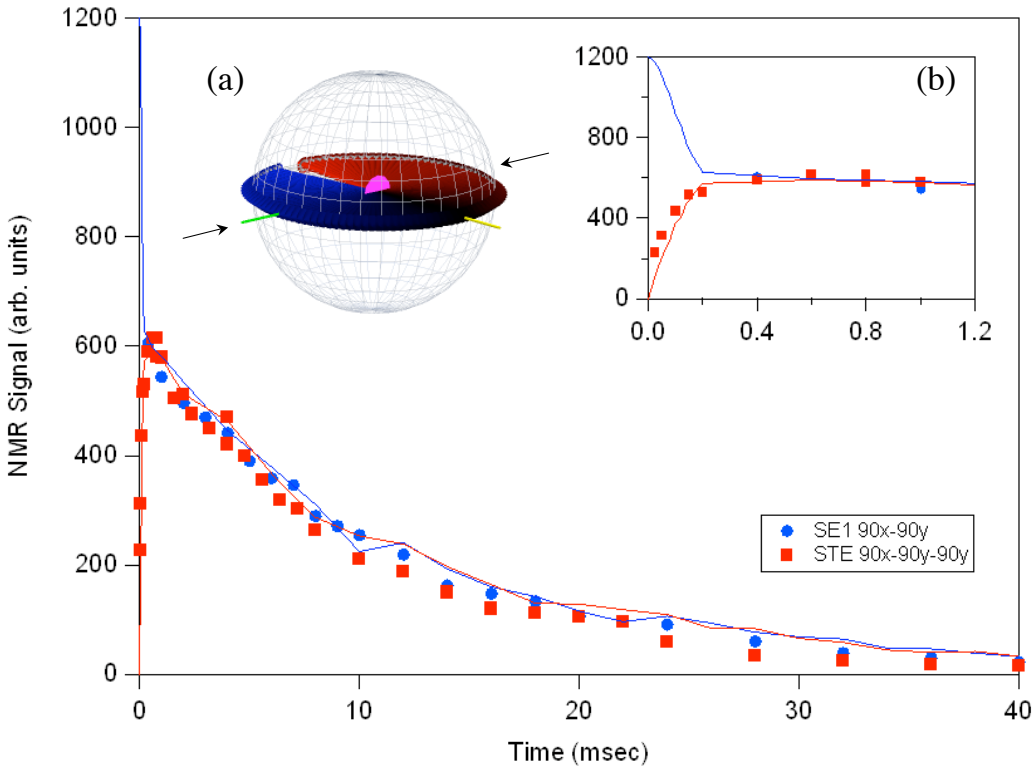

Figure 4.7: 90-90-90 stimulated echo data in silicon doped with phosphorous. These stimulated echoes decay with the same decay time as SE1 and SE2 as expected. (a) As the spins fan out in the Bloch Sphere, the second 90 degree pulse moves spins aligned along the x-axis to the z-axis. Spins along the z-axis are subsequently protected from decay during the TM time period. (b) Because spins take time to fan out to the x-axis, the stimulated echo is expected to grow from zero for short TE times.

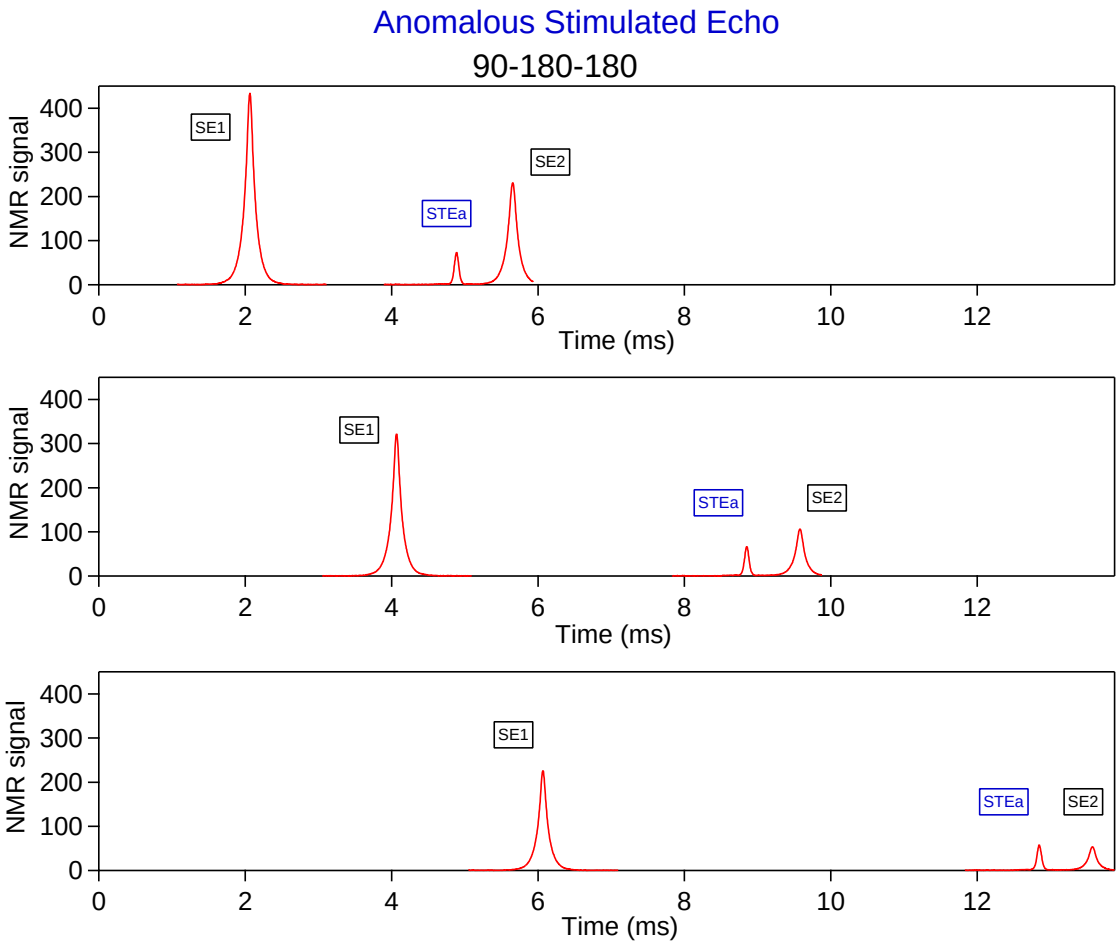

Figure 4.8: Analogous to the standard 90-90-90 stimulated echo, we found a 90-180-180 stimulated echo with anomalous characteristics. These series of figures show that the anomalous stimulated echo produced with π pulses does not decay with the same time constant as SE1 or SE2, in contrast to the standard stimulated echo.

was converted to

$$90_X - \mathrm{TE}/2 - 180_Y - \mathrm{TM} - 180_Y,$$

which is only a slight variation from the CPMG sequence in that TE is extended to TM after the second pulse.

Figure 4.8 shows three NMR experiments using the modified stimulated echo sequence with π pulses. An echo appears at the proper time analogous to the stimulated echo, which we refer to as the anomalous stimulated echo (STEa). Strangely, as the delay time TE is increased, both SE1 and SE2 decay as expected, while STEa appears relatively constant in amplitude.

Figure 4.9 plots a series of STEa data together in Si:P (10^{19} P/cm^3). Aside from appearing at the analogous time, the STEa does not behave like the standard stimulated echo.

The STEa answers one concern that the pulses we apply are not the proper angle that we desire. In other words, a maladjusted π pulse could actually be a $\pi/2$ pulse, in which case the STEa is simply the standard stimulated echo. However, Figure 4.9 is starkly different from Figure 4.7. The STEa does not decay similarly to SE1 or SE2, nor does it grow from zero for small TE. Furthermore, the scatter in the STEa amplitudes is abnormally high given the signal to noise ratio [14].

Though the anomalous stimulated echo certainly stimulated an enormous amount of theoretical and experimental work in our lab, it inevitably did not lead to a better understanding of the underlying cause of the phenomena of Figure 4.1. Other attempts were made such as a four pulse sequence in the hopes of understanding the source of echoes generated similarly to the STEa. Additionally, in one experiment we even tried to progressively increase the delay between all successive π pulses in the CPMG echo train to see how many STEa like coherences would be observed. While many of these explorations are interesting on their own right, they lead us astray from the main puzzling discrepancy between the Hahn echo and the CPMG echo train.

In order to find a foothold on the physical principles at the root of these experiments, we temporarily halt our experimental explorations to calculate what we mean by the conventional expectations of instantaneous pulses.

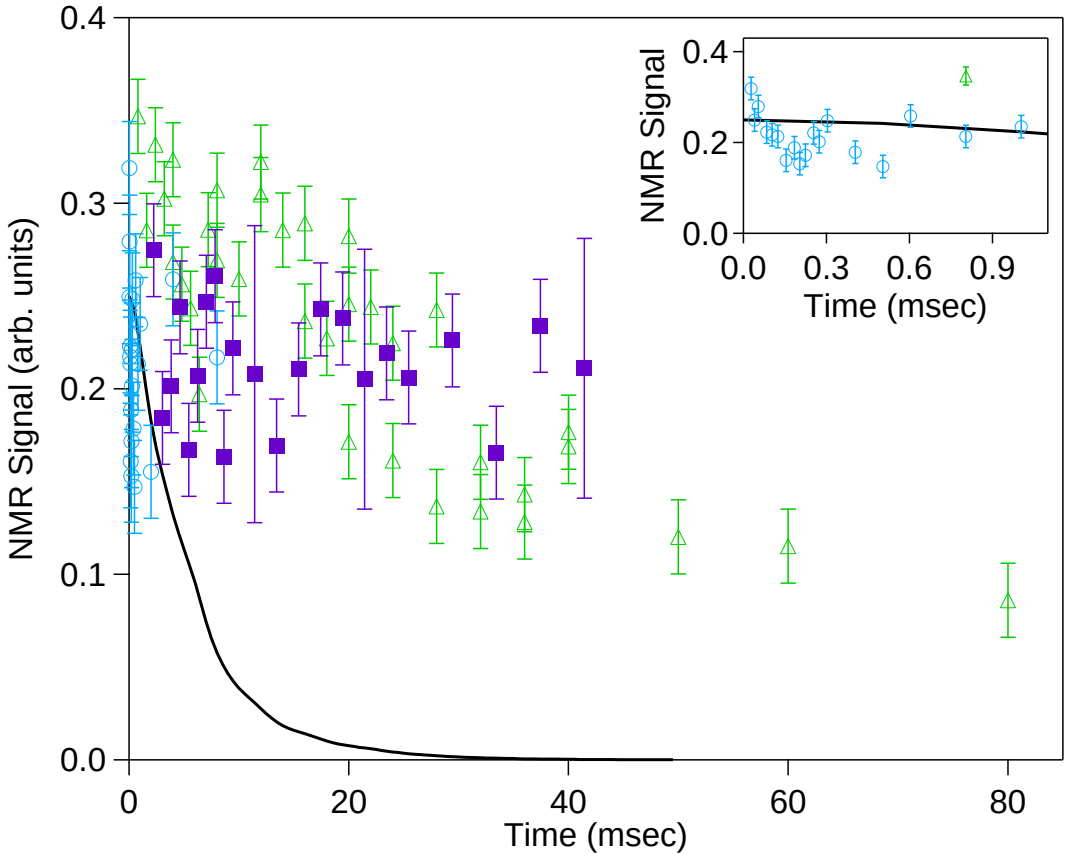

Figure 4.9: A collection of anomalous stimulated echo data in silicon doped with phosphorous shows a non-decaying signal and surprisingly large fluctuations in amplitude. (Inset) The stimulated echo does not appear to grow from zero at early times. Data taken at room temperature in a 7 Telsa field. Filled squares (TE$\approx$ 0.4 ms) are plotted versus TE+TM. Empty circules (TM$\approx$ 10 ms) and triangles (TM$\approx$ 21 ms) are plotted versus TE. The solid line is calculated Ising model decay.

Chapter 5

Expected Results for Instantaneous π Pulses

In this chapter, we calculate the expected behavior of N spin-1/2 particles under the action of pairwise dipolar coupling and instantaneous π pulses to compare with the experimental results of Figure 4.1.

5.1 The Internal Spin Hamiltonian

In order to calculate the expected behavior, we first write the relevant internal Hamiltonian for the system. The ideal Hamiltonian for a solid containing N spin-1/2 nuclei in an external magnetic field contains two parts [1, 55, 79]. In the lab frame, the Zeeman Hamiltonian

$$\mathcal{H}_Z^{\text{Lab}} = \sum_{j=1}^{N} -\gamma\hbar(B^{\text{ext}} + \Delta B_j^{\text{loc}})I_{z_j} \tag{5.1}$$

describes the interaction with the applied and local magnetic fields, while the dipolar Hamiltonian

$$\mathcal{H}_d^{\text{Lab}} = \sum_{j=1}^{N}\sum_{k>j}^{N}\left[\frac{\vec{\mu}_j \cdot \vec{\mu}_k}{|\vec{r}_{jk}|^3} - \frac{3(\vec{\mu}_j \cdot \vec{r}_{jk})(\vec{\mu}_k \cdot \vec{r}_{jk})}{|\vec{r}_{jk}|^5}\right] \tag{5.2}$$

describes the interaction between two spins. In these Hamiltonians, γ is the gyromagnetic ratio and B^{ext} is an external magnetic field applied along $\hat{z}$. For spin j, ΔB_j^{loc} is the local magnetic field, $\vec{\mu}_j = \gamma\hbar\vec{I}_j$ is the magnetic moment, and $\vec{I}_j = (I_{x_j}, I_{y_j}, I_{z_j})$ is the spin angular momentum vector operator. The position vector between spins j and k is $\vec{r}_{jk}$.

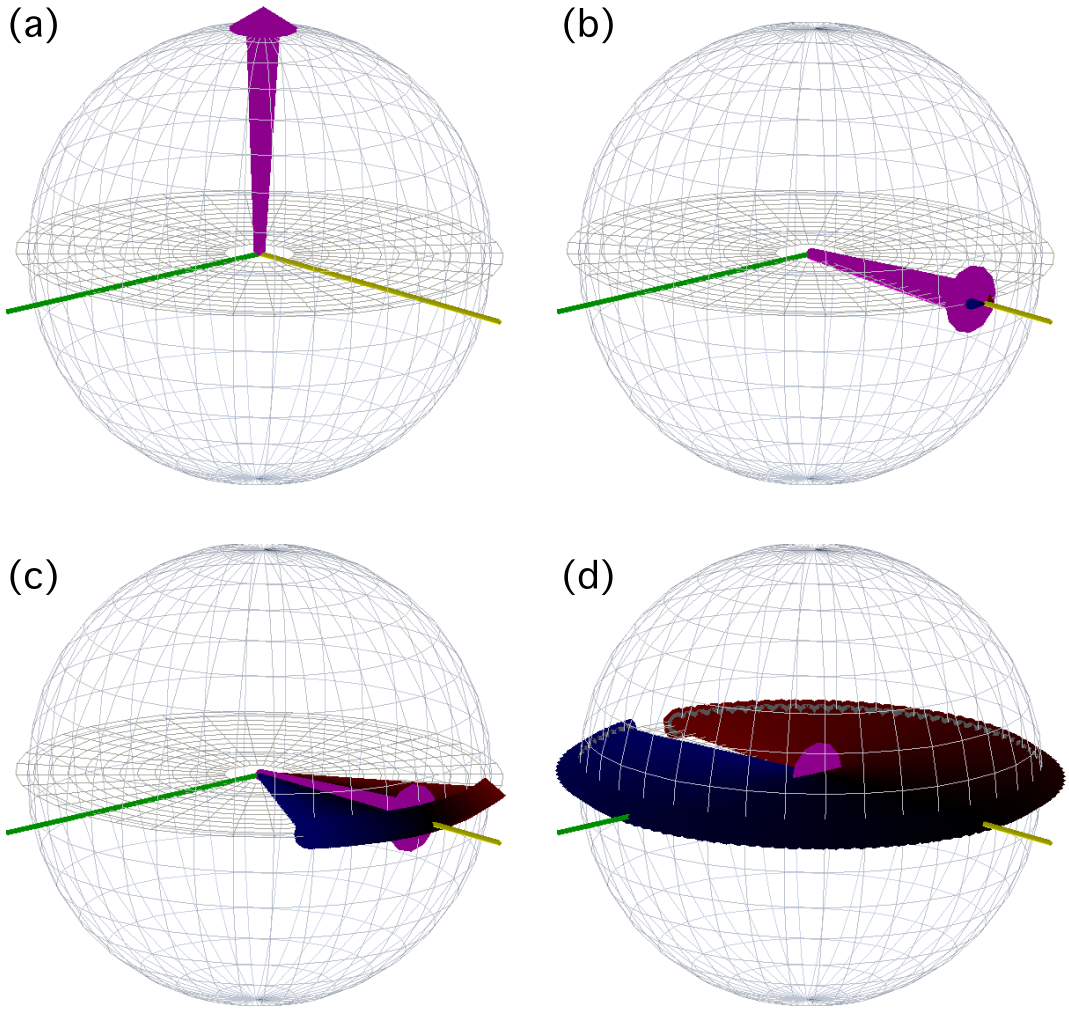

Figure 5.1: Bloch sphere depiction of signal decay due to a spread of Zeeman shifts. An external magnetic field is aligned along $\hat{z}$. (a) Spins in equilibrium with total magnetization represented by a large pink arrow. (b) After a 90_X pulse, the spins are aligned along $\hat{y}$ in the rotating frame. (c) Spins with different Zeeman shifts precess at different rates and fan apart. Red arrows represent spins with a positive Zeeman shift ($\Omega_z > 0$), blue arrows represent spins with a negative Zeeman shift ($\Omega_z < 0$), and black arrows represent spins on resonance ($\Omega_z = 0$). (d) After some time, the total magnetization decays to zero.

We proceed to the rotating reference frame [1, 55, 79] defined by the Larmor precession frequency $\omega_0 = \gamma B^{\text{ext}}$. The Zeeman term largely vanishes leaving only a small Zeeman shift due to spatial magnetic inhomogeneities. The Zeeman shift for spin j is defined as $\Omega_{z_j} = -\hbar\gamma\Delta B_j^{\text{loc}}$. The scale of the spread of Zeeman shifts depends on the sample. For highly disordered samples, or samples with magnetic impurities, Ω_{z_j} varies wildly between adjacent spins. The samples studied in this paper are much more homogeneous, so Ω_{z_j} is essentially the same for a large number of neighboring spins. We therefore drop the index j giving the Zeeman Hamiltonian in the rotating frame

$$\mathcal{H}_Z = \sum_{j=1}^{N} \Omega_z I_{z_j} = \Omega_z I_{z_T} \tag{5.3}$$

where $I_{z_T} = \sum_{j=1}^{N} I_{z_j}$ is the total I_z spin operator. Experiments that justify this assumption are presented in Chapter 6.

Even in the absence of the dipolar interaction, Zeeman shifts from different parts of the sample can cause signal decay as shown in the Bloch sphere representation in Figure 5.1. Each colored arrow represents a group of spins that experience a different ΔB^{loc} resulting in a slightly different precession frequency $\Omega_z/\hbar$ in the rotating frame. The initial magnetization at equilibrium starts aligned along the z-axis [Figure 5.1(a)]. After a 90_X pulse, the spins are tipped along the y-axis [Figure 5.1(b)]. Because of the spread of Zeeman shifts, spins in the rotating frame will begin to drift apart [Figure 5.1(c)]. The resultant magnetization, or vector sum, will consequently decay [Figure 5.1(d)]. This process is referred to as the free induction decay (FID) since it is detected in the NMR apparatus as a decaying oscillatory voltage arising from magnetic induction in the detection coil [47, 79, 11].

Even without a spread of Zeeman shifts across the sample, transverse magnetization will decay due to the dipolar coupling. It is appropriate to treat the dipolar Hamiltonian as a small perturbation [79] since the external magnetic field is typically four to five orders of magnitude larger than the field due to a nuclear moment. In this case, the secular dipolar Hamiltonian in the rotating frame is

$$\mathcal{H}_{zz} = \sum_{j=1}^{N} \sum_{k>j}^{N} B_{jk}(3I_{z_j}I_{z_k} - \vec{I_j} \cdot \vec{I_k}) \tag{5.4}$$

where the terms dropped from equation (5.2) are non-secular in the rotating frame. We define the dipolar coupling constant as

$$B_{jk} \equiv \frac{1}{2}\frac{\gamma^2\hbar^2}{|\vec{r}_{jk}|^3}(1 - 3\cos^2\theta_{jk}) \tag{5.5}$$

where θ_{jk} is the angle between $\vec{r}_{jk}$ and $\vec{B}^{\text{ext}}$.

Thus, the relevant total internal spin Hamiltonian is

$$\mathcal{H}_{int} = \mathcal{H}_Z + \mathcal{H}_{zz} \tag{5.6}$$

where we note that $\mathcal{H}_Z$ commutes with $\mathcal{H}_{zz}$. From this Hamiltonian, the free-evolution operator is defined as

$$\mathcal{U} \equiv e^{-\frac{i}{\hbar}\mathcal{H}_{int}\tau} = e^{-\frac{i}{\hbar}\mathcal{H}_Z\tau}e^{-\frac{i}{\hbar}\mathcal{H}_{zz}\tau} \equiv \mathcal{U}_Z\mathcal{U}_{zz} \tag{5.7}$$

where $\mathcal{U}_Z$ and $\mathcal{U}_{zz}$ also commute.

5.2 Simplifying the External Pulse

During the pulses, another time-evolution operator is needed. This pulse time-evolution operator is complicated since it contains all the terms in the free evolution plus an additional term associated with the rf pulse.

$$\mathcal{P}_\phi = \exp\left(-\frac{i}{\hbar}(\mathcal{H}_Z + \mathcal{H}_{zz} + \mathcal{H}_{P_\phi})t_p\right) \tag{5.8}$$

where

$$\mathcal{H}_{P_\phi} = -\hbar\omega_1 I_{\phi_T} \tag{5.9}$$

for a radio frequency pulse with angular frequency ω_1 and transverse phase ϕ. In practice, the pulse strength and phase could vary from spin to spin. Studies of the effects of this type of rf inhomogeneity are reported in Chapter 5, but this approximate calculation considers the homogeneous case.

Note that $\mathcal{H}_{P_\phi}$, in general, does not commute with $\mathcal{H}_{int} = \mathcal{H}_Z + \mathcal{H}_{zz}$. Because of this inherent complication, it is advantageous to make ω_1 large so that $\mathcal{H}_{P_\phi}$ dominates $\mathcal{P}_\phi$. This strong-pulse limit is achieved when $\omega_1 \gg \Omega_z/\hbar$ and $\omega_1 \gg B_{jk}/\hbar$. This paper is primarily

concerned with π pulses, which sets the pulse duration t_p so that $\omega_1 t_p = \pi$. The delta-function pulse approximation [1, 18, 22, 28, 55, 79] takes the limit $\omega_1 \to \infty$ and $t_p \to 0$ so that $\mathcal{P}_\phi$ simplifies to a pure left-handed π rotation

$$\mathcal{R}_\phi = \exp\Big(i\pi I_{\phi_T}\Big). \tag{5.10}$$

For these delta-function π pulses, the linear Zeeman Hamiltonian is perfectly inverted, while the bilinear dipolar Hamiltonian remains unchanged. The time-evolution operators thus transform as

$$\mathcal{R}_\phi \mathcal{U}_Z \mathcal{R}_\phi^{-1} = \mathcal{U}_Z^{-1} \tag{5.11}$$

$$\mathcal{R}_\phi \mathcal{U}_{zz} \mathcal{R}_\phi^{-1} = \mathcal{U}_{zz}. \tag{5.12}$$

In other words, after a π pulse, the Zeeman spread will refocus, while the dynamics due to dipolar coupling will continue to evolve as if the π pulse was never applied. Equation (5.12) is the basis for the statement: "π pulses do not refocus the dipolar coupling".

5.3 An Analytic Expression for the Evolution of the Density Matrix with Instantaneous Pulses

Using the free-evolution operator and the delta-function pulse, equation (4.3) for CPMG simplifies to

$$\begin{aligned}
\rho(t) &= \{\mathcal{U} R_y \mathcal{U}\}^n \rho(0) \left\{\mathcal{U}^{-1}\mathcal{R}_y^{-1}\mathcal{U}^{-1}\right\}^n \\
&= \left\{\mathcal{U}\mathcal{R}_y(\mathcal{R}_y^{-1}\mathcal{R}_y)\mathcal{U}(\mathcal{R}_y^{-1}\mathcal{R}_y)\right\}^n \rho(0)\{inv\}^n \\
&= \left\{\mathcal{U}_{zz}\mathcal{U}_Z\mathcal{U}_Z^{-1}\mathcal{U}_{zz}\mathcal{R}_y\right\}^n \rho(0)\{inv\}^n \\
&= (\mathcal{U}_{zz})^{2n}(R_y)^n\rho(0)(R_y^{-1})^n(\mathcal{U}_{zz}^{-1})^{2n} \\
&= (\mathcal{U}_{zz})^{2n}\rho(0)(\mathcal{U}_{zz}^{-1})^{2n} \\
&= \mathcal{U}_{zz}(t)\rho(0)\mathcal{U}_{zz}^{-1}(t).
\end{aligned} \tag{5.13}$$

where $\{inv\}$ is the inverse of the operators in brackets to the left of $\rho(0)$, the dipolar time-evolution operator for time t is $\mathcal{U}_{zz}(t) = \exp(-\frac{i}{\hbar}\mathcal{H}_{zz}t)$, and we assumed $(R_y)^n\rho(0)(R_y^{-1})^n = \rho(0) = I_{y_T}$. Invoking equations (5.7), (5.11), and (5.12) has allowed the cancellation of $\mathcal{U}_Z$.

By assuming that the pulses are instantaneous, the density matrix at the time of an echo is independent of the Zeeman spread and the number of applied pulses. In other words, the peaks of the Hahn echoes and the CPMG echo train should follow the same decay envelope given by the dipolar-only ($\Omega_z = 0$) FID.

5.4 General Method to Calculate the Observable NMR Signal

The last step is to calculate the measured quantity that is relevant to our NMR experiments. The NMR signal is proportional to the transverse magnetization in the rotating reference frame [1, 18, 22, 28, 55, 79]. Therefore, we wish to calculate

$$\langle I_{y_T}(t)\rangle = \sum_{j=1}^{N} \mathrm{Tr}\{\rho(t) I_{y_j}\}. \tag{5.14}$$

The real experiment involves a macroscopic number of spins N but computer limitations force us to use only small clusters of coupled spins. Since the size of the density matrix grows as $2^N \times 2^N$ we are limited to $N < 10$.

To mimic a macroscopic system with only a small cluster of spins, we first built a lattice with the appropriate unit cell for the solid under study. Then we randomly populated the lattice with spins according the natural abundance. For one spin at the origin, $N-1$ additional spins were chosen with the strongest coupling $|B_{1k}|$ to the central spin. Finally, we disorder-averaged over many random lattice populations to sample different regions of a large crystal. For powder samples, we also disorder-averaged over random orientations of the lattice with respect to $\vec{B}^{\mathrm{ext}}$. This method is biased to make the central spin's local environment as realistic as possible since the dipole coupling falls off as $1/r^3$. We therefore chose to calculate $\langle I_{y_1}(t)\rangle$ instead of $\langle I_{y_T}(t)\rangle$ since spins along the border of the cluster only interact with spins inside the cluster.

Using these clusters, the time dependence of the density matrix is calculated by starting from its conventional Boltzmann equilibrium value

$$\rho_B = I_{z_T} \tag{5.15}$$

assuming a strong B^{ext} and high temperature [55]. Treating a strong 90_X pulse as a perfect left-handed rotation about $\hat{x}$, ρ_B transforms as

$$\rho(0) = \mathcal{R}_{90_X}\rho_B\mathcal{R}_{90_X}^{-1} = I_{y_T}. \tag{5.16}$$

From this point, equation (5.13) gives the evolution for $\rho(t)$ in the limit of delta-function π pulses:

$$\rho(t) = \mathcal{U}_{zz}(t)I_{y_T}\mathcal{U}_{zz}^{-1}(t). \tag{5.17}$$

For each disorder realization (DR), the density matrix at time $t + dt$ is calculated by using the basis representation that diagonalizes the internal Hamiltonian. In this basis, the density matrix is given by the matrix formula

$$\rho_{mn}(t + dt) = \rho_{mn}(t)e^{-\frac{i}{\hbar}(E_m - E_n)dt} \tag{5.18}$$

where E_m is the mth eigenvalue of $\mathcal{H}_{zz}$, and ρ_{mn} is the element at the mth row and nth column of the $2^N \times 2^N$ density matrix [79]. Using the density matrix at each time t, the expectation value $\langle I_{y_1}(t)\rangle = \text{Tr}\{\rho(t)I_{y_1}\}$ is calculated for each DR, and then averaged over many DRs, yielding the expected decay for both CPMG and Hahn echoes [Figure 5.4(blue curve)]. These calculations were originally done by Kenneth MacLean in a computer program he wrote in Igor Pro. I subsequently verified the results independently in my own program. Three different methods for choosing the N spins are discussed at the end of Chapter 9.

Though $\mathcal{H}_{zz}$ is the appropriate Hamiltonian to consider, the small number of spins that we are able to treat can never describe the true dynamics of a macroscopic system even after substantial disorder averaging.

5.5 Ising Model Truncation

Let us consider another approach that truncates the secular dipolar Hamiltonian and yields an analytic expression for $\langle I_{y_1}(t)\rangle$ in the delta-function pulse limit. This truncation enables us to model the behavior of many more spins.

The secular dipolar Hamiltonian from equation (5.4) can be rewritten as

$$\mathcal{H}_{zz} = \sum_{j=1}^{N}\sum_{k>j}^{N} B_{jk}\left(2I_{z_j}I_{z_k} - \frac{1}{2}(I_j^+I_k^- + I_j^-I_k^+)\right) \tag{5.19}$$

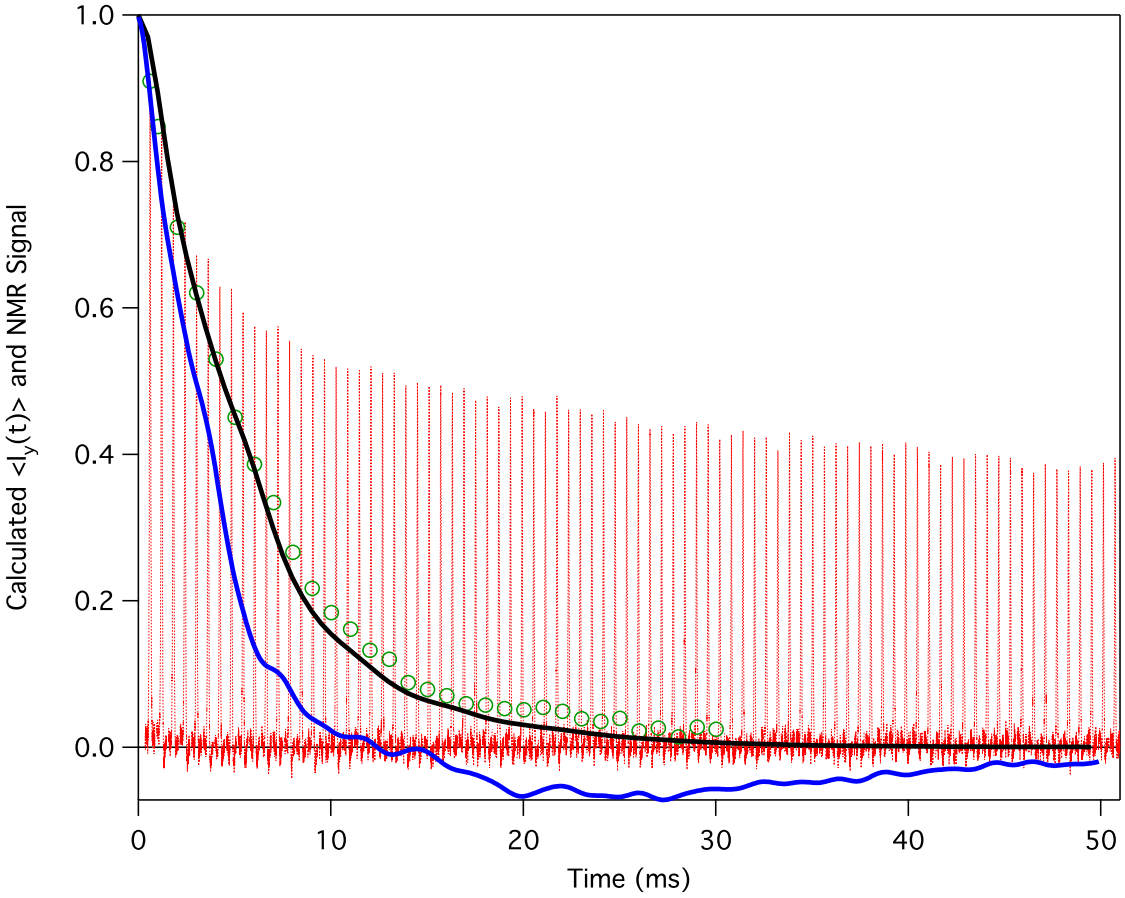

Figure 5.2: Expected decay curves for the delta-function pulse approximation using $\mathcal{H}_{zz}$ (blue curve) and $\mathcal{H}_{\text{Ising}}$ (black curve). The blue curve uses clusters of $N = 9$ spins and disorder-averages over 1,000 DRs. The black cure uses $N = 80$ spins and averages over 20,000 DRs. Both calculations use the realistic silicon lattice (4.67% natural abundance of spin-1/2 ^{29}Si nuclei, diamond lattice constant 5.43 Å). Hahn echo data (green circles) and the CPMG echo train (dashed red lines) from Figure 4.1 are plotted in the background for comparison.

by defining the raising and lowering operators

$$\begin{aligned} I^+ &= I_x + iI_y \\ I^- &= I_x - iI_y. \end{aligned}$$

We call $I_j^+ I_k^-$ and $I_j^- I_k^+$ the flip-flop terms. These terms flip one spin up and flop another spin down while conserving the total angular momentum [79].

It is a very good approximation to drop the flip-flop terms whenever spins within a cluster have quite different Zeeman energies. In this case, the flip-flop would not conserve energy so this process is inhibited [79]. In that limit, $\mathcal{H}_{zz}$ is truncated to the Ising model Hamiltonian with long-range interactions

$$\mathcal{H}_{\text{Ising}} = \sum_{j=1}^{N} \sum_{k>j}^{N} 2B_{jk} I_{z_j} I_{z_k}. \tag{5.20}$$

This approximation is usually made when considering the dipolar coupling between different spin species. [79] In the homonuclear systems that we consider, this approximation is not usually justified but we consider this limit here for comparison.

Using $\mathcal{H}_{\text{Ising}}$, the product operator formalism [81] enables us to analytically evaluate $\langle I_{y_1}(t) \rangle$ for the central spin

$$\langle I_{y_1}(t) \rangle = I_{y_1}(0) \prod_{k>1}^{N} \cos(B_{1k} t/\hbar). \tag{5.21}$$

Since the expression in equation (5.21) is analytic [47], the calculation of the resultant curve [Figure 5.4(black curve)] is not as computationally intensive as time-evolving the entire density matrix. This calculation only requires the the numerical value of the dipolar coupling B_{1k} between the central spin and a random population of $N-1$ spins on the lattice. In this way, many more spins can be treated. The final step is a disorder average over many random lattice occupancies and random lattice orientations.

Despite the differences in the two approaches, the simulated curves for the same lattice parameters are in reasonable agreement. The initial decay due to the secular dipolar Hamiltonian is two-thirds faster than the decay due to the Ising Hamiltonian in agreement with second-moment calculations [47, 79, 89, 56]. The Hahn echo experiment in this sample

follows the Ising model decay curve [Figure 5.4(green circles vs black curve)]. In other samples we have studied, the Hahn echo data lies between the calculated blue and black curves but always decays to zero. It is surprising then that the CPMG experiment has measurable coherence well beyond the decay predicted by either approach [Figure 5.4(red lines)].

Chapter 6

Exploring Experimental Imperfections

Because of the surprising results of the preceding section, we performed many experiments to test whether certain extrinsic factors were to blame for the surprising experimental data reported in Chapter 3. In this chapter, we show that even after greatly improving our experimental pulses, the tail of the CPMG echo train persists well beyond the decay of the Hahn echoes. We also report experiments with many different sample parameters that all yield the same surprising results.

These experiments are quite different from the usual array of NMR experiments that primarily focus on optimizing the signal-to-noise ratio. In contrast, we have plenty of signal to observe in the CPMG echo train, but our aim was to find any sensitivity of the CPMG tail height on some extrinsic parameter. Although deliberately imposing a large pulse imperfection may lead to NMR data that look qualitatively similar to those outlined in the previous section, experimental improvements that greatly reduced these imperfections did not make the effects vanish.

6.1 Nutation Calibration, Rotary Echoes, and Pulse Adjustments

Without proper pulse calibration it is difficult to predict the result of any NMR experiment. We calibrate the rotation angle of a real finite pulse through a series of measurements resulting in a nutation curve [85]. This experiment begins with the spins in the Boltzmann equilibrium $\rho_B = I_{z_T}$. During a square pulse of strength $H_1 = \omega_1/2\pi$ and time duration

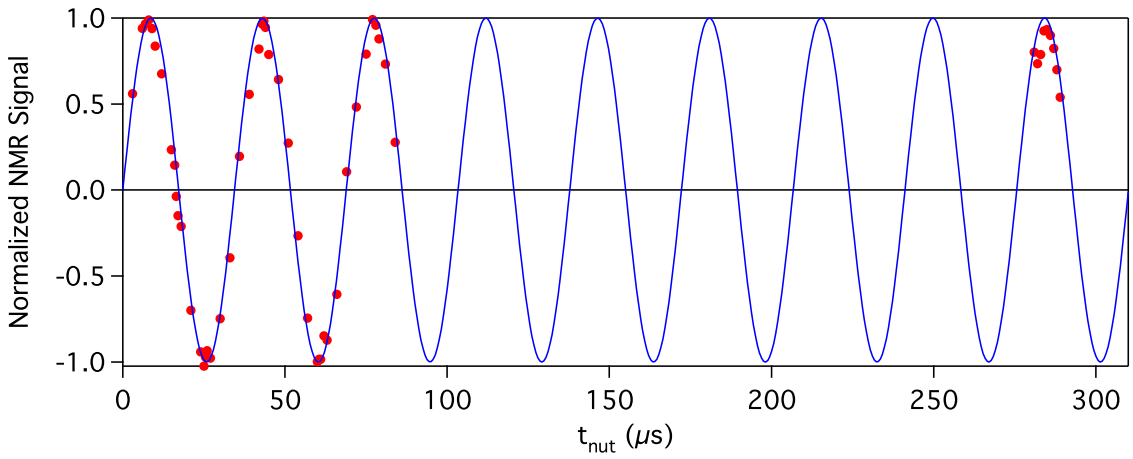

Figure 6.1: Nutation curve data (dots) of ^{29}Si in Si:Sb (2.75×10^{17} Sb/cm^3) agree with a non-decaying sine curve over 8.25 cycles. $H_1 = 8.33$ kHz, $T = 300$ K, and $B^{\rm ext} = 12$ Tesla.

$t_{\rm nut}$ applied along $\hat{x}$ in the rotating frame, the spins will nutate in the y-z plane. Shortly after $t_{\rm nut}$, the projected magnetization along $\hat{y}$ is measured as the initial height of the FID.

Figure 6.1 shows a typical nutation curve in Si:Sb (10^{17} Sb/cm^3). The π pulse is determined by the timing of the first zero-crossing of the nutation curve. This nutation calibration is typically repeated several times during a long experiment.

The nutation curve is also a measure of the quality of other aspects of the single-pulse experiment [36]. For example, the homogeneity of the applied rf field may be inferred from the decay of the nutation curve after several cycles. Figure 6.1 shows nutation data out to over eight cycles with very little decay. Extending the nutation experiment out to even longer pulse times (Figure 6.1) enables the study of the decay of its amplitude.

For such long nutation times, the dipolar coupling between spins contributes to the decay [5]. This decay is calculated using the density matrix evolved under the time-evolution operator for the full pulse [equation (5.8)] for time $t_{\rm nut}$. The expected decay envelope [Figure 6.1(dashed curves)] is the disorder-averaged expectation value $\langle I_{y_1}(t)\rangle = {\rm Tr}\{\rho(t) I_{y_1}\}$.

Another significant contribution to the decay of the nutation curve is rf field inhomogeneity. For a given spread of rf fields, the decay of the NMR signal depends on the number of nutation cycles, therefore, a nutation with a weaker H_1 [Figure 6.1(top)] will decay slower than a nutation with a stronger H_1 [Figure 6.1(middle)]. The damped sine curves include the contribution from dipolar coupling and add the spatial rf field variations due to

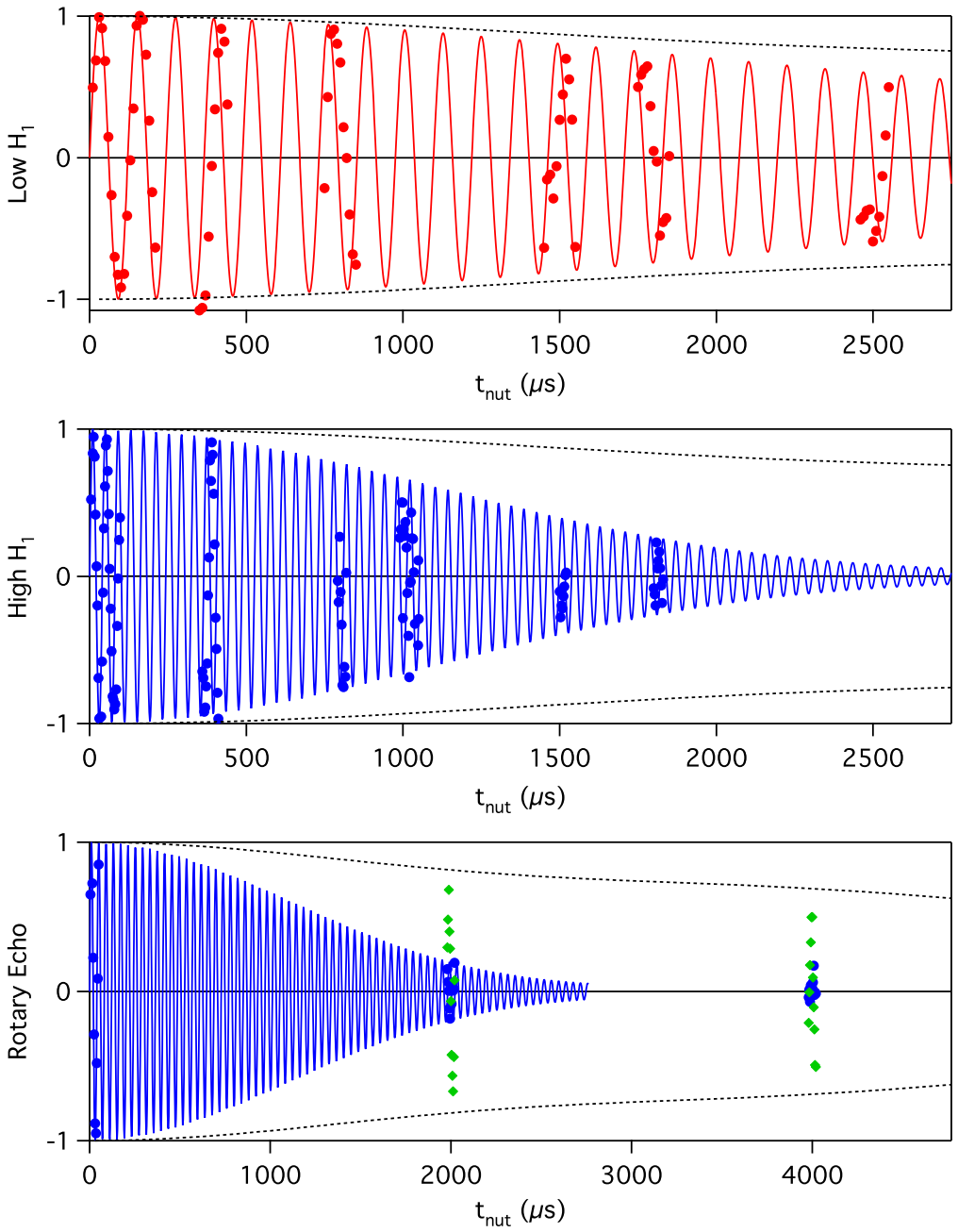

Figure 6.2: Extended nutation data of ^{29}Si in Si:Sb (2.75×10^{17} Sb/cm^3) taken at room temperature in a 12 Tesla field. (Top) $H_1 = 8.33$ kHz. (Middle) $H_1 = 25$ kHz. (Bottom) Rotary echo data (green dots) and nutation data (blue dots) for $H_1 = 25$ kHz. Dashed lines in each graph show the expected decay envelope due to dipolar coupling during the nutation pulse. Solid traces are calculations that include the dipolar decay, rf field spread from our NMR coil, and skin depth of Si:Sb.

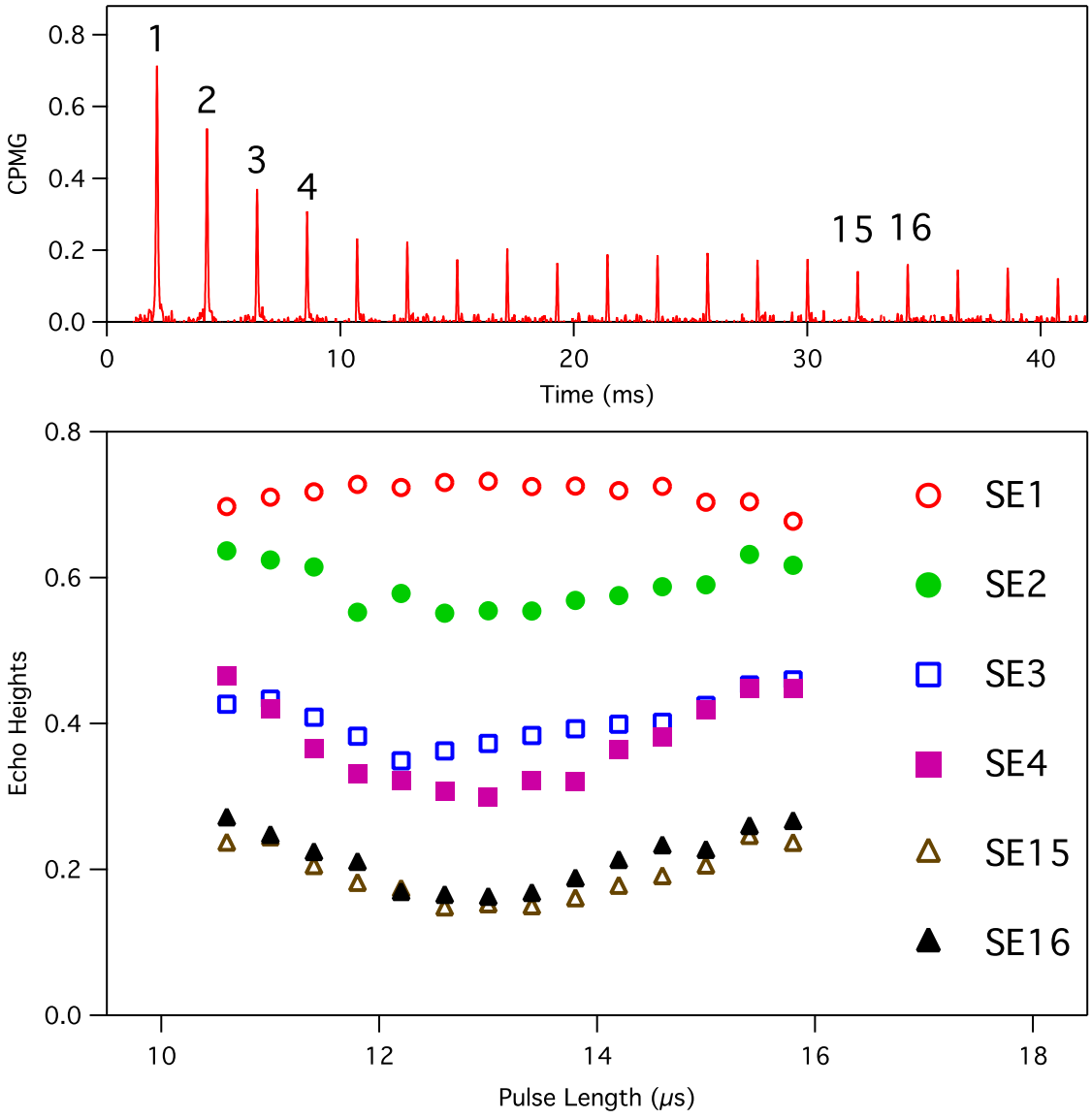

Figure 6.3: Finding the minimum tail height for CPMG. (Top) CPMG data of ^{29}Si in Si:P (3.94×10^{19} P/cm^3) with $2\tau = 2.192$ ms. (Bottom) Numbered spin echoes (SEn) are plotted versus π pulse duration. SE15 and SE16 are expected to have zero amplitude. The nutation calibrated π pulse has duration 12.2 μs. Data taken at room temperature in a 12 Tesla field.

the calculated sample skin depth and the inherent inhomogeneities of our NMR coil.

The rotary echo experiment [80] compensates for static spatial rf field inhomogeneities by reversing the phase of the nutation pulse at a time near $t_{\rm nut}/2$. Using this technique, the rotary echo data [Figure 6.1(green dots) approach the dipolar decay envelope even though the nutation data [Figure 6.1(blue dots) decay much faster.

So far, the Hahn echoes, the nutation curve, and rotary experiment all agree with the model for calculating the NMR signal developed in Chapter 4. One significant difference between these experiments and the CPMG sequence is that they consist of only one or two applied pulses while the CPMG sequence has many pulses. It is possible that the calibration for the CPMG sequence could be different then that set by the nutation curve. We explored this question of calibration by varying t_p of the π pulse to see if the expected decay would be recovered. Figure 6.1(bottom) plots a series of echoes from the CPMG sequence versus the misadjusted π pulse duration. Spin echo 15 (SE15) and spin echo 16 (SE16) are representative of coherence that should decay to zero for delta-function π pulses. Despite the wide range of pulse durations attempted, the tail of the CPMG echo train never reached zero. Modifying CPMG with more complicated pulse phase patterns [25, 76] changes the results, but echoes at long times are still observed.

6.2 RF Field Homogeneity

If the strength of the rf field during a pulse greatly varied from spin to spin, then the pulse calibration would not be consistent across the sample. To test whether this extrinsic effect could cause the results of Chapter 3, we examined the rf field homogeneity in our NMR coil and made improvements by modifying the sample.

An ideal delta-function pulse affects all spins in the system with the same rf field strength. However, a real NMR coil is a short ($\sim$10 turn) solenoid with rf fields that vary in space [30]. Figure 6.2 shows a calculation of the rf field homogeneity in the quasi-static approximation using the Biot-Savart law for our seven-turn NMR coil [33, 66]. The grayscale plot indicates the spatial variation of rf fields where lighter colored regions are areas of higher rf field strength. The proximity effect would slightly smooth out these rf fields beyond what is shown [10, 30, 84].

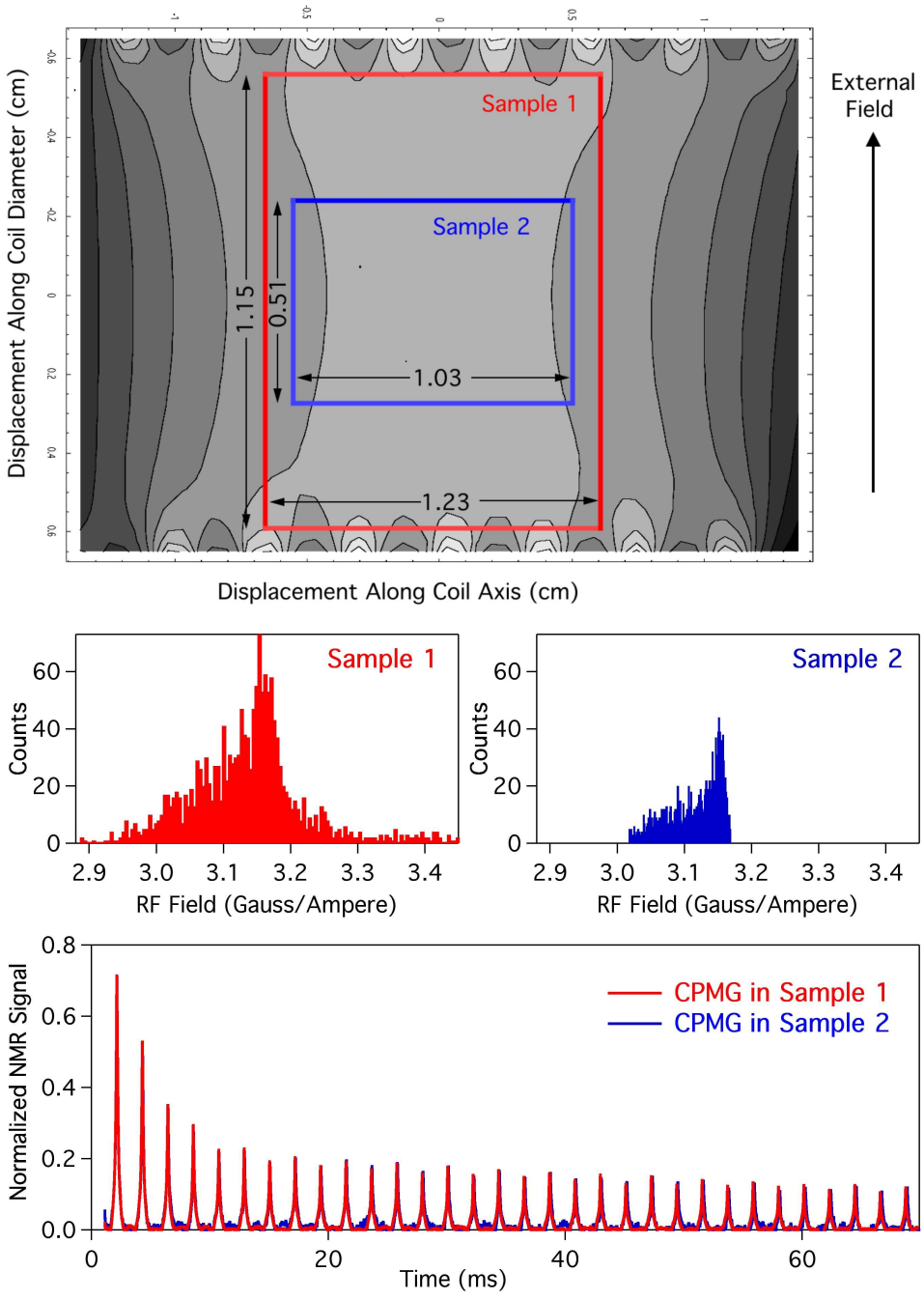

Figure 6.4: (Top) Sectional calculation of the rf field homogeneity in our NMR coil. Two cylindrical sample sizes are outlined. (Middle) Histograms of rf field strength distribution. (Bottom) CPMG data for the two sample sizes of ^{29}Si in Si:P (3.43×10^{19} P/cm^3) are nearly identical despite the noticeable change in rf field homogeneity. $2\tau = 2.192$ ms, $T = 300$ K, and $B^{\text{ext}} = 7$ Tesla.

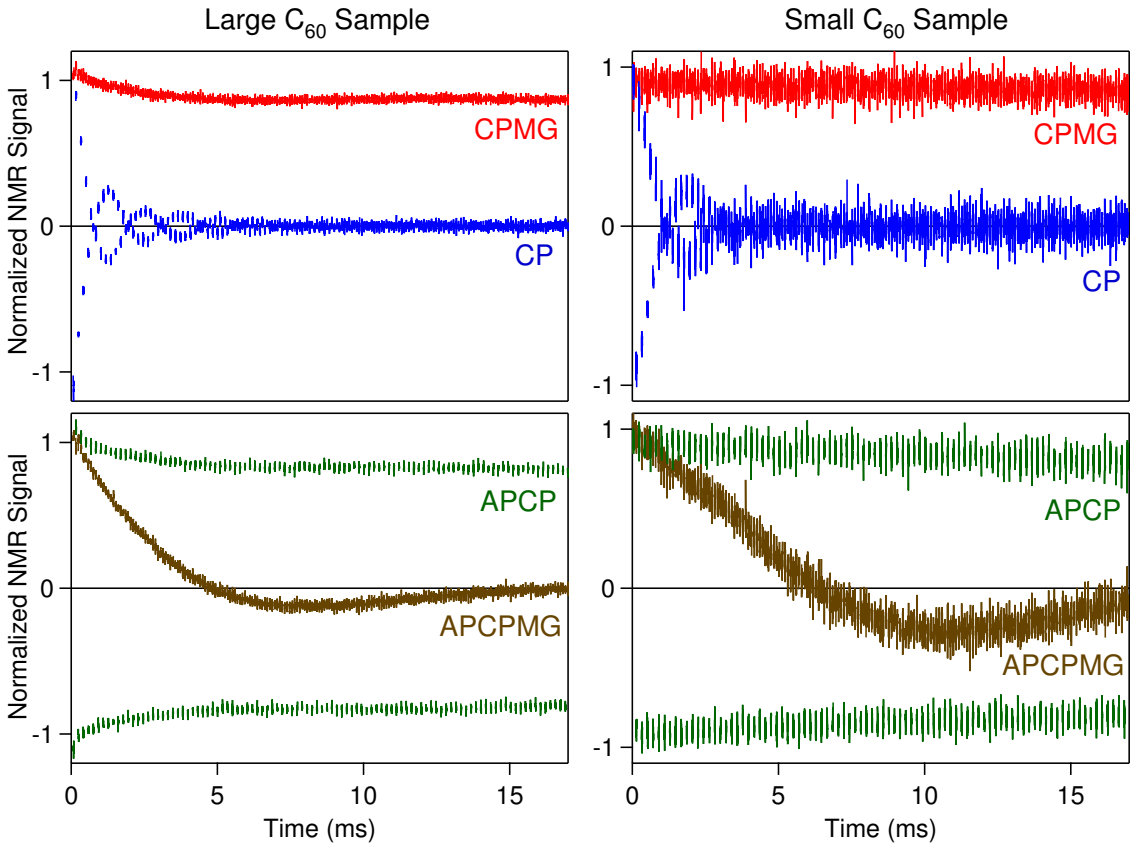

Figure 6.5: Pulse phase sensitivity and rf homogeneity tests in an insulating sample. CP, CPMG, APCP, and APCPMG data of ^{13}C in C_{60} for a large sample volume (left column) and a small sample volume (right column). All are expected to agree in the delta-function pulse limit. $H_1 = 45.5$ kHz, ^{13}C NMR linewidth $= 290$ Hz, $2\tau = 180$ μs, $T = 300$ K, $B^{\text{ext}} = 12$ Tesla.

For a given coil, the rf field homogeneity can be improved by decreasing the sample volume. To this end, we performed experiments using two different sample sizes to assess the influence of rf homogeneity on the long tail in the CPMG echo train. Figure 6.2 shows histograms of the rf field distribution within the two sample sizes and the corresponding CPMG echo trains. These rf field calculations were performed by Kenneth MacLean. No noticeable difference in the tail height was observed despite the marked improvement of rf homogeneity.

In addition to the coil dimensions, the sample itself may have properties that introduce an rf field inhomogeneity. For example, the skin depth in metallic samples attenuates the rf field inside the sample [33, 66, 82]. Two approaches were taken to reduce the contribution of skin depth effects to the rf field homogeneity. In the first approach, a sample of highly doped Si:P (10^{19} P/cm^3) was ground, passed through a 45 μm sieve, and diluted in paraffin wax. This high-doped silicon sample has a resistivity of 0.002 Ohm-cm. At a 12 Tesla field the rf frequency applied is 101.5 MHz. Thus the skin depth at this frequency is 223.3 μm. Particle diameters on the order of 45 μm would only have a 10% reduction of the field at the center. Furthermore, dilution in wax helps to separate the particles. Despite this improvement, the effects summarized in Chapter 3 remained.

The second method to reduce the rf field attenuation caused by skin depth is to use less metallic samples. Four different silicon samples were used that differ in dopant type (donors or acceptors) and dopant concentrations (up to a factor of a million less for Si:P with 10^{13} P/cm^3). For samples doped below the metal-insulator transition [82], the calculated skin depth is very large and the rf field attenuation at the center of the particle is much smaller. For example, Si:Sb (2.75×10^{17} Sb/cm^3) has a skin depth of 1.05 mm, which reduces the H_1 field by 2% at the center of a 45 μm particle. Si:P13 (resistivity 0.97 Ohm-cm to 2.90 Ohm-cm) has a skin depth range of 4.92 cm to 8.50 cm, which results in a less than 0.03% reduction in rf field at the particle center. Additionally NMR of ^{13}C in C_{60}, and ^{89}Y in Y_2O_3, two insulating samples, show the same behavior as in silicon [45, 14, 21].

Figure 6.2 shows the four pulse sequences in C_{60} for two sample sizes. Similar data was taken in other samples. This data in particular was taken by Rona G. Ramos. Despite the improvement in rf field homogeneity, the long tail in the CPMG echo train and the pulse sequence sensitivity are largely unaffected.

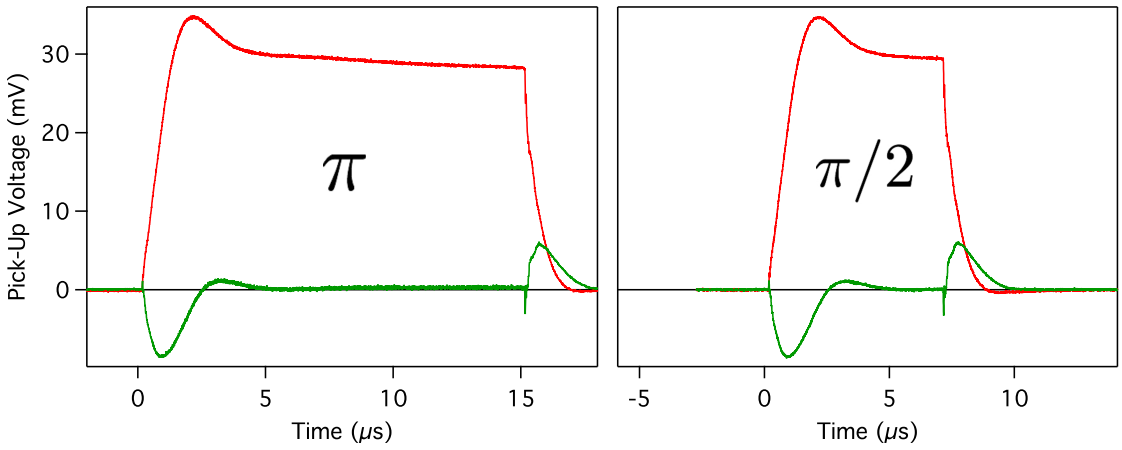

Figure 6.6: Measured pulse shapes in-phase (red) and out-of-phase (green) for a typical π pulse (left) and $\pi/2$ pulse (right) at radio frequency 101.5 MHz with pulse strength $H_1 = 33.3$ kHz. Transients are a larger fraction of short duration pulses like $\pi/2$. Data taken at room temperature in a 12 Tesla field. The real π pulse is approximated as three pure rotations $4_{\bar{X}}180.1_Y3_X$.

6.3 Measuring the Pulse Transients

Pulse transients are another possible source of experimental error [49, 57, 91, 92]. In principle, the perfect pulse is square and has a single rf frequency. In practice, however, the NMR tank circuit produces transients at the leading and trailing edges of the pulse. Because the pulse transients have both in-phase and out-of-phase components, they can cause spins to move out of the intended plane of rotation. These unintended transients can contribute to poor pulse calibration and possible accumulated imperfections. Therefore, it is important to quantify the pulse transients specific to our apparatus.

To measure the real pulse, we inserted a pickup loop near our NMR coil and applied our regular pulses [49, 57, 91]. Figure 6.3 shows the typical π pulse and $\pi/2$ pulse envelopes. The red traces show the in-phase components of the pulses while the green traces show the out-of-phase components. Empirically, changing parameters like the resonance and tuning of the NMR tank circuit changes the shape of the transients and even the sign of the out-of-phase components.

For short time pulses (e.g. a $\pi/2$ pulse), the transient constitutes a larger fraction of the entire pulse. Consequently, the dominate pulse transient in these short pulses could lead

to larger extrinsic effects. Furthermore, since $H_1 t_p = 1/2$ is fixed for π pulses, one would expect that any extrinsic effects caused by pulse transients would also be larger for stronger (i.e. shorter in time) π pulses.

The affect of the pulse transients on the multiple pulse sequences may be simulated [92] by approximating the real π pulse along $\hat{y}$ as a composite pulse of three pure rotations $180_Y \rightarrow 4_{\bar{X}} 180.1_Y 3_X$. Including the pulse transients in simulation yielded only small changes in the expected decay envelope derived in Chapter 4 and could not reproduce the effects from Chapter 3.

While the pulse transients are sensitive to many changes in our NMR apparatus, the observed effects in from Chapter 3 are qualitatively insensitive. Therefore, we infer that the pulse transients are not the dominant cause of these effects.

6.4 Pulse Strength Dependence

How strong does a real pulse need to be in order to be considered a delta-function pulse? The limit described in Chapter 4 assumes pulses of infinite strength. This limit ensures that all the spins are rotated identically. On the other hand, weak pulses treat different spins differently. Thus, if the calibration, rf field homogeneity, or pulse strength were grossly misadjusted [32], then the observed behavior could deviate from the calculation in Chapter 4.

However, Figure 6.4 shows CPMG experiments in Si:Sb (10^{17} Sb/cm^3) for a variety of pulse strengths. The tail height is extrapolated as a $t = 0$ intercept from the CPMG pulse sequence [Figure 6.4(top)] and plotted versus the rf field strength $H_1 = \omega_1/2\pi$ normalized by the full-width-at-half-maximum (FWHM) of the Si:Sb lineshape. For each data point, a separate nutation curve was measured to calibrate the π pulse. The tail height of the CPMG echo train is largely insensitive to the pulse strength for H_1/FWHM from 4 to 450.

The expected CPMG decay may be simulated using finite pulses [101] in an exact calculation for $N = 5$ spins in silicon [Figure 6.4(bottom, open blue triangles)]. These calculations agree with the data when the pulses are extremely weak (H_1/FWHM< 1) but quickly fall to zero once the pulses are over ten times the linewidth. Thus, these calculations agree with the conventional assumption that the strong pulse limit is achieved when H_1/FWHM

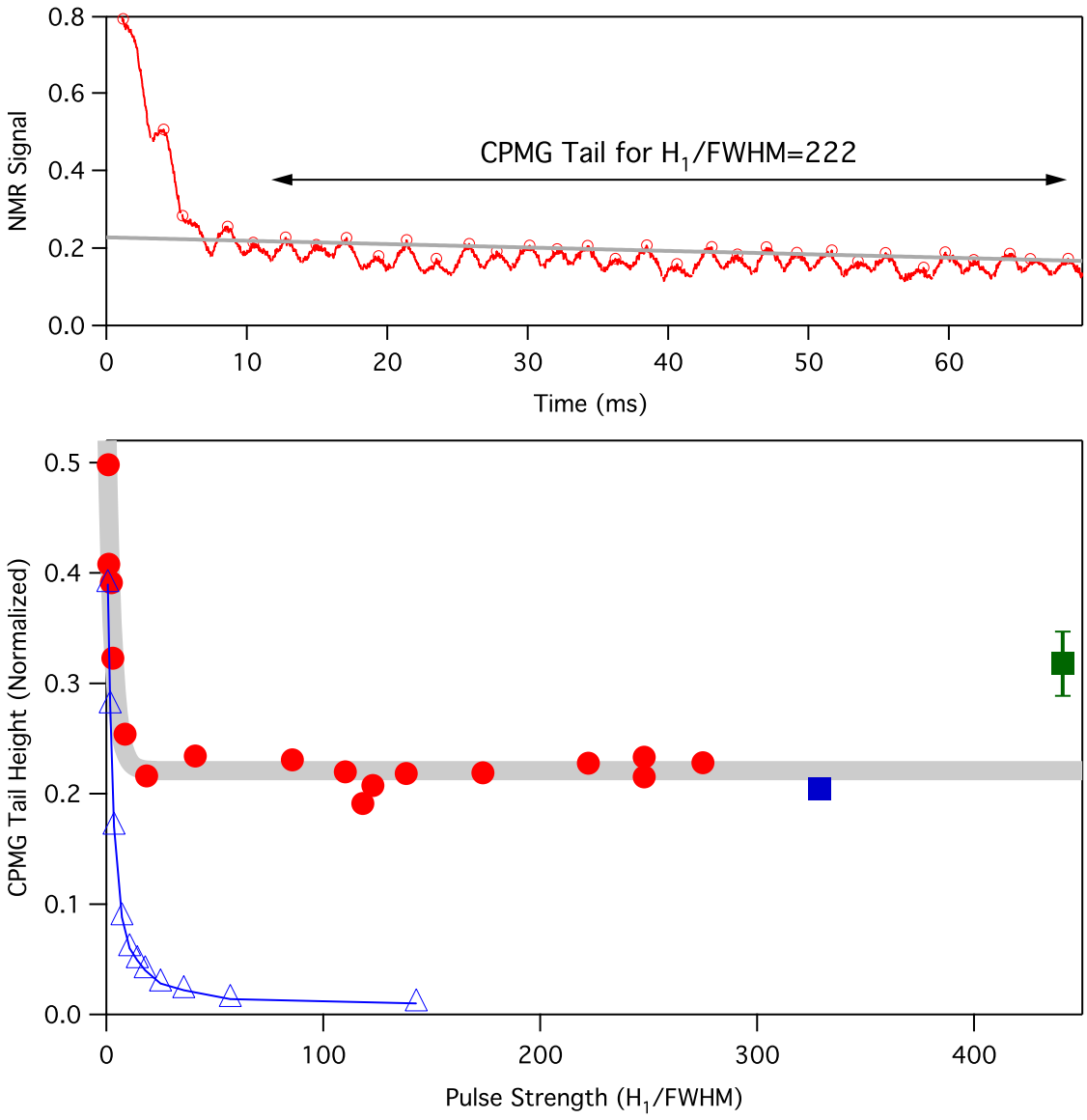

Figure 6.7: Dependence of CPMG tail height on pulse strength. (Top) Tail height is extrapolated as a $t = 0$ intercept for CPMG of ^{29}Si in Si:Sb (2.75×10^{17} Sb/cm^3) with $2\tau = 2.192$ ms. This example is for H_1/FWHM$= 222$. (Bottom) CPMG tail height versus pulse strength. Smaller samples and NMR coils were used to achieve the last two points. Exact calculations for $N = 5$ spins in silicon (triangles) decay to zero for $H_1 >$ FWHM.

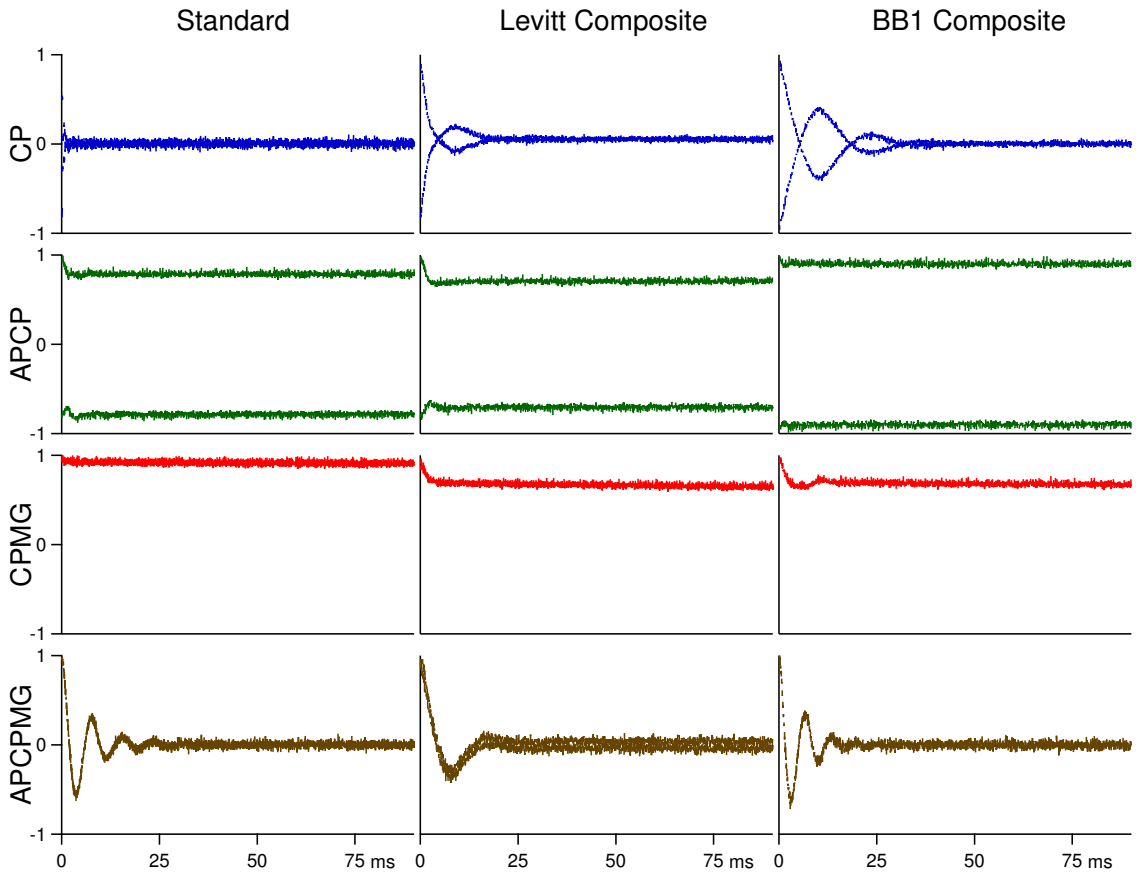

Figure 6.8: Pulse sequences CP, APCP, CPMG, and APCPMG using standard π pulses (left column), Levitt composite π pulses (middle column), and BB1 composite π pulses (right column). $H_1 = 35.7$ kHz, $2\tau = 72$ μs, $T = 300$ K, $B^{\text{ext}} = 11.74$ Tesla.

$\gg 1$, a limit that is easily achieved in our experiments.

Because the experimental tail height in CPMG is so insensitive to large changes in pulse strength, we conclude that strong π pulses are not the same as delta-function pulses.

6.5 Using Composite π Pulses to Improve Pulse Quality

Another way to improve pulse quality is to use composite pulses [18, 22, 43] in place of single π pulses. Composite pulses were designed to correct poor pulse angle calibration, rf inhomgeneity, and the effects of weak pulses [87] by splitting a full rotation into separate rotations about different axes. These separate pieces counteract pulse imperfections when

strung together.

Figure 6.5 shows a series of experiments where the single π pulses in CP, APCP, CPMG, and APCPMG are replaced by composite pulses. The Levitt composite pulse [44, 43] makes the replacement

$$\text{Levitt} : 180_Y \rightarrow 90_X 180_Y 90_X. \tag{6.1}$$

The BB1 composite pulse [13, 99] makes the replacement

$$\text{BB1} : 180_Y \rightarrow 180_\alpha 360_\beta 180_\alpha 180_Y \tag{6.2}$$

where $X = 0°$, $Y = 90°$, $\alpha = 194.5°$, and $\beta = 43.4°$. Even though these composite pulses should improve pulse quality [13], the CPMG tail height and the sensitivity to π pulse phase is hardly affected. I am grateful for the help from John D. Murray and Kurt Zilm for these experiments.

Chapter 7

Exploring External Dynamics of the System

More experimental exploration was done to find sources of unusual coherence or decoherence in the samples themselves. In this chapter, we continue our search for experimental or material parameters that are commonly thought to alter the NMR signal.

7.1 Absence of Non-Equilibrium Effects

This experiment tests the assumption made in Chapter 4 that the equilibrium density matrix is simply $\rho_B = I_{z_T}$. This ρ_B assumes that equilibrium is reached after waiting longer than the spin-lattice relaxation time T_1 before repeating a CPMG sequence [79]. If, however, an experiment is started out of equilibrium, then any unusual coherences [42, 96] present in the initial density matrix might lead to a different NMR signal.

Figure 7.1 shows the CPMG echo train in two regimes. In red, the CPMG echo train is repeated after waiting only a fifth of the spin-lattice relaxation time T_1. In blue, the CPMG echo train is repeated after waiting $5 \times T_1$. Inset (a) shows the saturation-recovery data that determines T_1. A single exponential is a good fit to the data supporting the assumption of a single mechanism for spin-lattice relaxation. Inset (b) shows a close-up of echoes for the two wait times. For shorter wait times, the echo shape is slightly distorted at the base of the echoes compared to the much longer wait times. However, the CPMG echo peaks still exhibit a long tail and is insensitive to the wait time.

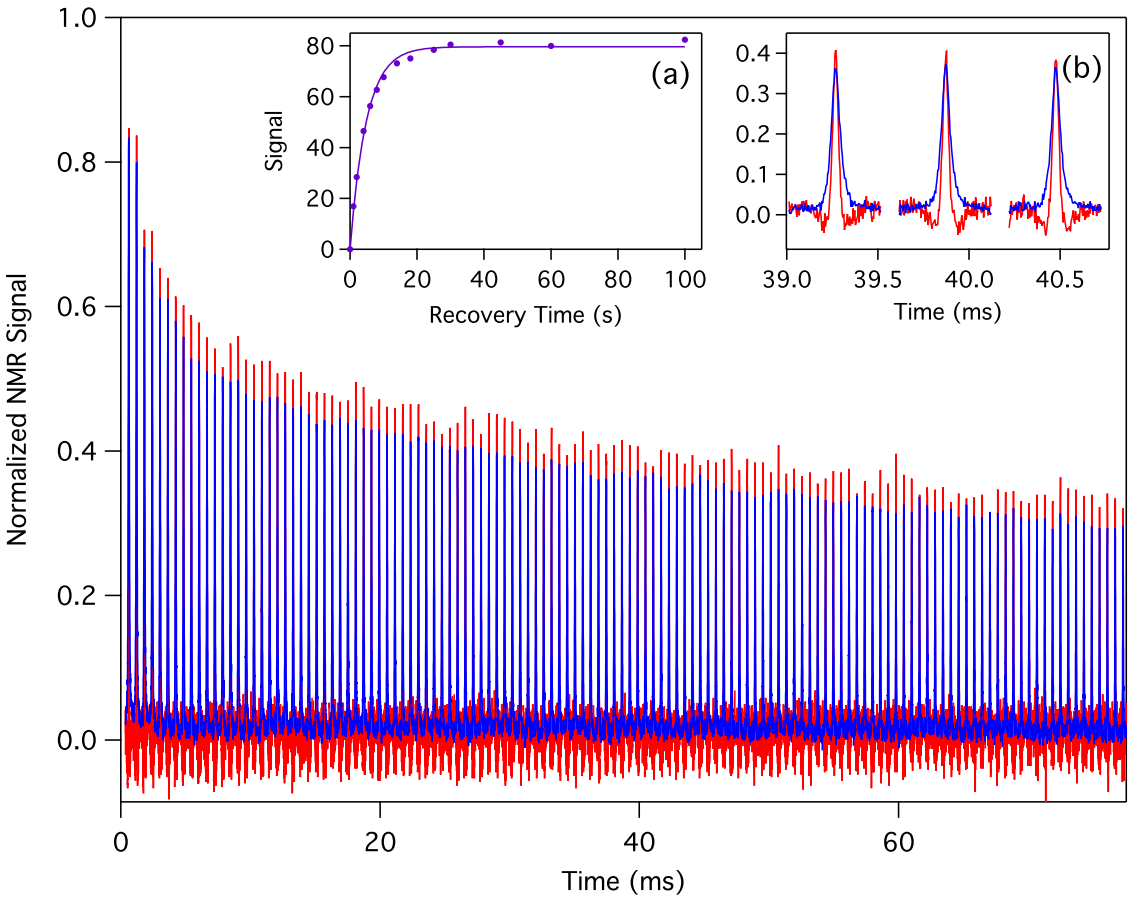

Figure 7.1: Non-equilibrium effects and spin-lattice relaxation. (Main) CPMG echo train for ^{29}Si in Si:P (3.94×10^{19} P/cm^3) with saturation recovery time $t_{\rm rec} = 1$ s (red) and $t_{\rm rec} = 20$ s (blue). $T = 300$ K, $B^{\rm ext} = 12$ Tesla, $2\tau = 592$ μs. The initial height of the FIDs are scaled to agree. (a) Exponential fit to the saturation recovery experiment gives $T_1 = 4.9$ s in this sample (b) Close-up of echo shapes.

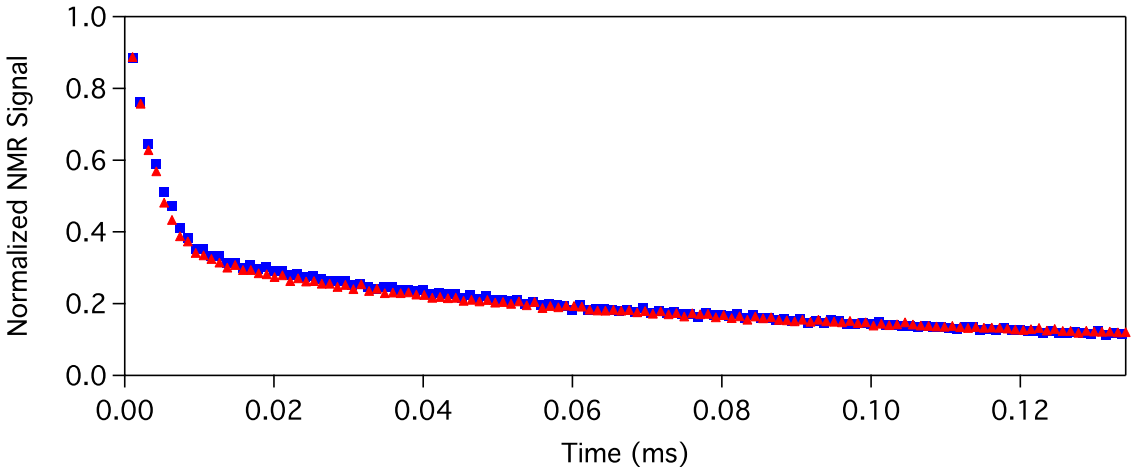

Figure 7.2: Temperature effects on CPMG tail height. CPMG echo peaks at room temperature (red) and 4 Kelvin (blue) in Si:P (3.94×10^{19} P/cm^3) diluted in paraffin wax. $2\tau = 2.192$ ms, $B^{\text{ext}} = 12$ Tesla.

7.2 Absence of Temperature Dependence

The CPMG tail height could be sensitive to both temperature-dependent effects specific to each sample and temperature-independent effects found in all dipolar systems. To distinguish between the two sets of effects, we performed the CPMG pulse sequence in Si:P (10^{19} P/cm^3) at room temperature and at 4 Kelvin. Figure 7.2 shows that the CPMG tail height is insensitive to the large change in temperature.

These results update previously reported data in the same sample [14]. Lowering the temperature increases the spin-lattice relaxation time T_1 from 4.9 seconds at room temperature to over 6 hours at 4 Kelvin. As a consequence, the increased T_1 at low temperatures required us to perform experiments at a much slower rate where our NMR tank circuit would be susceptible to temperature instabilities. These temperature instabilities caused poor pulse calibration from time to time. To rectify this problem, we repeated the CPMG pulse sequence many times at 4 Kelvin and measured the nutation curve after each repetition. If the calibration remained consistent between four applications of the CPMG pulse sequence, we averaged the four scans together to obtain the 4 Kelvin data in Figure 7.2(blue squares). None of these issues were present in the room temperature data.

In addition, the sample was carefully prepared by sieving the crushed powder to < 45

Sample	$\gamma/2\pi$ (MHz/Tesla)	n.a. (%)	T_1 (s)
^{13}C in C_{60}	10.7	1.11	25.8
^{29}Si in Si:P (10^{13})	8.46	4.67	17640
^{29}Si in Si:B (10^{16})	8.46	4.67	10080
^{29}Si in Si:Sb (10^{17})	8.46	4.67	276
^{29}Si in Si:P (10^{19})	8.46	4.67	4.9
^{89}Y in Y_2O_3	2.09	100	8280

Table 7.1: Dipolar solids used in these studies and their NMR spin-1/2 nucleus, gyromagnetic ratio (γ), natural abundance (n.a.), and spin-lattice relaxation time (T_1).

μm and diluting it in paraffin wax to reduce the skin depth effect and to reduce clumping when cooling in a bath of liquid helium.

Absence of temperature dependence supports the assumption that the relevant internal Hamiltonian is $\mathcal{H}_{int} = \mathcal{H}_Z + \mathcal{H}_{zz}$.

7.3 Similar Effects Found in Different Dipolar Solids

We performed the same pulse sequences in many different dipolar solids to show that the effects reported in Chapter 3 are universal. Table 7.3 summarizes the samples used in these studies and outlines dramatically different features including the T_1, which varies from 4.8 seconds to 5.5 hours at room temperature [45, 14]. Measurements in a variety of silicon samples with different doping concentrations, different dopant atoms, and even different dopant types (N-type and P-type) show the same qualitative results despite the significant differences in their local environments (Figure 7.3). These experiments, although time consuming, contributed significantly to our understanding of the universality of the effects. These experiments in silicon ultimately led us to believe that the results would be observable in any spin-1/2 system, and probably even in pseudo-spin systems.

We also performed the same NMR pulse sequences on different nuclei [45]. The CPMG echo trains of ^{13}C in C_{60} have long tails that outlast both the measured Hahn echoes and the predicted decay when calculated using the Ising model and delta-function π pulses.

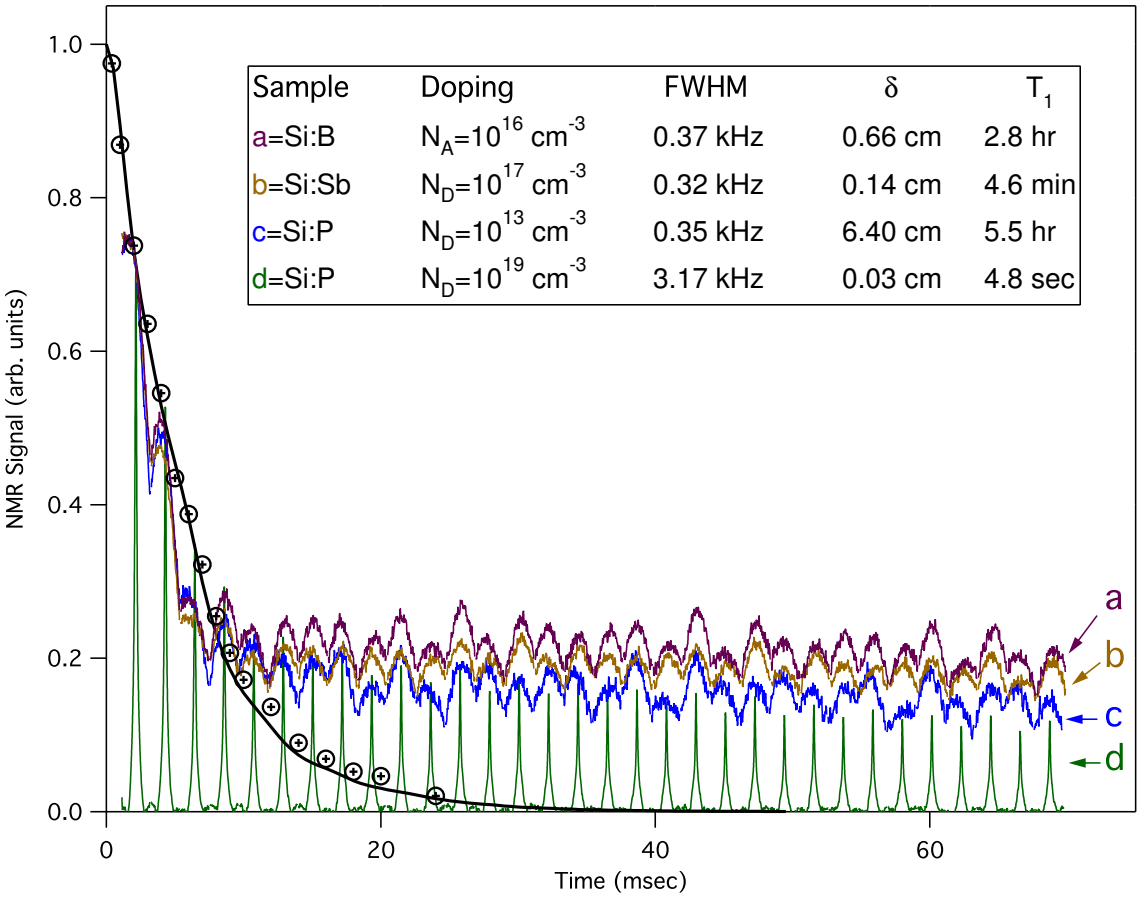

Figure 7.3: CPMG echo trains in four different doped silicon samples. All CPMG echo trains exhibit the same long-lived coherence despite many changes in their local environments. The Hahn echoes (open symbols) decay with the delta-function pulse approximation in all four samples (shown is Hahn echo data for Si:P 10^{19} P/cm^3). The inset table summarizes the different doping concentration, doping type, spectral full widths at half maximums (FWHM), skin depths (δ), and spin-lattice relaxation times (T_1).

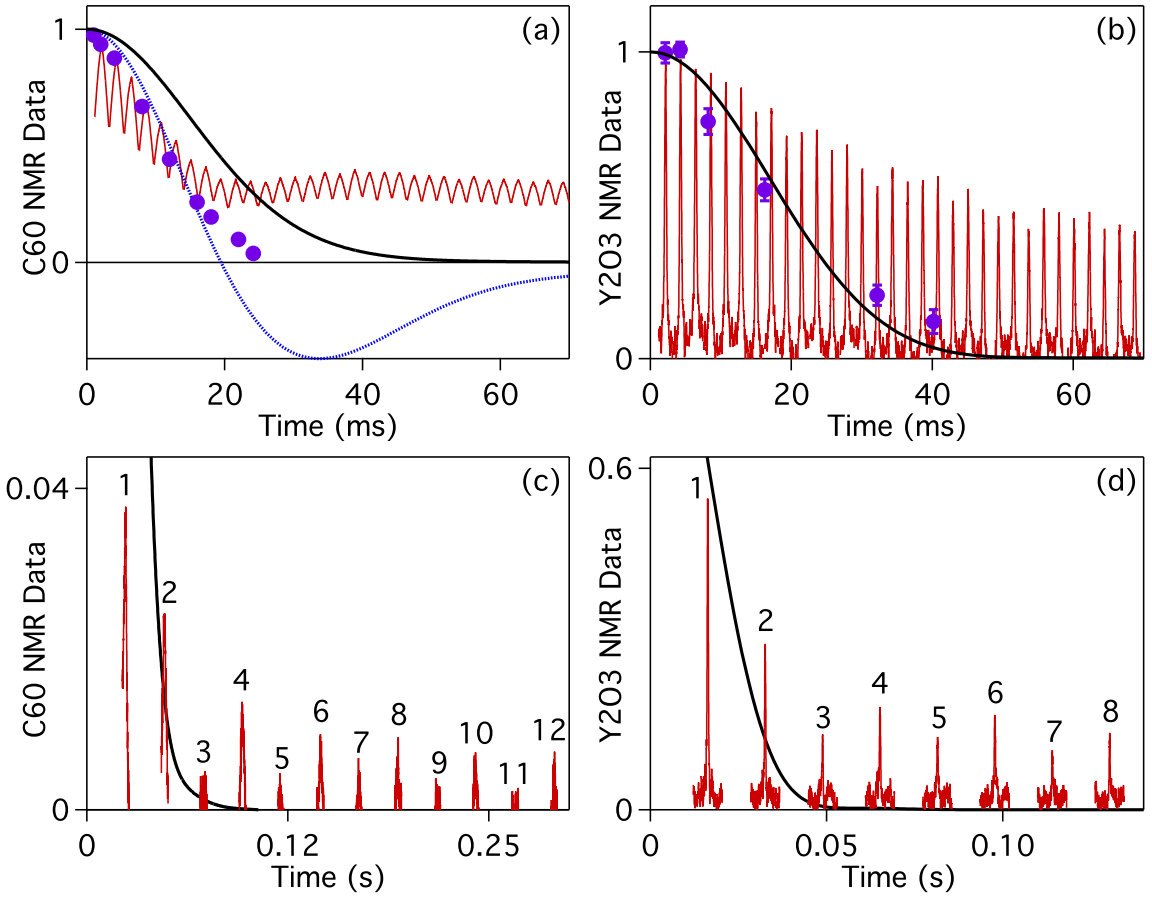

Figure 7.4: NMR measurements of ^{13}C in C_{60} (a), (c) and 89Y in Y_2O_3 (b), (d). Experimental parameters: $T = 300$ K, $B = 12$ Tesla, spin-lattice relaxation time $T_1 = 26$ s (C_{60}), 2.3 hr (Y_2O_3). The dots in (a) and (b) are Hahn echo peaks while the red lines are CPMG echo trains. Simulated dipolar decay curves are shown for comparison (black and blue). Note the long tail for short interpulse spacings (a) and (b) and the even-odd effect for long interpulse spacings (c), (d).

Furthermore, we see the same qualitative results for ^{89}Y in Y_2O_3. Because the natural abundance (n.a.) of ^{89}Y is 100%, dilution of the spins on the lattice does not contribute to the results [20, 37].

Additionally, at room temperature, C_{60} molecules form an fcc lattice, and each C_{60} undergoes rapid isotropic rotation about its lattice point [86, 100]. This motion eliminates any inter-C_{60} J coupling[79] but leaves the dipolar coupling between spins on different buckyballs. Thus the J coupling, which we have not included in $\mathcal{H}_{\rm int}$ [equation (5.6)], does not play a major role in the results [2, 22].

As Figure 7.4 shows, the even-odd effect as well as the long tail in CPMG can be seen in any spin system. The scale of the dipolar coupling sets the transition in interpulse spacing where the long tail in CPMG changes to the even-odd effect in the heights of the echoes. Phenomenologically, we have found that this transitional π pulse spacing occurs near T_2 as calculated by the delta-function pulse approximation. Coincidentally, in the case of ^{13}C IN C_{60}, this timing was around 20 ms, which is the about the same for ^{89}Y in Y_2O_3. However, for ^{29}Si in doped silicon, this transitional time was around 6 ms. In protons, we find the transition time at around 1 ms [67].

7.4 Single Crystal Studies

In order to reduce the effects of skin depth [33, 66, 82], most of our samples were ground to a powder. The calculations outlined in Chapter 4 took this into account in the disorder average by configuring each disorder realization with a random orientation of the lattice with respect to $\vec{B}^{\rm ext}$. Then, by picking small clusters of N spins, each disorder realization was designed to represent a realistic cluster in any one powder particle.

The real ground powder particles have different shapes and sizes. Though the magnetic susceptibility of silicon is very low [31], each powder particle would have a slightly different internal field due to its shape [33, 66]. By approximating the random powder particle as an ellipsoid of revolution, we calculated the resultant magnetic susceptibility broadening of the NMR linewidth [6, 12, 17, 60, 61, 77]. Convolving the magnetic susceptibility broadening with the dipolar linewidth accounted for the 290 Hz FWHM of our Si:Sb (2.75×10^{17} Sb/cm^3) powder sample.

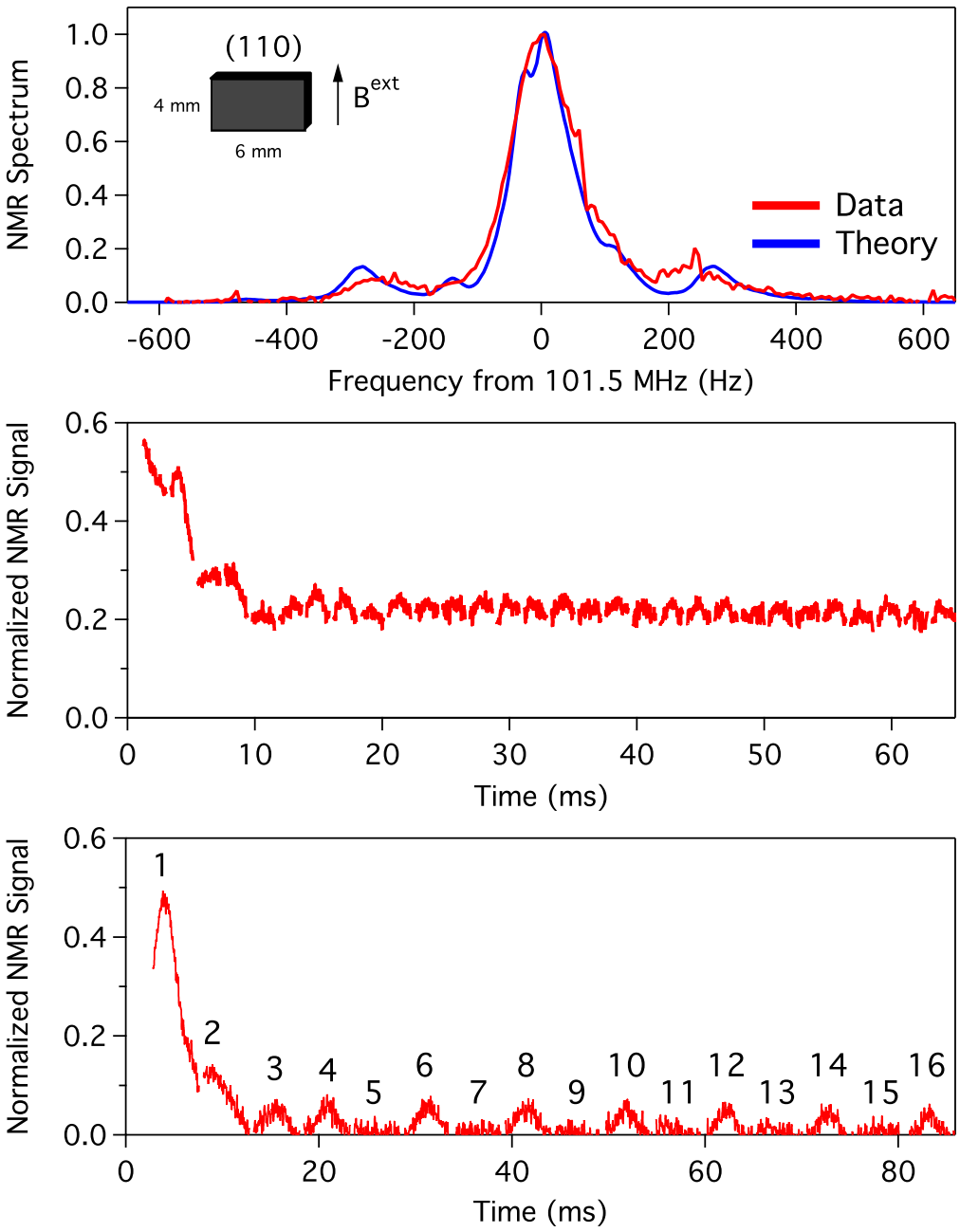

Figure 7.5: NMR data in a single crystal of Si:Sb (2.75×10^{17} Sb/cm^3) oriented with its (110) axis along $\hat{z}$ (see top inset). (Top) NMR spectrum (red) compared with a calculation for silicon that include dipolar coupling of $N = 6$ spins, magnetic susceptibility broadening, and skin depth due to the crystal shape (blue). FWHM=110 Hz. (Middle) CPMG echo train for $2\tau = 2.1$ ms shows the long tail. (Bottom) CPMG echo train for $2\tau = 5.2$ ms shows the even-odd effect.

In order to reduce the extrinsic broadening due to the magnetic susceptibility, we studied a single crystal of Si:Sb. Measurements in a single crystal allow confirmation of the lattice model and furthers the understanding of the magnetic susceptibility broadening. In a single crystal of Si:Sb (2.75×10^{17} Sb/cm^3) the orientation of the lattice allows only discrete coupling constants and subsequently, a unique dipolar lineshape. Additionally, the shape and orientation of the crystal with respect to $\vec{B}^{\rm ext}$ yields a smaller spread in the internal field due to the magnetic susceptibility [60]. Figure 7.4(inset, blue spectrum)] plots the convolution of the dipolar lineshape and the magnetic susceptibility broadening for the single crystal. The small satellites in the spectrum are due to the dipolar coupling between nearest-neighbors. This simulation is a good fit to the measured spectrum [Figure 7.4(inset, red spectrum)].

In the single crystal, the CPMG echo train still exhibits a long-lived coherence for short τ [Figure 7.4(middle)] and the even-odd effect for longer τ [Figure 7.4(bottom)]. These single crystal experiments were performed by Rona G. Ramos. I thank her for allowing me to present this data in my thesis.

7.5 Magic Angle Spinning

The technique of magic angle spinning [18, 55, 75, 79] (MAS) is used to reduce the dipolar coupling coefficient by rotating the entire sample about an axis tilted at 54.7° with respect to $\vec{B}^{\rm ext}$. In the time-average, the angular factor $(1-3\cos^2\theta_{jk})$ in the dipolar coupling constant [see equation (5.5)] vanishes. In addition to reducing the dipolar coupling, MAS eliminates Zeeman shift anisotropies and first order quadrupole splittings. These experiments seek to connect $\mathcal{H}_{zz}$ to the effects outlined in Chapter 3. Also, narrowing the NMR linewidth even further than in the single crystal leads to a better understanding of the population of ^{29}Si nuclei in the silicon lattice.

The FWHM of the MAS spectrum of Si:Sb (2.75×10^{17} Sb/cm^3) [Figure 7.5(top graph, red spectrum)] decreased by almost a factor of 6 compared with the spectrum of the static sample [Figure 7.5(top graph, black spectrum)]. Despite this narrowing, the MAS spectrum does not resolve distinct features in the NMR lineshape. The upper limit on the spread in Zeeman shifts is consistent with the single crystal data (Figure 7.4). Therefore, we conclude

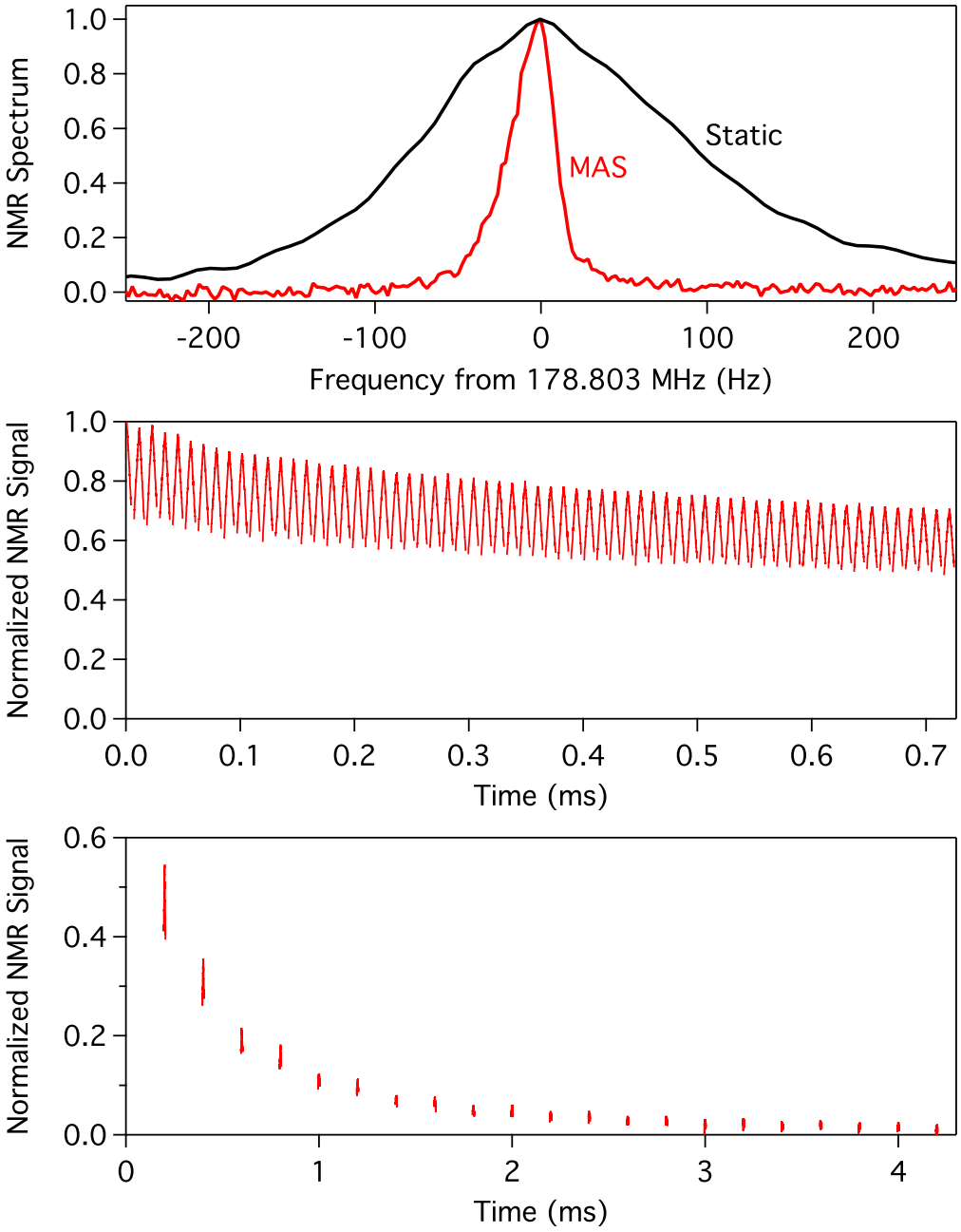

Figure 7.6: Magic Angle Spinning in Si:Sb (2.75×10^{17} Sb/cm^3). (Top) NMR spectrum of a static powdered sample with FWHM = 175Hz (black) and the MAS spectrum spun at 3 kHz with FWHM = 31 Hz (red). (Middle) CPMG echo train while spinning. $2\tau = 11.25$ ms. Long tail is expected since dipolar coupling is reduced. (Bottom) CPMG echo train while spinning. $2\tau = 0.2$ s. No pronounced even-odd effect, in contrast to Figure 4.2(bottom) and Figure 7.4(bottom).

that only $\mathcal{H}_{int} = \mathcal{H}_Z + \mathcal{H}_{zz}$ is needed to produce the static spectrum for this sample.

Figure 7.5 shows the CPMG echo train for two different time delays τ taken during MAS. The top graph shows that the echo train decays even more slowly than in the static sample. Also, for very large inter-pi-pulse spacings, as shown in the bottom graph, the even-odd effect is not present. The absence of the dipolar coupling and the dramatic changes in the observed CPMG echo trains suggest that $\mathcal{H}_{zz}$ plays an important role in our static NMR studies. These MAS experiments were performed by Yanqun Dong. I thank her for allowing me to present this data in my thesis.

We conclude these two experimental chapters by stating that these studies are by no means a complete study of all extrinsic effects in NMR. They are, however, representative of the high quality of the pulses that we use and the simple spin Hamiltonian of the nuclei under study. These experiments are near-optimal yet still exhibit the unexpected behavior of multiple π pulse echo trains. From these experimental results we can make concrete assumptions about the real pulse $\mathcal{P}$ and the real free evolution $\mathcal{V}$.

The experiments outlined in Chapters 5 and 6 provide the following constraints on any theoretical model that may explain our results: (1) the relevant internal Hamiltonian should contain only the Zeeman and dipolar Hamiltonians $\mathcal{H}_{int} = \mathcal{H}_Z + \mathcal{H}_{zz}$ and (2) the pulses are strong and address all spins equally, but they are not instantaneous.

Chapter 8

Exact Calculations with Finite Pulses

As we have shown in Chapter 4, instantaneous π pulses are not expected to affect the transverse relaxation time in dipolar solids. Application of multiple π pulses only serve to refocus the static spread of Zeeman shifts while the overall measurable coherence decays to zero under the action of the dipolar Hamiltonian as if no pulses were applied at all.

However, the experiments reported in Chapter 3 contradict these expectations in many surprising ways. For example, the measurable coherence appears to be sensitive to the phase of the applied π pulses. Some multiple π pulse echo trains extend well beyond the expected T_2 (CPMG, APCP) while others decay much faster (CP, APCPMG).

Additionally, the experimental explorations of Chapters 5 and 6 strongly suggest that extrinsic pulse imperfections are not responsible for these large discrepancies. Our observed effects are universal across many different samples all connected by the same form of the dipolar Hamiltonian. Thus, only the Zeeman and dipolar Hamiltonians are needed but the validity of the instantaneous π pulse approximation must be reconsidered.

In this chapter, we calculate the exact evolution of the density matrix by numerical means. The action of strong but finite pulses under the simultaneous influence of the dipolar Hamiltonian is the intrinsic effect that can lead to the large discrepancies we have observed.

8.1 Realistic Parameters

The first approach to calculate the expected results for finite pulses is the most straightforward: use everything we have gleaned from our experimental explorations about the pulses

and the spin system and apply the identical parameters in simulation. We begin this exact calculation by modifying the approach outlined in Chapter 4.

Since the delta-function pulse approximation has failed to explain our results, we return to the exact form of the pulse evolution operator from equation (5.8)

$$\mathcal{P}_\phi = \exp\left(-\frac{i}{\hbar}(\mathcal{H}_Z + \mathcal{H}_{zz} + \mathcal{H}_{P_\phi})t_p\right) \tag{8.1}$$

where $\mathcal{H}_Z$ is the Zeeman Hamiltonian, $\mathcal{H}_{zz}$ is the secular dipolar Hamiltonian, and $\mathcal{H}_{P_\phi} = -\hbar\omega_1 I_{\phi_T}$ is the Hamiltonian form of an rf pulse applied for time t_p along the ϕ-axis in the rotating frame.

To model the evolution of a spin system after n pulses, the relevant form of equation (4.3) becomes

$$\rho(t) = \{\mathcal{U}\mathcal{P}_\phi\mathcal{U}\}^n\rho(0)\{\mathcal{U}^{-1}\mathcal{P}_\phi^{-1}\mathcal{U}^{-1}\}^n \tag{8.2}$$

where the free evolution propagator is given by $\mathcal{U} = \exp(-\frac{i}{\hbar}(\mathcal{H}_Z + \mathcal{H}_{zz})\tau)$. From here, no approximations are made. Instead, numerical diagonalization is used during each $\mathcal{P}_\phi$ and $\mathcal{U}$ to evaluate $\rho(t)$ for the four pulse sequences that we consider [45, 16].

Figure 8.1 shows the exact calculations for all four pulse sequences CP, CPMG, APCP, and APCPMG using the same parameters as in the experiment. Unfortunately, the exact calculation fails to fit the data. These calculated curves deviate only slightly from the expectations for delta-function pulses.

Encouragingly, however, there are small differences between each calculated curve (Figure 8.2). This is a curious result since for the pulses used, H_1 divided by the FWHM of the spectrum was larger by a factor of 108, well beyond the conventional strong-pulse limit. Furthermore, the slight deviations between the calculated curves have the same qualitative comparisons with respect to each other as in the experiments. Namely, the CP simulated curve decays faster than the CPMG simulated curve, and the APCPMG simulated curve decays faster than the APCP simulated curve.

These slight differences between the calculated curves helped inspire us to perform additional calculations. In the next section, we inflated the dipolar coupling between spins in the hopes that the differences between the curves would be amplified. We were also inspired to take this route from NMR experiments on protons in liquid crystals because the proton

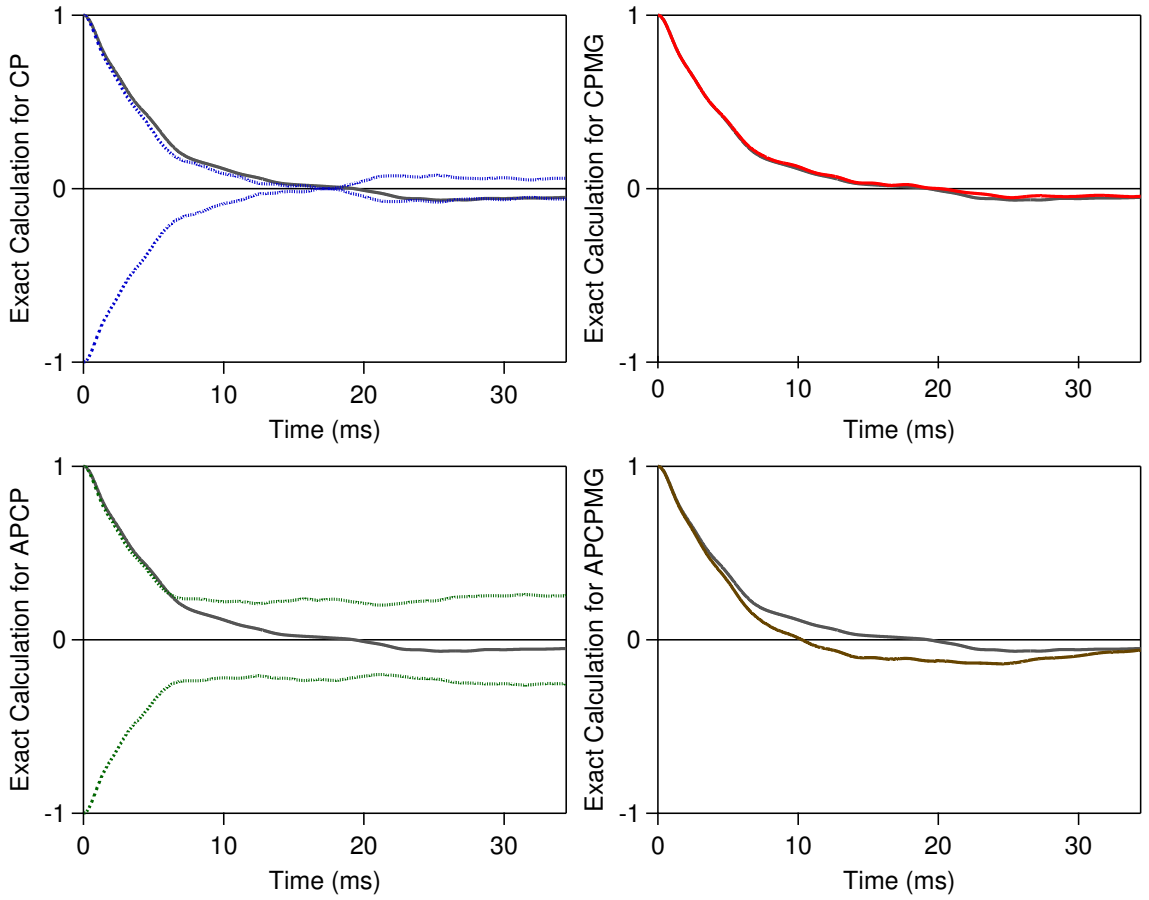

Figure 8.1: Exact calculations for the silicon experiments in pulse phase sensitivity for multiple π-pulse echo trains. The black reference curve is calculated assuming the dipolar coupling is set to zero during each pulse. In this limit, each pulse sequence produces the identical curve. Calculation parameters: $N = 7$ spins, $H_1 = 35.7$ kHz (14 μs π pulse), $2\tau = 72$ μs. These parameters are identical to the NMR data in Figure 4.4 except for the number of spins N. Figure 8.2 compares these calculations with the experiment.

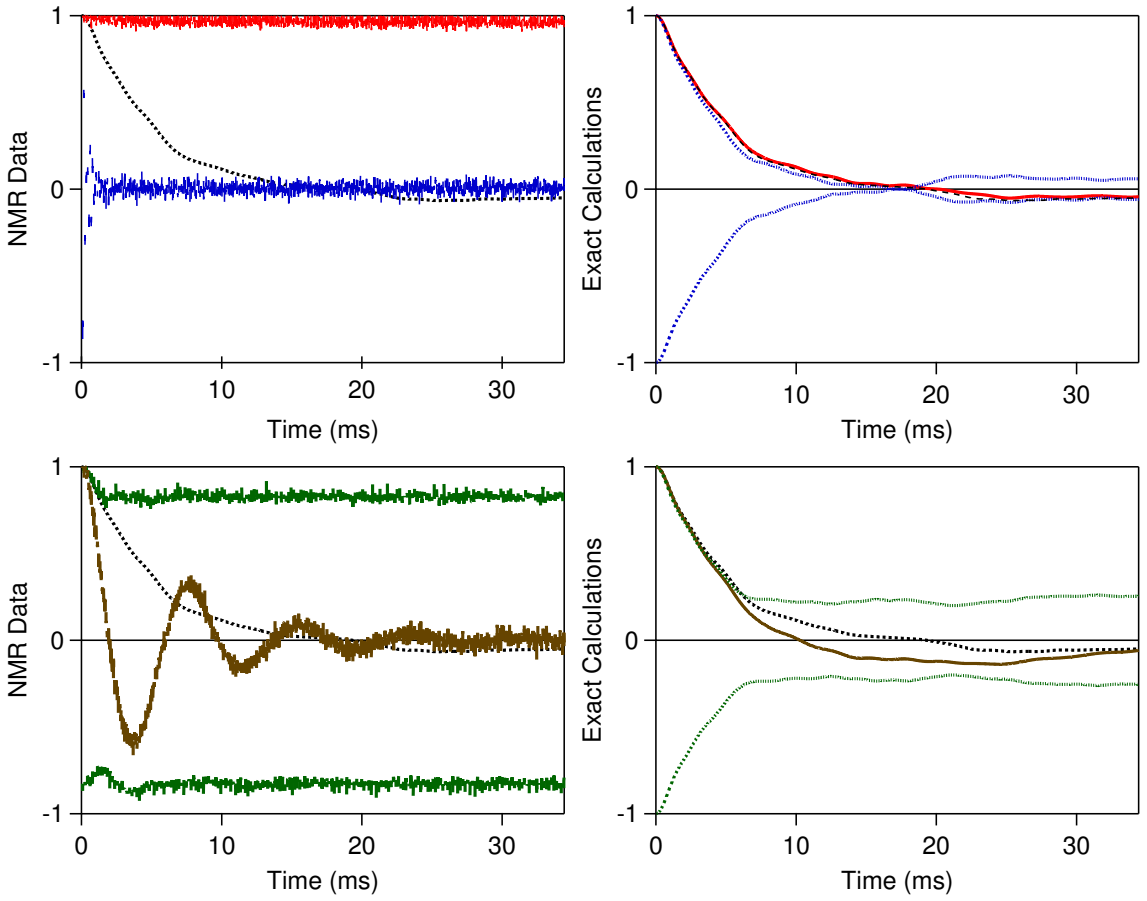

Figure 8.2: Comparison of exact calculations to actual NMR data using strong but finite π pulses in silicon. CPMG (red), CP (blue), APCP (green), and APCPMG (brown). Calculations use parameters: $N = 7$ spins, $H_1 = 35.7$ kHz (14 μs π pulse), $2\tau = 72$ μs, which are identical to the NMR data except for the number of spins N. The black dashed reference curve is calculated assuming that the dipolar coupling is turned off during the pulses. While there is a noticeable difference between each calculation curve when compared with the black dashed reference, the small sensitivity to pulse phase in the calculation does not quantitatively describe the data. It would appear that a further extrinsic parameter would need to be introduced to account for the remaining differences between each data curve. However, experimental tests of Chapters 6 and 7 suggest that no such extrinsic effects are needed. The calculation must be flawed in the only parameter that differs from experiment, N.

dipolar coupling is much stronger than ^{29}Si in silicon yet we observed the same qualitative results.

It may be helpful to point out that each of the four exact calculations in Figure 8.1 required 7 full days of computer time, which forced us to carefully consider the benefit of performing all four calculations. Initially, from the expectations derived in Chapter 5, it was thought that the strong pulses would produce very little deviation between any of the four sequences (after taking the absolute value). It turned out that the first calculation after 7 days yielded the top right graph in Figure 8.1, which differs very little from the underlying black curve for instantaneous pulses (dipolar coupling set to zero during pulses). However, I strongly suggested that we invest the time to calculate all four curves, in the least, to have evidence that the finiteness of pulses contributes nothing to the coherence. Although the deviation between the curves is small, it inspired us to reconsider the assumptions of strong pulses that eventually led to our understanding of the intrinsic origin of the observed long-lived coherence in CPMG. In this way, we greatly benefitted by not giving in to the temptations of bias for the sake of saving time.

8.2 Inflating the Dipolar Coupling

In this set of calculations, we strayed from the experimental parameters for the silicon data in the search for parameters in the exact calculation that would produce the deviations observed in Figure 8.1. The naturally weak dipolar coupling strength in silicon was not a necessary ingredient to observe the effects in experiment since we also found qualitatively similar effects in different nuclear systems including ^{13}C in C_{60}, ^{89}Y in Y_2O_3, as well as in ^{1}H in Adamantane [16, 67]. This allowed us to freely consider much strong coupling strengths then that of ^{29}Si in silicon.

Additionally, the expectations of Chapter 5 confirm that any delay between repeated π pulses will lead to decay. That is, no long-lived tail can develop for the CPMG pulse sequence as long as there are finite delays between the π pulses. Thus we were able to also reduce the inter-pulse delay times 2τ to enhance the effects of the strong but finite π pulses while remaining within the boundaries of experimentally realizable conditions.

Figure 8.3 plots the exact calculation of $\langle I_{y_1}(t)\rangle = \mathrm{Tr}\{\rho(t)I_{y_1}\}$ [equation (5.14)] aver-

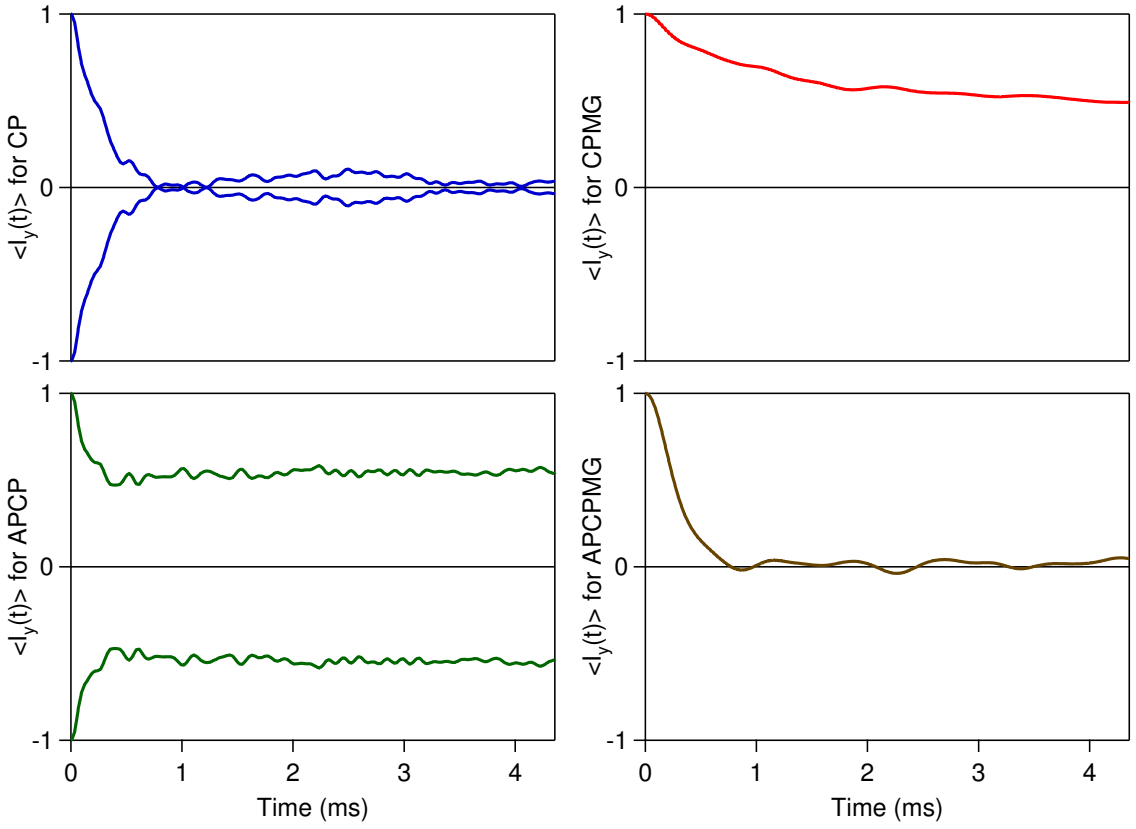

Figure 8.3: Exact calculations using strong but finite π pulses. Calculations use parameters: $N = 6$ spins, simulated pulse strength $H_1 = 40$ kHz ($t_p = 12.5\,\mu$s), delay between π pulses $2\tau = 2\,\mu$s, dipolar coupling scaled by $25 \times B_{jk}$ of ^{29}Si, Zeeman shift Ω_z/h drawn from a 3 kHz wide Gaussian for each DR, and the disorder average is taken over 150 DRs. The full lineshape is 4 kHz, which is a convolution of the pure dipolar line of 2.2 kHz and the Zeeman spread of 3 kHz. Compare these curves to the data of Fig. 4.4. CPMG and APCP display long-lived tails while CP and APCPMG decay to zero.

aged over 400 disorder realizations (DRs) for the four pulse sequences CP, CPMG, APCP, and APCPMG. These exact calculations have the same qualitative trends as the experiments. Namely, CPMG and APCP produce long-lived measurable coherence while CP and APCPMG decay away to zero. Since these exact calculations include no extrinsic imperfections, we conclude that the dipolar Hamiltonian and Zeeman Hamiltonian under the pulse must be the sole cause for the different time-evolved curves in Fig. 8.3.

However, there are two important caveats for these calculations. First, we used an $N = 6$ spin system to simulate the behavior of a macroscopic spin system. Because of computer

limitations, using a much larger system is not possible, inevitably leaving out many multi-spin entanglements. Second, we artificially inflated the dipolar coupling strength, which makes the differences in the curves more consistent with the experiments. We will return to these two important points in the last part of this section to show how system size and coupling strength are related.

Chapter 9

Average Hamiltonian Theory for Finite Pulses

To understand the mechanisms underlying the exact calculation, we turn to average Hamiltonian theory [27, 28, 52, 55, 79] to obtain approximate analytic results for the four pulse sequences under study. This analysis, in turn, allows the development of further calculations to uncover trends in the behavior of N spins under strong π pulses.

Average Hamiltonian or coherent averaging theory [27] was developed in NMR to approximate the behavior of multiple pulse experiments that use many $\pi/2$ pulses. Additionally, average Hamiltonian theory can be used to describe NMR experiments with very long pulses such as spin-locking or the magic-echo [69, 70].

Here, we wish to apply average Hamiltonian theory to a train of strong but finite π pulses where the delta-function pulse approximation (Chapter 5) predicts echoes that decay to zero. Because our pulses are so strong (Figure 6.4), we expected the nonzero pulse duration to give only a small perturbation to the delta-function pulse approximation. However, the exact calculations show a dramatic departure from this expectation (Figure 8.3).

9.1 Magnus Expansion in the Toggling Frame

The average Hamiltonian analysis starts from the total time-dependent Hamiltonian of an interacting spin system in the presence of an rf field

$$\mathcal{H}_{tot}(t) = \mathcal{H}_Z + \mathcal{H}_{zz} - \hbar\omega(t) I_{\phi_T} \tag{9.1}$$

where $\omega(t) = \omega_1$ during a pulse and zero during free evolution. $\mathcal{H}_Z$ and $\mathcal{H}_{zz}$ are the Zeeman Hamiltonian and the secular dipolar Hamiltonian respectively [equations (5.3) and (5.4)]. The spin operator along ϕ can be projected along the principle axes in the rotating frame $I_{\phi_T} = \cos\phi I_{x_T} + \sin\phi I_{y_T}$.

We label the first two terms of equation (9.1) as the internal Hamiltonian $\mathcal{H}_{int} = \mathcal{H}_{zz} + \mathcal{H}_Z$ in the language of average Hamiltonian theory [27, 55]. The applied pulse term then becomes the external or rf Hamiltonian $\mathcal{H}_{rf}(t) = -\hbar\omega(t)I_\phi$.

The total time-evolution operator

$$U_{tot}(t) = T\exp\Big[-\frac{i}{\hbar}\int_0^t dt'\mathcal{H}_0(t')\Big] \tag{9.2}$$

can then be split into a product of two parts

$$\begin{aligned} U_{tot}(t) &= U_{rf}(t)U_{int}(t) && (9.3)\\ U_{rf}(t) &= T\exp\Big[-\frac{i}{\hbar}\int_0^t dt'\mathcal{H}_{rf}(t')\Big] && (9.4)\\ U_{int}(t) &= T\exp\Big[-\frac{i}{\hbar}\int_0^t dt'\tilde{\mathcal{H}}(t')\Big] && (9.5)\\ \tilde{\mathcal{H}}(t) &= U_{rf}^{-1}(t)\mathcal{H}_{int}U_{rf}(t) && (9.6) \end{aligned}$$

where T is the Dyson time-ordering operator [79] and $\tilde{\mathcal{H}}(t)$ is the toggling frame Hamiltonian [27, 28, 55]. This separation is convenient when $\mathcal{H}_{rf}$ is periodic and cyclic with cycle time t_c. In this case, $U_{rf}(t_c) = 1$ and the Magnus expansion [50] gives

$$U_{int}(nt_c) = \exp\Big[-\frac{i}{\hbar}nt_c(\bar{\mathcal{H}}^{(0)} + \bar{\mathcal{H}}^{(1)} + \bar{\mathcal{H}}^{(2)} + ...)\Big] \tag{9.7}$$

for the time-evolution after any multiple, n, of the cycle time. The first two terms in the expansion are given by

$$\begin{aligned} \bar{\mathcal{H}}^{(0)} &= \frac{1}{t_c}\int_0^{t_c} dt\tilde{\mathcal{H}}(t) && (9.8)\\ \bar{\mathcal{H}}^{(1)} &= -\frac{i}{2t_c\hbar}\int_0^{t_c} dt_2\int_0^{t_2} dt_1[\tilde{\mathcal{H}}(t_2),\tilde{\mathcal{H}}(t_1)]. && (9.9) \end{aligned}$$

The advantage of the Magnus expansion is that the full time-evolution operator $U_{tot}(t)$ is now written as a single exponential instead of a product of exponentials. Additionally, the

terms in the average Hamiltonian expansion $\bar{\mathcal{H}}^{(0)}$, $\bar{\mathcal{H}}^{(1)}$, $\bar{\mathcal{H}}^{(2)}\ldots$ are time independent and exactly describe the system at multiples of the cycle time t_c. In practice, this exact expression is replaced by an approximate one when the series expansion is truncated after the first few terms [27, 28, 52, 55, 79].

The four pulse sequences studied here all have the same cycle time $t_c = 4\tau + 2t_p$ consisting of two π pulses with a time delay of τ before and after each pulse. The average Hamiltonian description is simplest when the cycle time is short and the pulses are strong compared with the Zeeman spread, $\omega_1 \gg \Omega_z$, since the expansion in equation (9.7) is then dominated by the first few terms.

Using these steps we can calculate the leading terms for the four pulse sequences under study. For example, the time-evolution of $\rho(t)$ under the CPMG sequence is

$$\begin{aligned} \rho(t) &= U_{tot}(t)\rho(0)U_{tot}^{-1}(t) \\ &= \{\mathcal{U}_5\mathcal{P}_4\mathcal{U}_3\mathcal{P}_2\mathcal{U}_1\}^n\rho(0)\{inv\}^n \end{aligned} \tag{9.10}$$

where $\mathcal{P}_2 = \mathcal{P}_4$ are π pulses along $\hat{y}$ and include the Zeeman and dipolar Hamiltonians. $\mathcal{U}_i$, $i = 1, 3, 5$ are the free evolution propagators that only include the Zeeman and dipolar Hamiltonian.

After identifying the parts of U_{tot}, the next step is to calculate the toggling frame Hamiltonians for each of these events. As an example, $\tilde{\mathcal{H}}(t_3)$ in CPMG for event $\mathcal{U}_3$ is

$$\begin{aligned} \tilde{\mathcal{H}}(t_3) &= \{U_{rf}^{-1}(t_1)U_{rf}^{-1}(t_2)U_{rf}^{-1}(t_3)\}\mathcal{H}_{int}\{inv\} \\ &= \mathcal{R}_y^{-1}(\Omega_z I_{z_T} + \mathcal{H}_{zz})\mathcal{R}_y \\ &= -\Omega_z I_{z_T} + \mathcal{H}_{zz} \end{aligned} \tag{9.11}$$

where the unitary operators U_{rf} are applied in reverse time-ordering [equation (9.6)].

Table 9.1 gives the expressions for all the toggling frame Hamiltonians as modified by $\mathcal{H}_{rf}$ in each event of the CPMG sequence. Note that the difference between the toggling frame transformation of the $\mathcal{U}_3$ interval and the $\mathcal{U}_1$ and $\mathcal{U}_5$ intervals is only the sign in front of the Zeeman term $\Omega_z I_{z_T}$. This detail is important because it is an explicit indication that the pulses are free from any extrinsic errors. Thus, I_z rotates to $-I_z$ after each π pulse. This rotation flips the sign of the single-spin Zeeman Hamiltonian, but does nothing to the bilinear dipole Hamiltonian.

Event	Time	$\tilde{\mathcal{H}}(t_i)$ for CPMG
$\mathcal{U}_1$	τ	$+\Omega_z I_{z_T} + \mathcal{H}_{zz}$
$\mathcal{P}_2$	t_p	$+\Omega_z(I_{z_T}C_\theta + I_{x_T}S_\theta) - \frac{1}{2}\mathcal{H}_{yy} + \mathcal{H}_y^S C_{2\theta} + \mathcal{H}_y^A S_{2\theta}$
$\mathcal{U}_3$	2τ	$-\Omega_z I_{z_T} + \mathcal{H}_{zz}$
$\mathcal{P}_4$	t_p	$-\Omega_z(I_{z_T}C_\theta + I_{x_T}S_\theta) - \frac{1}{2}\mathcal{H}_{yy} + \mathcal{H}_y^S C_{2\theta} + \mathcal{H}_y^A S_{2\theta}$
$\mathcal{U}_5$	τ	$+\Omega_z I_{z_T} + \mathcal{H}_{zz}$

Table 9.1: Toggling frame Hamiltonians $\tilde{\mathcal{H}}(t_i)$ during each event of the CPMG cycle $\{\tau - 180_Y - 2\tau - 180_Y - \tau\}$ where t_p is the pulse time, and τ is the free evolution time. $C_\theta = \cos(\omega_1 t)$, $C_{2\theta} = \cos(2\omega_1 t)$, $S_\theta = \sin(\omega_1 t)$, $S_{2\theta} = \sin(2\omega_1 t)$.

Event	Time	$\tilde{\mathcal{H}}(t_i)$ for CP
$\mathcal{U}_1$	τ	$+\Omega_z I_{z_T} + \mathcal{H}_{zz}$
$\mathcal{P}_2$	t_p	$+\Omega_z(I_{z_T}C_\theta - I_{y_T}S_\theta) - \frac{1}{2}\mathcal{H}_{xx} + \mathcal{H}_x^S C_{2\theta} - \mathcal{H}_x^A S_{2\theta}$
$\mathcal{U}_3$	2τ	$-\Omega_z I_{z_T} + \mathcal{H}_{zz}$
$\mathcal{P}_4$	t_p	$-\Omega_z(I_{z_T}C_\theta - I_{y_T}S_\theta) - \frac{1}{2}\mathcal{H}_{xx} + \mathcal{H}_x^S C_{2\theta} - \mathcal{H}_x^A S_{2\theta}$
$\mathcal{U}_5$	τ	$+\Omega_z I_{z_T} + \mathcal{H}_{zz}$

Table 9.2: Toggling frame Hamiltonians $\tilde{\mathcal{H}}(t_i)$ during each event of the APCP cycle $\{\tau - 180_X - 2\tau - 180_X - \tau\}$.

Event	Time	$\tilde{\mathcal{H}}(t_i)$ for APCP
$\mathcal{U}_1$	τ	$+\Omega_z I_{z_T} + \mathcal{H}_{zz}$
$\mathcal{P}_2$	t_p	$+\Omega_z(I_{z_T}C_\theta + I_{y_T}S_\theta) - \frac{1}{2}\mathcal{H}_{xx} + \mathcal{H}_x^S C_{2\theta} + \mathcal{H}_x^A S_{2\theta}$
$\mathcal{U}_3$	2τ	$-\Omega_z I_{z_T} + \mathcal{H}_{zz}$
$\mathcal{P}_4$	t_p	$-\Omega_z(I_{z_T}C_\theta - I_{y_T}S_\theta) - \frac{1}{2}\mathcal{H}_{xx} + \mathcal{H}_x^S C_{2\theta} - \mathcal{H}_x^A S_{2\theta}$
$\mathcal{U}_5$	τ	$+\Omega_z I_{z_T} + \mathcal{H}_{zz}$

Table 9.3: Toggling frame Hamiltonians $\tilde{\mathcal{H}}(t_i)$ during each event of the APCP cycle $\{\tau - 180_{\bar{X}} - 2\tau - 180_X - \tau\}$.

Event	Time	$\tilde{\mathcal{H}}(t_i)$ for APCPMG
$\mathcal{U}_1$	τ	$+\Omega_z I_{z_T} - \mathcal{H}_{zz}$
$\mathcal{P}_2$	t_p	$+\Omega_z(I_{z_T}C_\theta - I_{x_T}S_\theta) - \frac{1}{2}\mathcal{H}_{yy} + \mathcal{H}_y^S C_{2\theta} + \mathcal{H}_y^A S_{2\theta}$
$\mathcal{U}_3$	2τ	$-\Omega_z I_{z_T} + \mathcal{H}_{zz}$
$\mathcal{P}_4$	t_p	$-\Omega_z(I_{z_T}C_\theta + I_{x_T}S_\theta) - \frac{1}{2}\mathcal{H}_{yy} + \mathcal{H}_y^S C_{2\theta} + \mathcal{H}_y^A S_{2\theta}$
$\mathcal{U}_5$	τ	$+\Omega_z I_{z_T} + \mathcal{H}_{zz}$

Table 9.4: Toggling frame Hamiltonians $\tilde{\mathcal{H}}(t_i)$ during each event of the APCPMG cycle $\{\tau - 180_{\bar{Y}} - 2\tau - 180_Y - \tau\}$.

For comparison, the toggling Hamiltonians for the CP sequence are provided in Table 9.2, the APCP sequence in Table 9.3, and the APCPMG sequence in Table 9.4. The difference between the alternating phase sequences and their counterparts can be obtained with a proper sign change in specific terms during the first pulse. The toggling frame Hamiltonians for APCPMG differs from CPMG by the signs of S_θ and $S_{2\theta}$ in event $\mathcal{P}_2$. Similarly, CP differs from APCP also by the signs of S_θ and $S_{2\theta}$ in event $\mathcal{P}_2$.

The time-dependent terms of the toggling frame Hamiltonians during the pulses are of key interest in this analysis. The cosine and sine terms depend directly on the strength of the rf field ω_1. It is tempting to assume the limit $\omega_1 \to \infty$ and $t_p \to 0$, which would make these time-dependent terms under the pulses negligible. After all, most experiments in this study are conducted using very strong pulses. However, by keeping these small terms, we find that they have a large impact over many pulses.

The toggling frame Hamiltonians from Table 9.1 are fed into Eq. (9.8) to yield the leading order behavior for the CPMG sequence [45]. This approach is repeated for all four pulse sequences giving the zeroth-order average Hamiltonians

$$\bar{\mathcal{H}}^{(0)}_{\mathrm{CP}} = \frac{1}{t_c}(4\tau\mathcal{H}_{zz} - t_p\mathcal{H}_{xx}) \tag{9.12}$$

$$\bar{\mathcal{H}}^{(0)}_{\mathrm{CPMG}} = \frac{1}{t_c}(4\tau\mathcal{H}_{zz} - t_p\mathcal{H}_{yy}) \tag{9.13}$$

$$\bar{\mathcal{H}}^{(0)}_{\mathrm{APCP}} = \frac{1}{t_c}(4\tau\mathcal{H}_{zz} - t_p\mathcal{H}_{xx} + \frac{4\Omega_z t_p}{\pi} I_{y_T}) \tag{9.14}$$

$$\bar{\mathcal{H}}^{(0)}_{\mathrm{APCPMG}} = \frac{1}{t_c}(4\tau\mathcal{H}_{zz} - t_p\mathcal{H}_{yy} - \frac{4\Omega_z}{\pi} t_p I_{x_T}) \tag{9.15}$$

with the following first order corrections

$$\begin{aligned}
\bar{\mathcal{H}}^{(1)}_{\mathrm{CP}} &= \frac{+i}{2t_c\hbar}\frac{t_p}{\pi}\Big(t_p[\mathcal{H}^A_x, \mathcal{H}^S_x + \mathcal{H}_{xx}] \\
&\quad +(8\tau+2t_p)[\Omega_z I_{y_T}, \Omega_z I_{z_T} + \mathcal{H}_{xx}]\Big) && (9.16)\\
\bar{\mathcal{H}}^{(1)}_{\mathrm{CPMG}} &= \frac{-i}{2t_c\hbar}\frac{t_p}{\pi}\Big(t_p[\mathcal{H}^A_y, \mathcal{H}^S_y + \mathcal{H}_{yy}] \\
&\quad +(8\tau+2t_p)[\Omega_z I_{x_T}, \Omega_z I_{z_T} + \mathcal{H}_{yy}]\Big) && (9.17)\\
\bar{\mathcal{H}}^{(1)}_{\mathrm{APCP}} &= 0 && (9.18)\\
\bar{\mathcal{H}}^{(1)}_{\mathrm{APCPMG}} &= 0 && (9.19)
\end{aligned}$$

where we define

$$\begin{aligned}
\mathcal{H}_{xx} &= \sum_{j=1}^{N}\sum_{k>j}^{N} B_{jk}(3I_{x_j}I_{x_k} - \vec{I_j}\cdot\vec{I_k}) && (9.20)\\
\mathcal{H}_{yy} &= \sum_{j=1}^{N}\sum_{k>j}^{N} B_{jk}(3I_{y_j}I_{y_k} - \vec{I_j}\cdot\vec{I_k}) && (9.21)\\
\mathcal{H}^A_x &= \frac{3}{2}\sum_{j=1}^{N}\sum_{k>j}^{N} B_{jk}(I_{y_j}I_{z_k} + I_{z_j}I_{y_k}) && (9.22)\\
\mathcal{H}^A_y &= \frac{3}{2}\sum_{j=1}^{N}\sum_{k>j}^{N} B_{jk}(I_{x_j}I_{z_k} + I_{z_j}I_{x_k}) && (9.23)\\
\mathcal{H}^S_x &= \frac{3}{2}\sum_{j=1}^{N}\sum_{k>j}^{N} B_{jk}(I_{z_j}I_{z_k} - I_{y_j}I_{y_k}) && (9.24)\\
\mathcal{H}^S_y &= \frac{3}{2}\sum_{j=1}^{N}\sum_{k>j}^{N} B_{jk}(I_{z_j}I_{z_k} - I_{x_j}I_{x_k}). && (9.25)
\end{aligned}$$

Inspection of these expressions leads to several important conclusions. First, the average Hamiltonian expressions for all four pulse sequences reduce to the bare dipolar Hamiltonian $\mathcal{H}_{zz}$ in the limit when $t_p \to 0$. The first order correction terms $\bar{\mathcal{H}}^{(1)}$ vanish in that limit since they are all proportional to t_p. While the instantaneous pulse approximation leads to an identical decay for all four pulse sequences, real pulses introduce dynamics unique to each sequence.

Second, all the first-order correction terms $\bar{\mathcal{H}}^{(1)}$ are strictly due to the commonly ne-

glected time-dependent terms under the pulse. Though the prefactor is small, these first-order terms provide important contributions to the time-evolution of quantum coherences.

Third, by symmetry, the alternating phase sequences APCP and APCPMG have no odd-order Average Hamiltonian terms. Some sequences were designed to exploit such symmetries in an effort to eliminate the first few Average Hamiltonian terms and thus reduce decay. However, in experiments and in simulations, we observe a long-lived coherence in the APCP sequence but a fast decay in the APCPMG sequence.

Fourth, the Average Hamiltonian expressions for the CP sequence are isomorphic to the CPMG sequence under the transformation $(x, y) \mapsto (y, -x)$. The same transformation applies to mapping the APCP sequence to the APCPMG sequence. Also, for $\Omega_z = 0$, $\bar{\mathcal{H}}^{(0)}_{\mathrm{CP}} \equiv \bar{\mathcal{H}}^{(0)}_{\mathrm{APCP}}$ and $\bar{\mathcal{H}}^{(0)}_{\mathrm{CPMG}} \equiv \bar{\mathcal{H}}^{(0)}_{\mathrm{APCPMG}}$ leaving only a difference in the first order correction terms. Despite these similarities, all four pulse sequences produce very different results in experiments (Figure 4.4) and in simulations (Figure 8.3).

Fifth and finally, the alternating phase sequences APCP and APCPMG have another distinct difference from CP and CPMG at the level of $\mathcal{H}^{(0)}$. In equations (9.14) and (9.15) a single spin operator appears that is proportional to both the Zeeman shift Ω_z and the pulse duration t_p.

9.2 Second Averaging

Though the average Hamiltonian expressions [Eqs. (9.12)-(9.19)] are all different, it is not obvious how they produce the very distinct expectation values $\langle I_y(t) \rangle$ in Figure 8.3. In order to gain insight into the mechanisms that produce these results, we rewrite the average Hamiltonian expressions using second averaging [26, 55, 63].

Equations (9.14) and (9.15) each contain a single spin operator term (e.g. $\frac{4\Omega_z t_p}{\pi} I_{y_T}$ in $\bar{\mathcal{H}}^{(0)}_{\mathrm{APCP}}$) that looks like a transverse field coupled to the spins. Since $\bar{\mathcal{H}}^{(0)}$ is time-independent, we treat this effective transverse field as a continuous field $\bar{\mathcal{H}}_{rf}$ even though it only originates from the pulses. Applying average Hamiltonian theory in this second toggling frame

yields

$$\bar{\bar{\mathcal{H}}}^{(0)}_{\mathrm{APCP}} = -\frac{1}{t_c}(2\tau - \frac{t_p}{2})\mathcal{H}_{yy} \tag{9.26}$$

$$\bar{\bar{\mathcal{H}}}^{(0)}_{\mathrm{APCPMG}} = -\frac{1}{t_c}(2\tau - \frac{t_p}{2})\mathcal{H}_{xx}. \tag{9.27}$$

These leading order second-averaged Hamiltonians differ only in the direction of a single anisotropic dipolar Hamiltonian term. The direction for both $\mathcal{H}_{xx}$ and $\mathcal{H}_{yy}$ were dictated by the effective transverse field $\bar{\mathcal{H}}_{rf}$. The effect that these anisotropic dipolar Hamiltonians have on the measurable coherence depends on the initial density matrix. For this paper, we set $\rho(0) = I_{y_T}$. From the commutation relations, we note that $\bar{\bar{\mathcal{H}}}^{(0)}_{\mathrm{APCP}}$ preserves I_{y_T}, since $[I_{y_T}, \mathcal{H}_{yy}] = 0$, while $\bar{\bar{\mathcal{H}}}^{(0)}_{\mathrm{APCPMG}}$ does not, since $[I_{y_T}, \mathcal{H}_{xx}] \neq 0$. Therefore, this second-averaging analysis predicts that APCP will have long-lived coherence while APCPMG should rapidly decay towards zero.

However, only considering Eqs. (9.26) and (9.27) would be a mistake since higher order corrections in this second averaged Magnus expansion are non-negligible. Strictly truncating the second averaged Hamiltonian to Eqs. (9.26) and (9.27) is only a good approximation when $\Omega_z t_p \gg B_{jk} t_c$. In contrast, our experiments are typically in the regime where $\Omega_z t_p$ is comparable to $B_{jk} t_c$. Still, our experimental results show long-lived coherence in APCP, suggesting that the higher-order corrections do not induce decay.

Because a similar difference exists between the CP and CPMG pulse sequences, we wish to apply the idea of second averaging to their average Hamiltonian expressions as well. However, because equations (9.12) and (9.13) do not have similar effective transverse fields, we must look to their first order correction terms.

For CPMG, the first order term $\bar{\mathcal{H}}^{(1)}_{\mathrm{CPMG}}$ [Eq. (9.17)] contains a single spin operator proportional to $\Omega_z^2 I_{y_T}$ from the commutator $[I_{x_T}, I_{z_T}]$. Similarly, $\bar{\mathcal{H}}^{(1)}_{\mathrm{CP}}$ [Eq. (9.16)] contains a term proportional to $\Omega_z^2 I_{x_T}$. These single spin terms are analogous to the effective transverse fields that produced $\bar{\bar{\mathcal{H}}}^{(0)}_{\mathrm{APCP}}$ and $\bar{\bar{\mathcal{H}}}^{(0)}_{\mathrm{APCPMG}}$. Thus, this analysis predicts long-lived coherence in CPMG and a fast decay in CP, at least for large Ω_z (Figure 8.3).

However, in experiments, we observed a long tail in CPMG even for very small Ω_z. This experimental result inspired us to re-examine $\bar{\mathcal{H}}^{(1)}_{\mathrm{CPMG}}$ for another single spin operator.

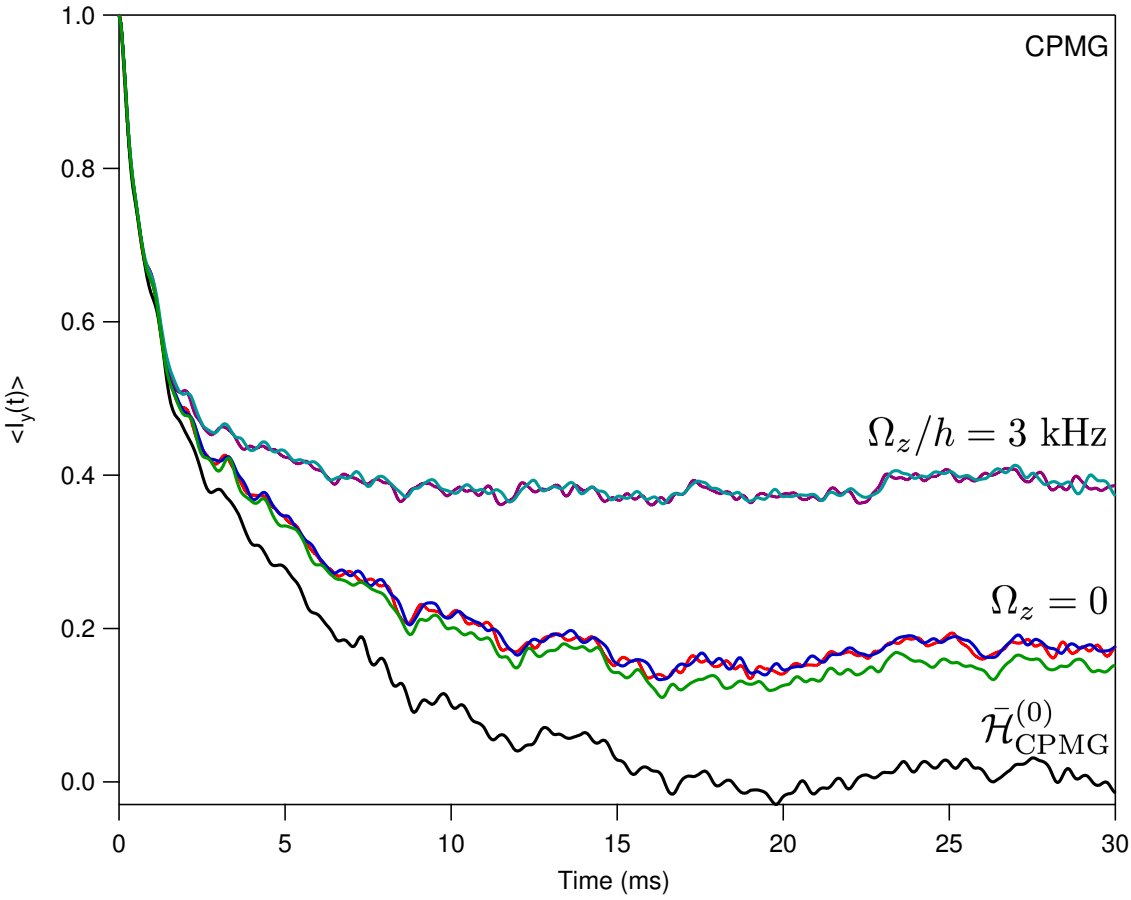

Figure 9.1: Calculations for the CPMG pulse sequence with $N = 4$, $2\tau = 2$ μs, $t_p = 12.5$ μs, $25 \times B_{jk}$ of ^{29}Si in silicon, and an average over 400 DRs. Exact calculations with Ω_z/h drawn from a 3 kHz wide Gaussian for each DR (purple curve) and $\Omega_z = 0$ (red curve). Average Hamiltonian calculations $\bar{\mathcal{H}}^{(0)}_{\mathrm{CPMG}} + \bar{\mathcal{H}}^{(1)}_{\mathrm{CPMG}}$ with Ω_z/h drawn from a 3 kHz wide Gaussian for each DR (teal curve) and $\Omega_z = 0$ (blue curve). Approximate calculation with $\bar{\mathcal{H}}^{(0)}_{\mathrm{CPMG}} + \bar{\mathcal{F}}^{(1)}_{\mathrm{CPMG}}$ for $\Omega_z = 0$ (green curve). Zeroth order average Hamiltonian $\bar{\mathcal{H}}^{(0)}_{\mathrm{CPMG}}$ (black curve).

Evaluating equation (9.17) for $\Omega_z = 0$ gives

$$\bar{\mathcal{H}}^{(1)}_{\mathrm{CPMG}}|_{\Omega_z=0} = \frac{-i}{2t_c\hbar}\frac{t_p^2}{\pi}[\mathcal{H}_y^A, \mathcal{H}_y^S + \mathcal{H}_{yy}]. \tag{9.28}$$

There are many multi-spin operators in this expression but the only single-spin operator left in equation (9.28) is

$$\bar{\mathcal{F}}^{(1)}_{\mathrm{CPMG}} \equiv -\frac{9t_p^2}{16\pi t_c\hbar}\sum_{j=1}^{N}\sum_{k>j}^{N} B_{jk}^2(I_{y_j} + I_{y_k}). \tag{9.29}$$

Although this term is indeed a single spin operator, it is not proportional to the total spin operator I_{y_T}. Nevertheless, the effect of $\bar{\mathcal{F}}^{(1)}_{\mathrm{CPMG}}$ on $\bar{\mathcal{H}}^{(0)}_{\mathrm{CPMG}}$ can be examined by calculating the time-evolution of $\langle I_{y_1}(t)\rangle$ using only $\bar{\mathcal{H}}^{(0)}_{\mathrm{CPMG}} + \bar{\mathcal{F}}^{(1)}_{\mathrm{CPMG}}$ [Figure 9.2(green curve)].

For comparison, Figure 9.2 plots exact calculations and average Hamiltonian calculations for the CPMG sequence. Without any additions, $\bar{\mathcal{H}}^{(0)}_{\mathrm{CPMG}}$ [Figure 9.2(black curve)] decays to zero. Using the average Hamiltonian $\bar{\mathcal{H}}^{(0)}_{\mathrm{CPMG}} + \bar{\mathcal{H}}^{(1)}_{\mathrm{CPMG}}$ to time-evolve the expectation value $\langle I_y(t)\rangle$ yields a long-tail in good agreement with the exact calculation for the case where Ω_z/h is drawn from a 3 kHz wide Gaussian for each DR [Figure 9.2(teal curve compared to purple curve)].

Even for the case of $\Omega_z = 0$ the average Hamiltonian $\bar{\mathcal{H}}^{(0)}_{\mathrm{CPMG}} + \bar{\mathcal{H}}^{(1)}_{\mathrm{CPMG}}$ [Figure 9.2(blue)] is still in good agreement with the exact calculation [Figure 9.2(red)]. These curves show that the long-tail in CPMG can exist in the absence of the $\Omega_z^2 I_{y_T}$ term. Surprisingly, we also find that $\bar{\mathcal{H}}^{(0)}_{\mathrm{CPMG}} + \bar{\mathcal{F}}^{(1)}_{\mathrm{CPMG}}$ [Figure 9.2(green curve)] fits together with these two curves despite the terms that were neglected. However, these neglected terms also contribute to a tail in calculations of $\bar{\mathcal{H}}^{(0)}_{\mathrm{CPMG}} + \bar{\mathcal{H}}^{(1)}_{\mathrm{CPMG}} - \bar{\mathcal{F}}^{(1)}_{\mathrm{CPMG}}$. Furthermore, multi-spin terms play an even bigger role in systems with stronger coupling or a larger number of spins.

The emphasis of this section was to highlight the influence of a few important terms in the average Hamiltonian [equations (9.12)-(9.19)]. Focussing on only a few terms allows us to understand the qualitative results in calculations of $\langle I_{y_1}(t)\rangle$. The exact calculation contains more physics. As we shall show in Chapter 9, the qualitative similarities pointed out in the second-averaging of APCP and CPMG, for example, do not give a complete picture of the evolution of $\rho(t)$.

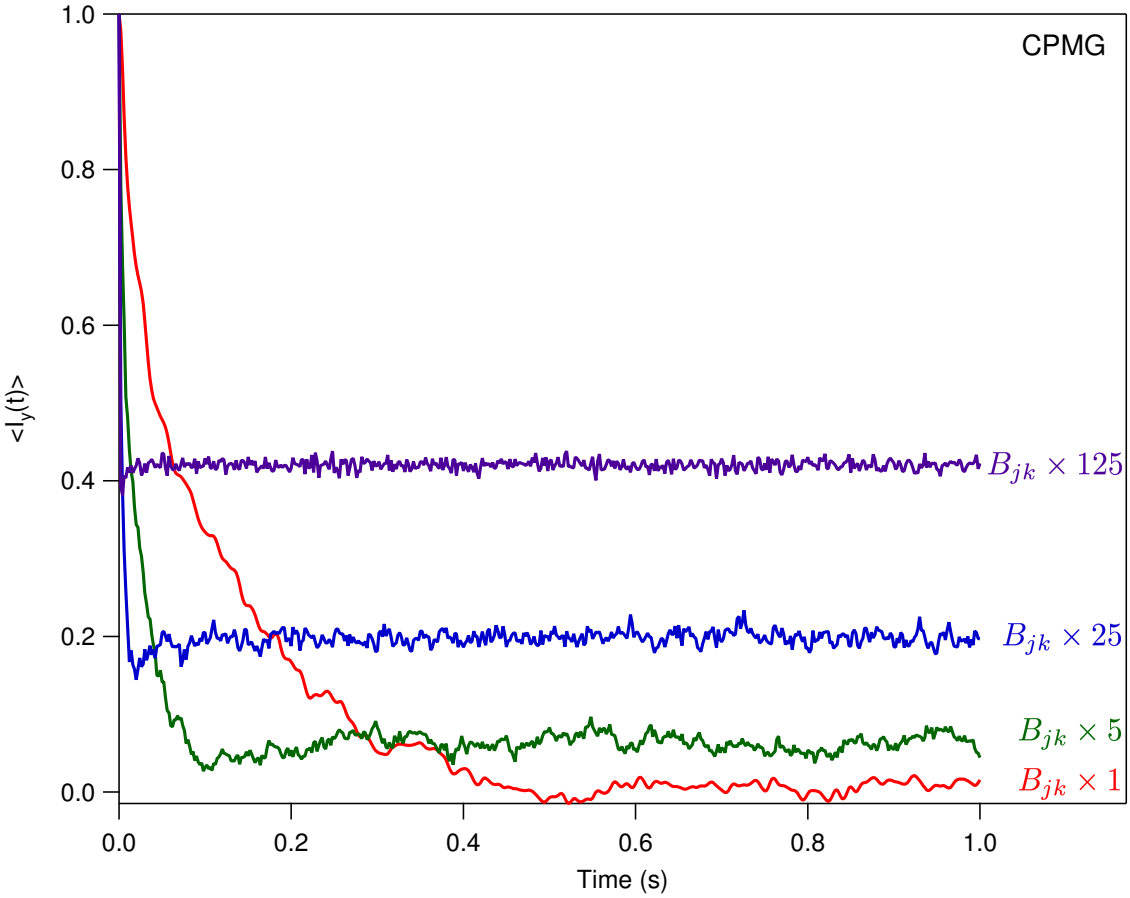

Figure 9.2: Calculations of the time evolution of $\langle I_y(t) \rangle$ under $\bar{\mathcal{H}}^{(0)}_{\mathrm{CPMG}} + \bar{\mathcal{H}}^{(1)}_{\mathrm{CPMG}}$ [Eqs. (9.13) and (9.17)] with different coupling strengths as multiples of B_{jk} for ^{29}Si in Silicon ($B_{jk} \times 1$ produces a dipolar linewidth of 90 Hz). Parameters: $N = 4$ spins, $\Omega_Z = 0$, $H_1 = 40$ kHz, $2\tau = 2$ μs, 1000 DR average. Exact calculations produce similar curves for these parameters.

9.3 Reconciling Simulations with Experiments

We now address the two important caveats that we made for the exact calculations of Figure 8.3. Namely, we included only a small number of spins in our exact calculation and inflated the dipolar coupling strength slightly above the experimental values in order to accentuate the contributions of the time-dependent terms under the pulses. For simplicity, this discussion considers only the CPMG pulse sequence with $\Omega_z = 0$.

Figure 9.3 shows a set of calculations of $\langle I_y(t) \rangle$ evolved under $\bar{\mathcal{H}}^{(0)}_{\mathrm{CPMG}} + \bar{\mathcal{H}}^{(1)}_{\mathrm{CPMG}}$ for different dipolar coupling strengths. For weak dipolar coupling strengths ($B_{jk} \times 1$ of ^{29}Si in

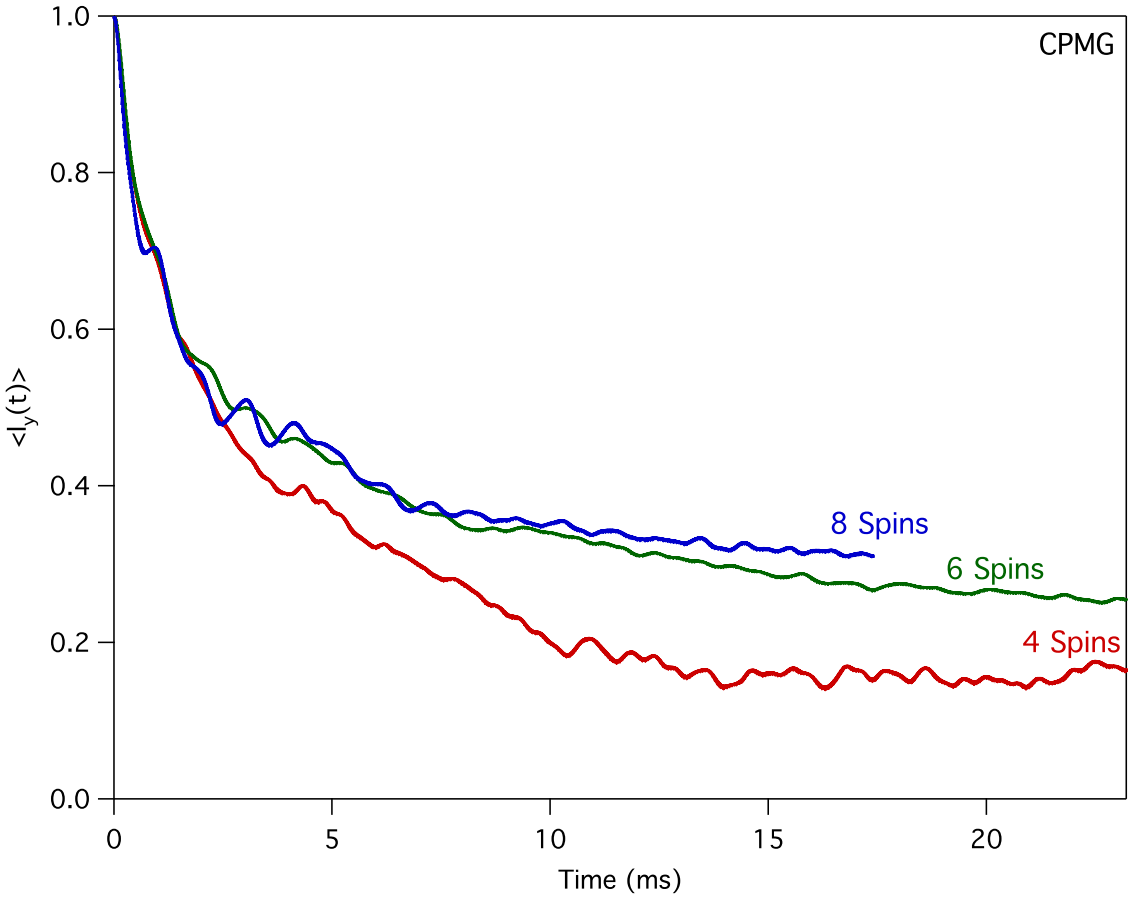

Figure 9.3: Exact calculations of the CPMG pulse sequence show that the tail height of the measurable coherence increases with system size (even N are compared to avoid artifacts [95]). Parameters: $\Omega_Z = 0$, $H_1 = 40$ kHz, $2\tau = 2$ μs, 400 DR average (100 DR average for N=8).

Silicon), the measured coherence decays to zero in agreement with the delta-function pulse approximation (see Chapter 5). As B_{jk} increases, the initial decay rate increases, consistent with the dipolar linewidth [1, 47, 79, 89, 11]. For large B_{jk}, this initial decay is followed by a long tail that increases with dipolar coupling strength.

Figure 9.3 shows a different set of calculations where the CPMG tail height increases with system size. In this case, the coupling strength is fixed at 25 times that of ^{29}Si, while each exact calculation considers a different number of spins N. By keeping B_{jk} fixed, the initial decay is very similar for the three system sizes shown. However, after some time, the effect of many strong but finite π pulses appears to produce a long-lived tail in the measured

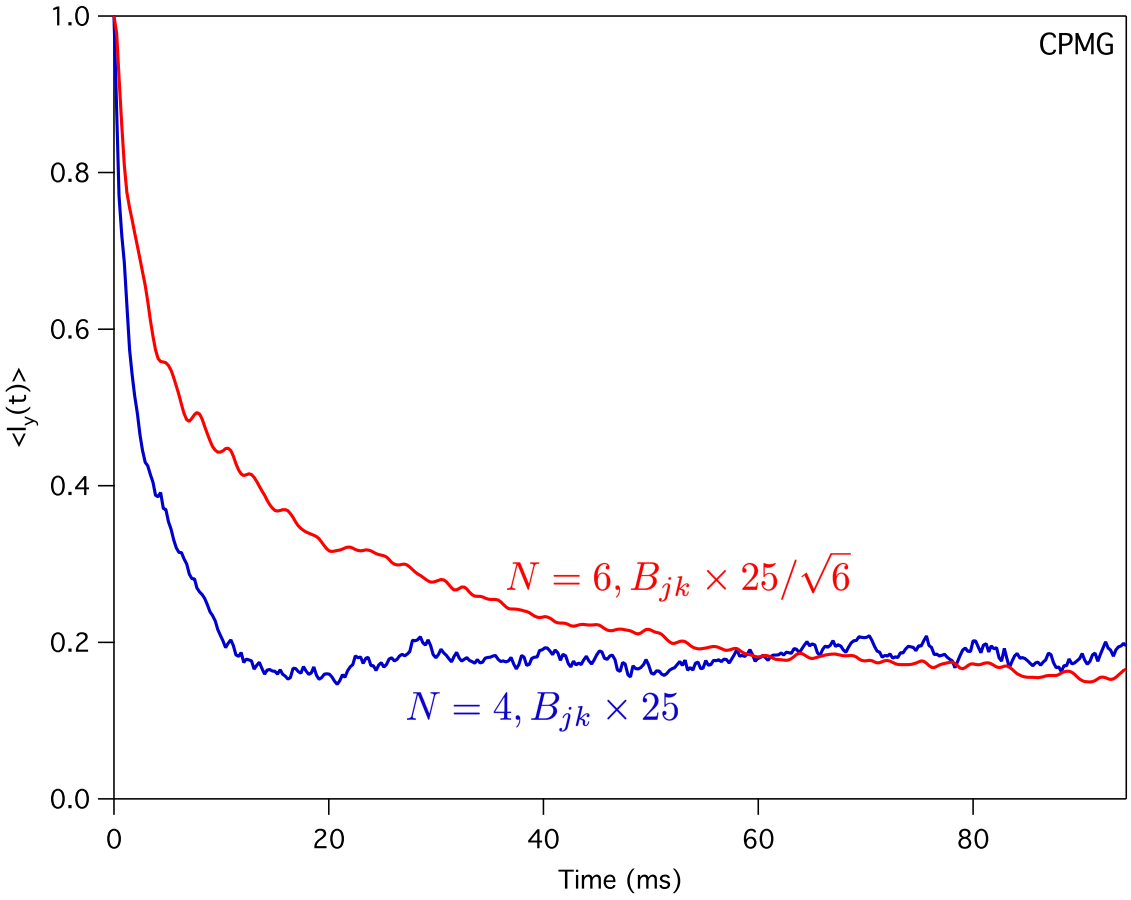

Figure 9.4: Exact calculations changing both dipolar coupling strength and system size. By adding more spins, the dipolar coupling strength can be reduced to yield a similar tail height in CPMG. Parameters: $\Omega_z = 0$, $H_1 = 40$ kHz, $2\tau = 2$ μs, 400 DR average.

coherence that depends on N.

Since the CPMG tail height is sensitive to both the dipolar coupling strength and the system size, we performed a comparative calculation in an attempt to extrapolate the results of Figure 8.3 towards a system with large N and weak B_{jk} (as in silicon). Figure 9.3 shows a pair of calculations where N is increased while B_{jk} is decreased. The $N = 4$ spin calculation uses a dipolar coupling strength 25 times stronger than that of silicon, while the $N = 6$ spin calculation uses a reduced dipolar coupling strength of $25/\sqrt{6}$ times that of silicon. We reduced the dipolar coupling strength by the ratio of the system sizes [27, 52, 55] $\|I_{z_T}\| = \sqrt{\mathrm{Tr}\{I_{z_T}^2\}} = \sqrt{N2^{(N-2)}}$ in order to keep $\|\mathcal{H}_{zz}\|$ constant between the two calculations. The relative agreement in the calculated CPMG tail height supports the notion that small

systems of strongly coupling spins share similarities with large systems of weakly coupled spins.

These scaling calculations show that the total dipolar energy of the system, which increases with system size, is an important parameter in finite π pulse effects. It is unknown whether a saturation would occur at some large N or how strong the pulses need to be in a real system so that the delta-function pulse approximation can safely be invoked.

9.4 Choices for the Set of Dipolar Coupling Strengths

In Chapter 5, Section 5.4, the method for calculating the expectation value $\langle I_y \rangle$ for N spins on a lattice was described. In all the exact and average Hamiltonian calculations shown since Chapter 8, we have used the silicon lattice as a model and as a qualitative comparison to the real data from Chapters 4, 6, and 7. Additionally, the calculations selected the N spins based on their dipolar coupling strength to the spin at the origin. In other words, some spins that appear on the lattice are ignored if the coupling constant to the origin B_{1k} is weaker than the rest.

This method for selecting the set of N spins depends on the form of the dipolar coupling expression

$$B_{jk} \equiv \frac{1}{2}\frac{\gamma^2\hbar^2}{|\vec{r}_{jk}|^3}(1 - 3\cos^2\theta_{jk}) \tag{9.30}$$

where γ is the gyromagnetic ratio, $\vec{r}_{jk}$ is the position vector between spins j and k, and θ_{jk} satisfies $\vec{r}_{jk} \cdot \vec{B}^{\text{ext}} = |\vec{r}_{jk}||\vec{B}^{\text{ext}}|\cos(\theta_{jk})$ defined for an externally applied magnetic field $\vec{B}^{\text{ext}}$ parallel to $\hat{z}$. Spins too far from the origin couple weakly since B_{jk} falls as $1/|\vec{r}_{jk}|^3$. Also, spins oriented close to the magic angle have small coupling to the origin since at the magic angle $(1 - 3\cos^2\theta_{jk}) = 0$.

Originally, this method of selecting which spins to include in the calculation was chosen in order to enhance the influence of the coupling on the central spin since we calculate $\langle I_{y_1} \rangle$. The disadvantage of this method of picking by coupling strength is the artificial discrimination of spins in a cone about the magic angle. Those excluded spins could otherwise couple strongly to their neighbors and thus indirectly affect the central spin. By excluding these spins, we may not be representing a naturally random set of spins on a lattice. Therefore,

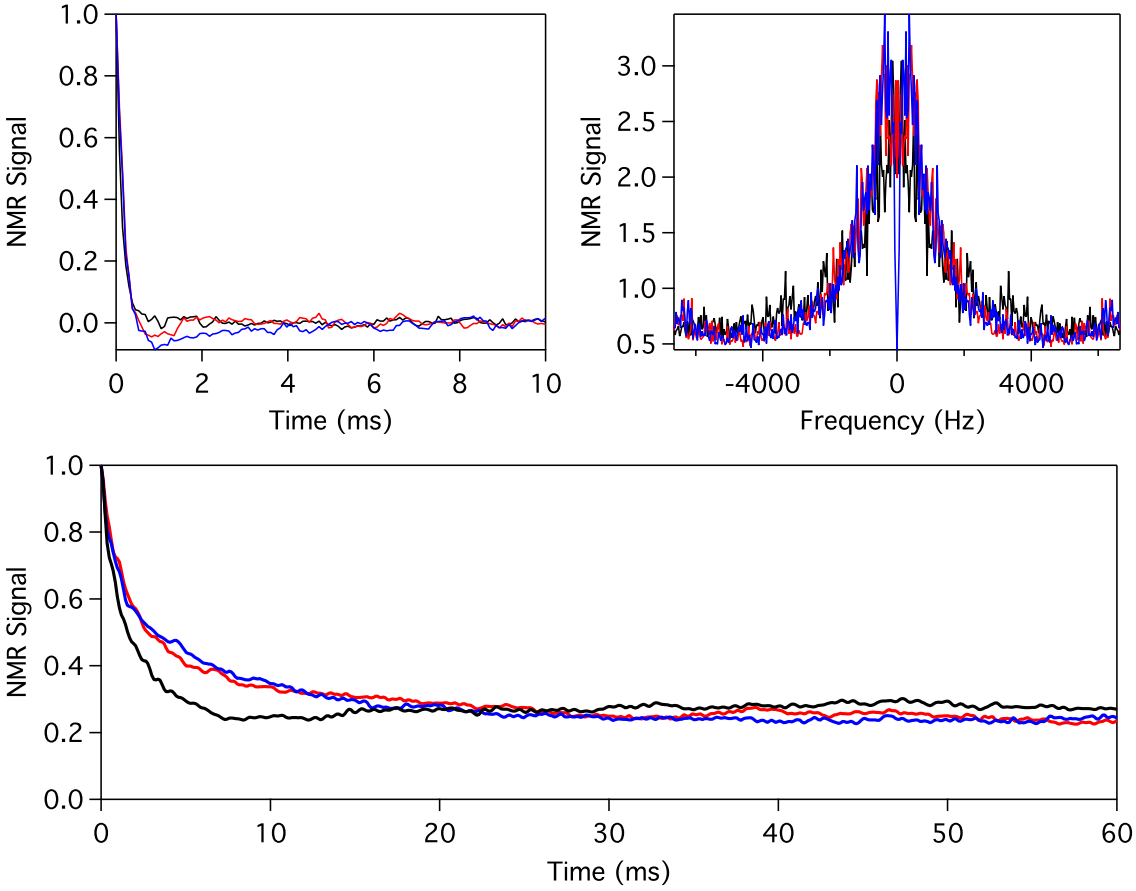

Figure 9.5: Three ways to choose the $N = 6$ spins for calculations: In all graphs red curves show calculations where spins are selected by their distance to the origin on a silicon lattice, blue curves show calculations were spins are selected based on their coupling strength to the origin on a silicon lattice, and black curves show calculations where the coupling constants are selected from a random Lorentzian distribution of coupling constants that match those on the disorder averaged silicon lattice. Top left graph shows the calculated FID. Top right graph shows the calculated spectrum. Bottom graph shows an average Hamiltonian calculation of $\bar{\mathcal{H}}^{(0)}_{\mathrm{CPMG}} + \bar{\mathcal{H}}^{(1)}_{\mathrm{CPMG}}$ where $t_p = 12.5\ \mu$s, $2\tau = 2\ \mu$s, and the coupling strength is $25\times$ that of ^{29}Si in silicon.

presented here are two other methods of selecting the set of N spins and their effects on the calculations.

The first alternative builds the proper lattice as before but sorts the lattice sites by their distance from the origin in a list. Then the lattice is randomly populated according to its natural abundance (in the case of silicon it is 4.67% n.a.). The first N populated spins in the list are included in the calculation, thus producing a small cluster of N spins in proximity to the origin. The advantage of this method is that it creates a more spherical cluster of spins. Additionally, by including the possibility of weak coupling constants, this method is more representative of the actual set of couplings that may be found in a natural cluster of spins. However, this method is still greatly limited by the small number $N < 10$ spins that we are computationally able to handle. Spins just outside the border of the cluster are excluded even though their contribution to $\langle I_{y_1} \rangle$ may be just as significant as those spins within the cluster.

The second alternative method eliminates the step of building a lattice altogether and instead randomly selects N coupling constants from a Lorentzian distribution that matches the disorder averaged distribution of coupling constants on the real lattice. The advantage of this method is that all possible coupling strengths are represented with their appropriate likelihood, with weak couplings being more likely than strong couplings. This feature can also be considered a disadvantage since in any single set of coupling constants, there is no proximity relationship between spins. In this case there is no origin spin and the set of coupling strengths might not be physically realizable.

The three methods for selecting the N spins are used in Figure 9.5 to calculate the free induction decay (FID), the Fourier transformed spectrum, and the CPMG tail. As the figure shows, the FID and the spectrum are qualitatively identical. In all three methods, the set of strong couplings appear to dominate the early time behavior. However in the CPMG average Hamiltonian calculation, the differences that show up in the set of weak couplings actually manifest in small changes in the shape of the CPMG tail.

None of these methods produce qualitatively different results, i.e. the long-lived tail still appears with a flat slope and roughly the same height for the given parameters. Still, the sensitivity of the calculations on the choice of the couplings appears to be consistent with the notion that the dynamics of all the spins contribute to the surprising observable coherence.

In the next chapter we discuss how coherence transfer pathways that depend on the set of coupling strengths and the number of spins may dynamically lead to the observed effects.

Chapter 10

Hidden Order in the Density Matrix

The multiple-pulse experiments and calculations presented thus far have been concerned with the disorder-averaged expectation value $\langle I_{y_1}(t)\rangle = \mathrm{Tr}\{\rho(t) I_{y_1}\}$. We can gain more insight into the full quantum dynamics of the spin system by visualizing the time-evolution of $\rho(t)$, both for a single disorder realization (DR), and for an average over many DRs.

10.1 Visualizing the Dynamic Density Matrix

For an $N = 6$ spin system, $\rho(t)$ is a $2^6 \times 2^6$ matrix [18, 79] of complex numbers $z = re^{i\theta}$ that is difficult to present in compact form. Since the initial state of the system following the 90_X pulse is $\rho(0) = I_{y_T}$, we found it convenient to visualize the state of $\rho(t)$ using a red-white-blue color scale to represent the phase angle θ of each cell in $\rho(t)$. Any cells that have magnitudes $r < 1/10$ of the largest initial magnitudes are colored black.

We start with the calculation for the case of CPMG with delta-function π pulses as we have outlined in Chapter 4. By setting the Zeeman spread $\Omega_z = 0$, the evolution of $\rho(t)$ is caused by the dipolar Hamiltonian alone.

Figures 10.1 & 10.2 show the calculated disorder averaged expectation value $\langle I_y(t)\rangle$ for $N = 6$ spins coupled by the truncated Ising Hamiltonian (Figure 10.1)

$$\mathcal{H}_{\text{Ising}} = \sum_{j=1}^{N} \sum_{k>j}^{N} 2B_{jk} I_{z_j} I_{z_k} \tag{10.1}$$

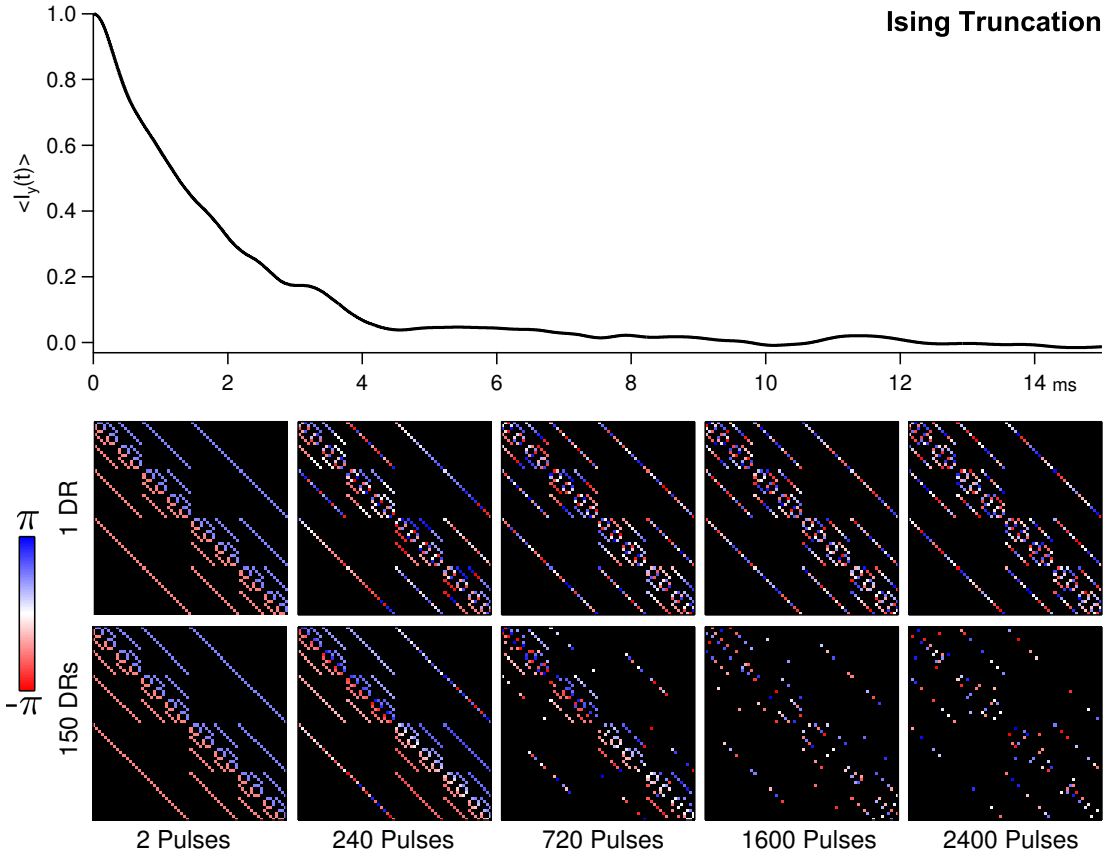

Figure 10.1: Dipolar decay of $\langle I_{y_1}(t)\rangle$ with snapshots of the z-basis density matrix evolving in time under the Ising Hamiltonian. Parameters: $N = 6$, $\rho(0) = I_{y_T}$, $\Omega_z = 0$, $t_p = 12.2$ μs, $2\tau = 2$ μs, $25 \times B_{jk}$ of ^{29}Si in silicon, and $B_{jk} = 0$ during pulses. The phase is colored on a red-white-blue color scale (inset). Cells are set to black if their magnitude is less than $1/10$ of the largest initially filled cells. In a single disorder realization (DR) the initial phase coherence is lost after many pulses using $\mathcal{H}_{\text{Ising}}$. After an average over 150 DRs, the initial state has decayed.

or by the secular dipolar Hamiltonian (Figure 10.2)

$$\mathcal{H}_{zz} = \sum_{j=1}^{N}\sum_{k>j}^{N} 2B_{jk}\Big[I_{z_j}I_{z_k} - \frac{1}{4}(I_j^+ I_k^- + I_j^- I_k^+)\Big] \tag{10.2}$$

along with snapshots of the corresponding density matrix for each case.

In a single disorder realization (DR), the final density matrix under $\mathcal{H}_{\text{Ising}}$ looks very similar to the initial density matrix, however the phase of each nonzero element has been scrambled from its initial phase. The scrambled phase in a single DR translates to a decay of the magnitude in the average over 150 DRs and thus also the decay of $\langle I_{y_1}(t)\rangle$.

The secular dipolar Hamiltonian also scrambles the phase of the density matrix as it evolves in time. In a single DR, $\mathcal{H}_{zz}$ also spreads coherence to additional cells in the density matrix. The mechanism responsible for the spreading of coherence in this case are the flip-flop terms of $\mathcal{H}_{zz}$. These terms allow the transitions between spin-states that conserve z-angular momentum. Both the flip-flop terms and the initial density matrix proportional to I_{y_T} dictate the possible cells that can be reached after time-evolution [18, 79, 11]. Through both the scrambling of the phase and the spread of coherence, the evolution of the density matrix for delta-function pulses leads to decay in the disorder average.

For finite pulses, the evolution of the density matrix can be very different. Figures 10.3, 10.4, 10.5, and 10.6 show the density matrix as it evolves under the four pulse sequences

$$\begin{aligned}
\text{CP} &: 90_X - \tau - \{180_X - 2\tau - 180_X - 2\tau\}^n \\
\text{APCP} &: 90_X - \tau - \{180_{\bar{X}} - 2\tau - 180_X - 2\tau\}^n \\
\text{CPMG} &: 90_X - \tau - \{180_Y - 2\tau - 180_Y - 2\tau\}^n \\
\text{APCPMG} &: 90_X - \tau - \{180_{\bar{Y}} - 2\tau - 180_Y - 2\tau\}^n
\end{aligned}$$

where the internal Hamiltonian is present during the strong but finite pulses. In contrast to the delta-function pulse approximation, these pulse sequences allow much more coherence transfer to different cells of the density matrix. In particular, for the CP and CPMG sequences, the spread of coherence has reached every single cell of the $2^6 \times 2^6$ density matrix after evolving under 300 strong but finite π pulses.

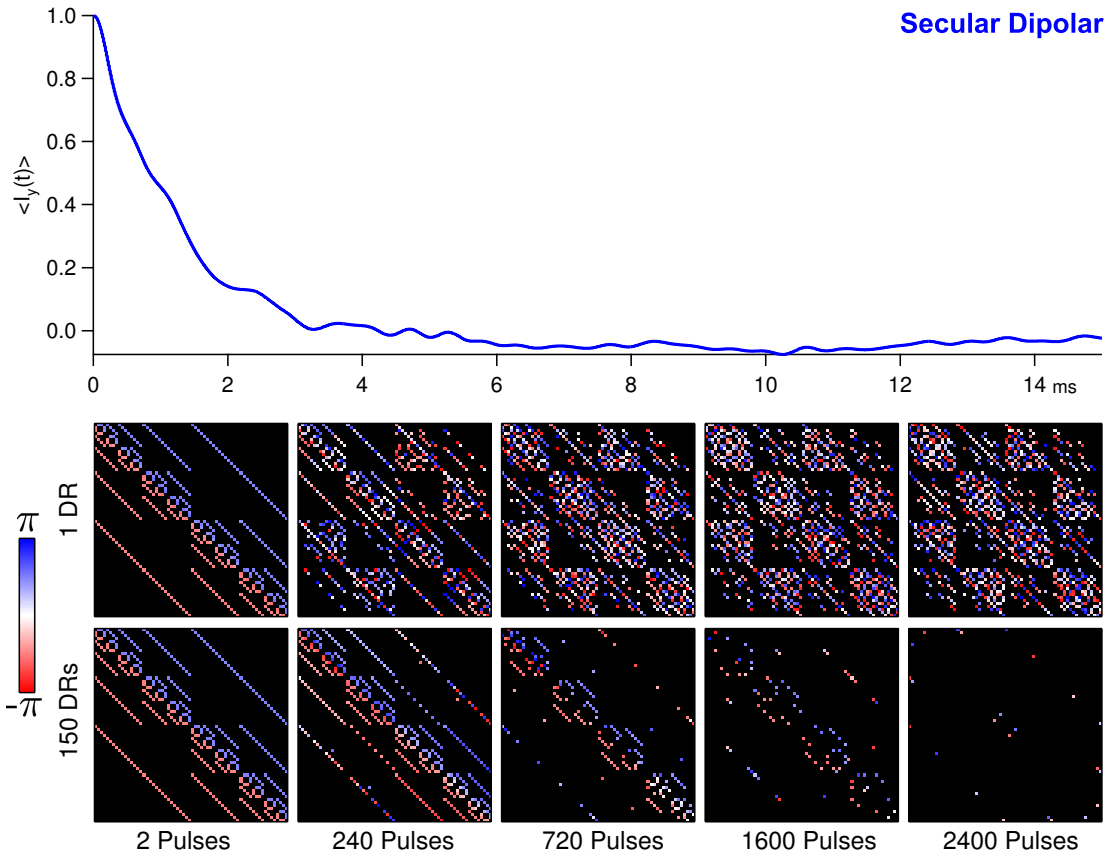

Figure 10.2: Dipolar decay of $\langle I_{y_1}(t)\rangle$ with snapshots of the z-basis density matrix evolving in time under the secular dipolar Hamiltonian. Parameters: $N = 6$, $\rho(0) = I_{y_T}$, $\Omega_z = 0$, $t_p = 12.2\ \mu$s, $2\tau = 2\ \mu$s, $25 \times B_{jk}$ of ^{29}Si in silicon, and $B_{jk} = 0$ during pulses. The phase is colored on a red-white-blue color scale (inset). Cells are set to black if their magnitude is less than $1/10$ of the largest initially filled cells. In a single disorder realization (DR) the initial phase coherence is lost after many pulses using using $\mathcal{H}_{zz}$, which spreads coherence to other parts of the density matrix and mixes their phase. After an average over 150 DRs, the initial state has decayed.

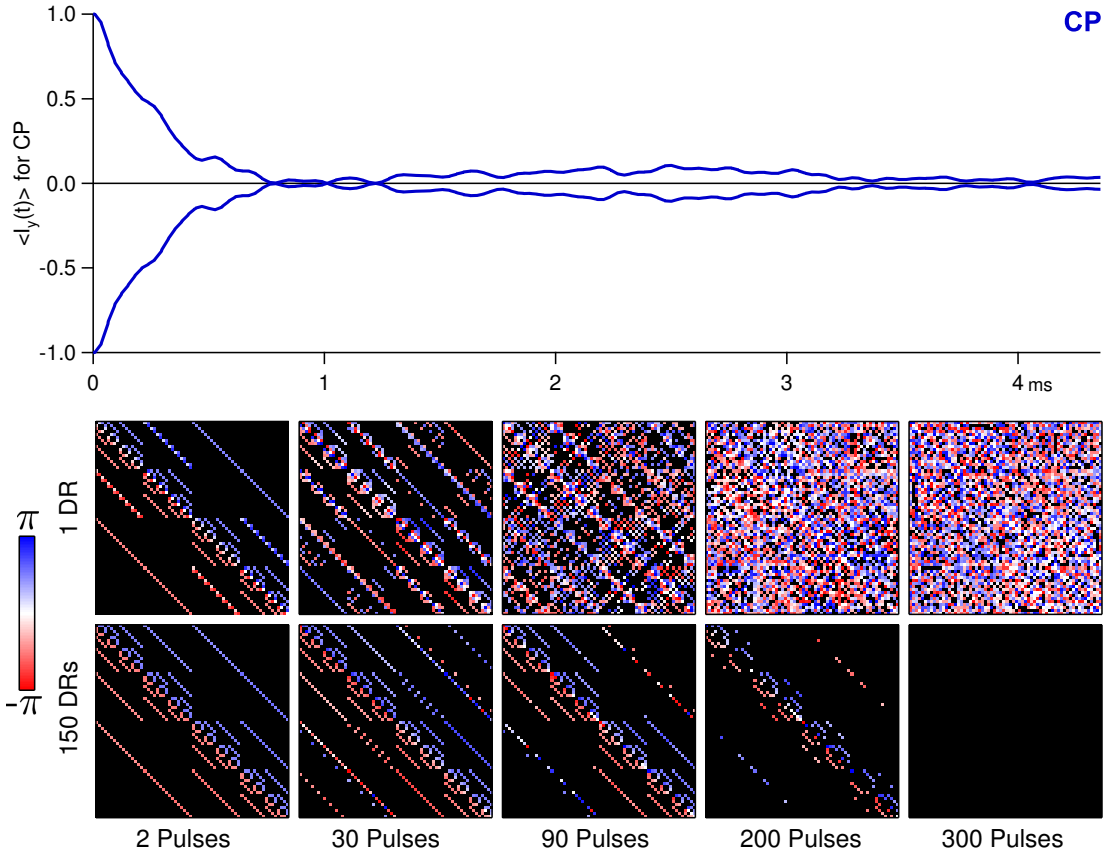

Figure 10.3: Snapshots of the Density Matrix with Finite Pulses Under CP. Expectation value $\langle I_{y_1}(t)\rangle$ and the density matrix $\rho(t)$ as they evolve under The Carr-Purcell multiple π pulse sequence with $N = 6$, Ω_z drawn from a 3 kHz wide Gaussian, $25 \times B_{jk}$ of ^{29}Si in silicon, $H_1 = 40$ kHz, $2\tau = 2$ μs. The phase is colored on a red-white-blue color scale (inset). Cells with negligible magnitude are colored black. Compare the single DR density matrix snapshots with those of Figures 10.1 & 10.2. Much more coherence is spread about the density matrix in these exact calculations, yet the disorder average can yield long-lived coherence (CPMG and APCP) as well as fast decay (CP and APCPMG).

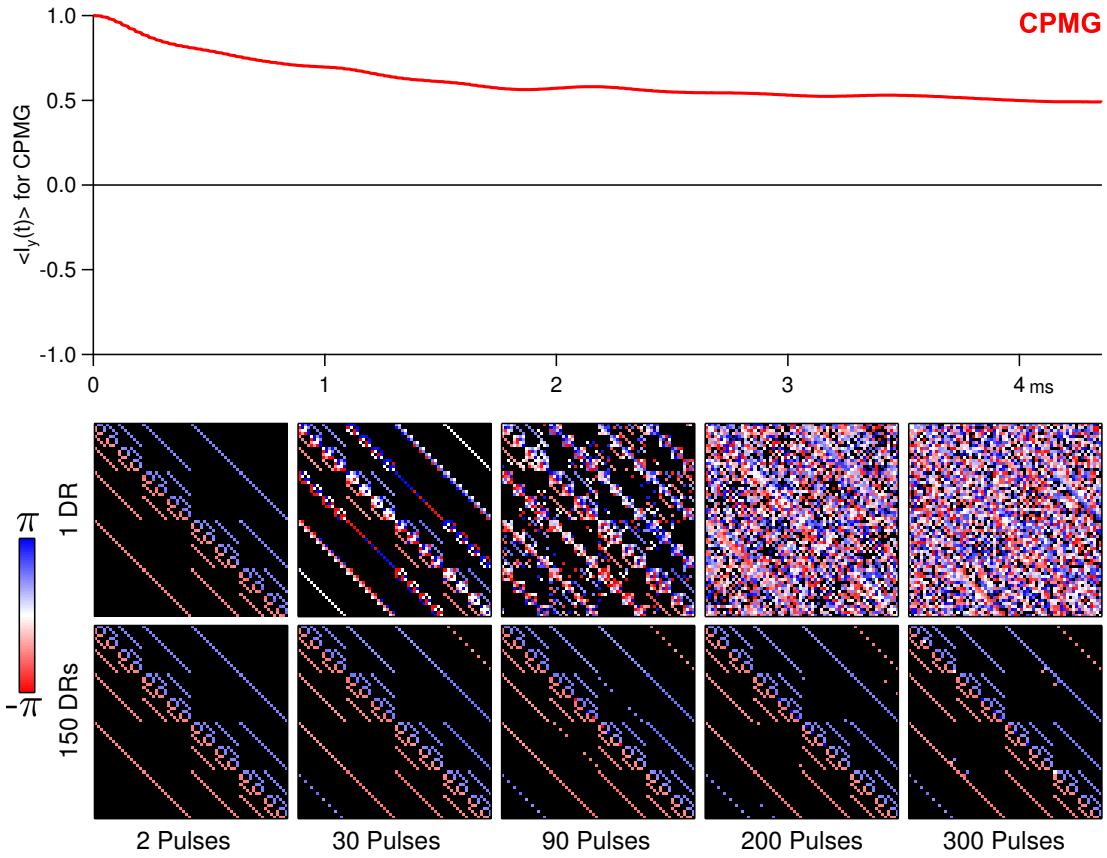

Figure 10.4: Snapshots of the Density Matrix with Finite Pulses Under CPMG. Expectation value $\langle I_{y_1}(t)\rangle$ and the density matrix $\rho(t)$ as they evolve under the Carr-Purcell-Meiboom-Gill multiple π pulse sequence with $N = 6$, Ω_z drawn from a 3 kHz wide Gaussian, $25 \times B_{jk}$ of ^{29}Si in silicon, $H_1 = 40$ kHz, $2\tau = 2$ μs. The phase is colored on a red-white-blue color scale (inset). Cells with negligible magnitude are colored black. Compare the single DR density matrix snapshots with those of Figures 10.1 & 10.2. Much more coherence is spread about the density matrix in these exact calculations, yet the disorder average can yield long-lived coherence (CPMG and APCP) as well as fast decay (CP and APCPMG).

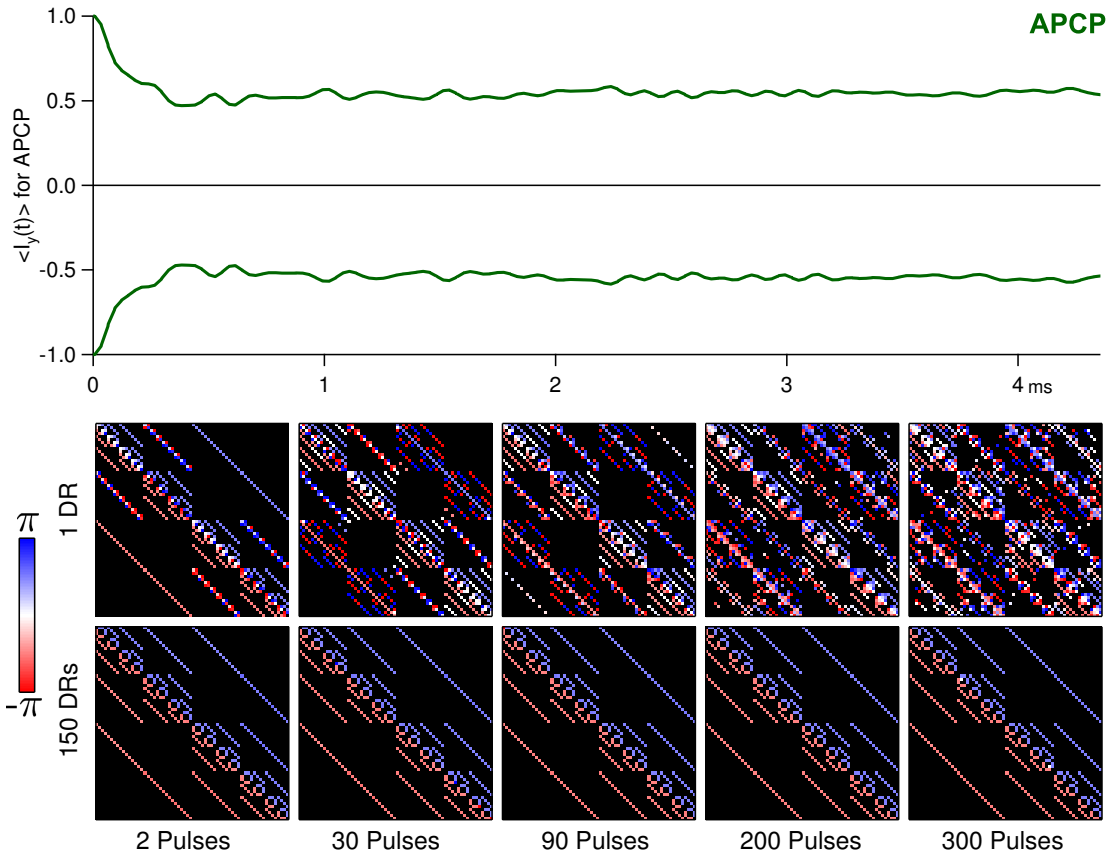

Figure 10.5: Snapshots of the Density Matrix with Finite Pulses Under APCP. Expectation value $\langle I_{y_1}(t)\rangle$ and the density matrix $\rho(t)$ as they evolve under the Alternating-Phase Carr-Purcell multiple π pulse sequence with $N = 6$, Ω_z drawn from a 3 kHz wide Gaussian, $25 \times B_{jk}$ of ^{29}Si in silicon, $H_1 = 40$ kHz, $2\tau = 2$ μs. The phase is colored on a red-white-blue color scale (inset). Cells with negligible magnitude are colored black. Compare the single DR density matrix snapshots with those of Figures 10.1 & 10.2. Much more coherence is spread about the density matrix in these exact calculations, yet the disorder average can yield long-lived coherence (CPMG and APCP) as well as fast decay (CP and APCPMG).

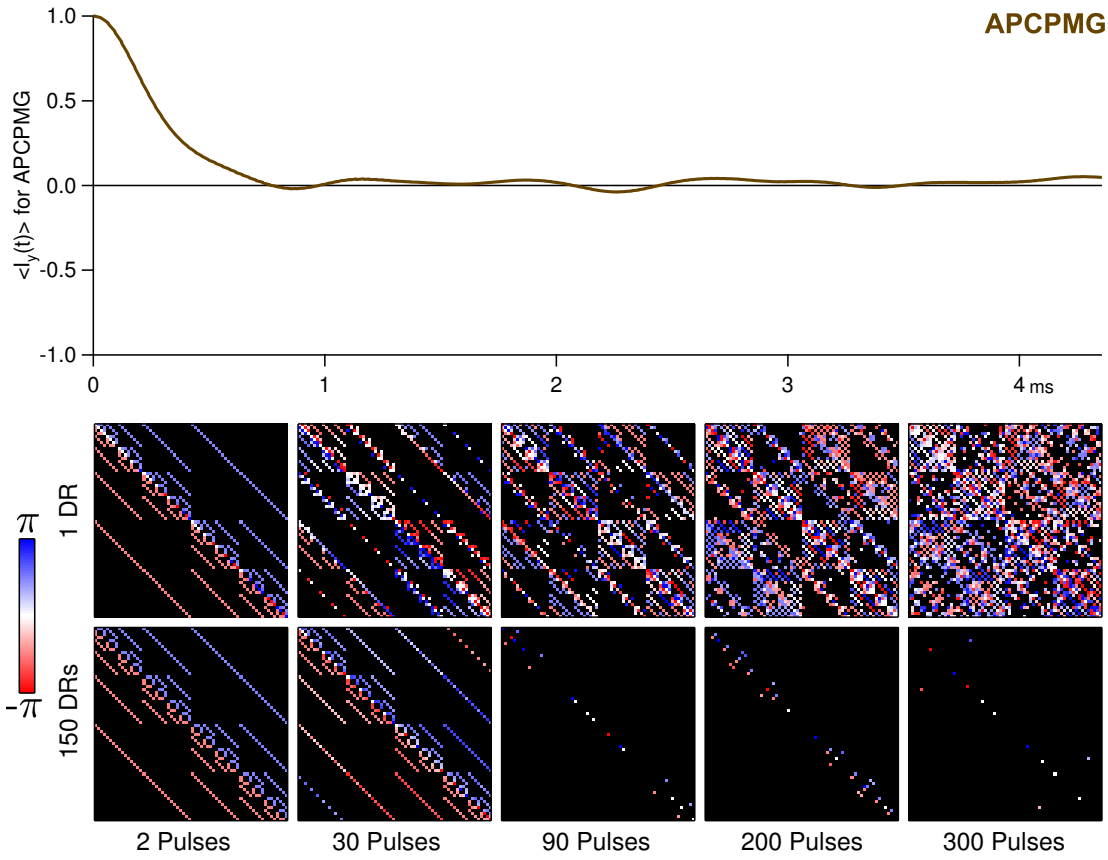

Figure 10.6: Snapshots of the Density Matrix with Finite Pulses Under APCPMG. Expectation value $\langle I_{y_1}(t)\rangle$ and the density matrix $\rho(t)$ as they evolve under the Alternating-Phase Carr-Purcell-Meiboom-Gill multiple π pulse sequence with $N = 6$, Ω_z drawn from a 3 kHz wide Gaussian, $25 \times B_{jk}$ of ^{29}Si in silicon, $H_1 = 40$ kHz, $2\tau = 2$ μs. The phase is colored on a red-white-blue color scale (inset). Cells with negligible magnitude are colored black. Compare the single DR density matrix snapshots with those of Figures 10.1 & 10.2. Much more coherence is spread about the density matrix in these exact calculations, yet the disorder average can yield long-lived coherence (CPMG and APCP) as well as fast decay (CP and APCPMG).

10.2 Quantum Coherence Transfer Pathways and the "Knock-Out" Sequence

The average Hamiltonian expressions for the four pulse sequences give us a better understanding of the mechanism of coherence flow to other cells of the density matrix for the case of finite pulses. For example, the APCP sequence has a zeroth order Average Hamiltonian

$$\begin{aligned}\mathcal{H}^{(0)}_{\mathrm{APCP}} &= \sum_{j=1}^{N}\sum_{k>j}^{N} B_{jk}\Big[\kappa_1 I_{z_j} I_{z_k} + \kappa_2(I_j^+ I_k^- + I_j^- I_k^+) \\ &\quad +\kappa_3(I_j^+ I_k^+ + I_j^- I_k^-)\Big] + \kappa_4(I_j^+ - I_j^-) \end{aligned} \tag{10.3}$$

when expressed using the raising and lowering operators. Here, $\kappa_1 = \frac{8\tau+t_p}{t_c}$, $\kappa_2 = \frac{4\tau+t_p}{4t_c}$, $\kappa_3 = -\frac{3t_p}{4t_c}$, $\kappa_4 = -i\frac{2\Omega_z t_p}{\pi t_c}$. The last two terms in equation (10.3) do not appear in the Hamiltonian under the delta-function pulse approximation [equation (10.2)]. Furthermore, these terms are distinct because they do not conserve z-angular momentum. The appearance of these novel terms is yet another intrinsic property of the finite pulse. Regardless of how well real pulses are engineered to reduce t_p, unless t_p is exactly zero, these extra terms will enable the spread of coherence to parts of the density matrix fundamentally forbidden in the delta-function pulse approximation. Thus, after the application of many π pulses, the final density matrix will be nowhere near the expected result, if we fail to consider the action of real pulses.

The significance of our argument for NMR would be lost if these extra coherence transfer pathways only led to an imperceptible difference in the decay of $\langle I_{y_1}(t)\rangle$. However, as Figures 10.3, 10.4, 10.5, and 10.6 show, the enhanced spread of coherence in a single DR can surprisingly preserve the measurable coherence (CPMG and APCP) or lead to decay (CP and APCPMG) in the disorder average depending on the phase of the π pulses. Thus, it is of considerable importance to understand the entire density matrix since real pulses connect all cells back to the measurable channel.

To illustrate the influence of these new coherence transfer pathways [18] to the measurable cells, we performed a "knockout" calculation [16] that periodically zeroes cells in the density matrix that should always be zero under the secular dipolar Hamiltonian and delta-function π pulses [i.e. cells that remain black in Figure 10.2 after 2400 pulses in 1

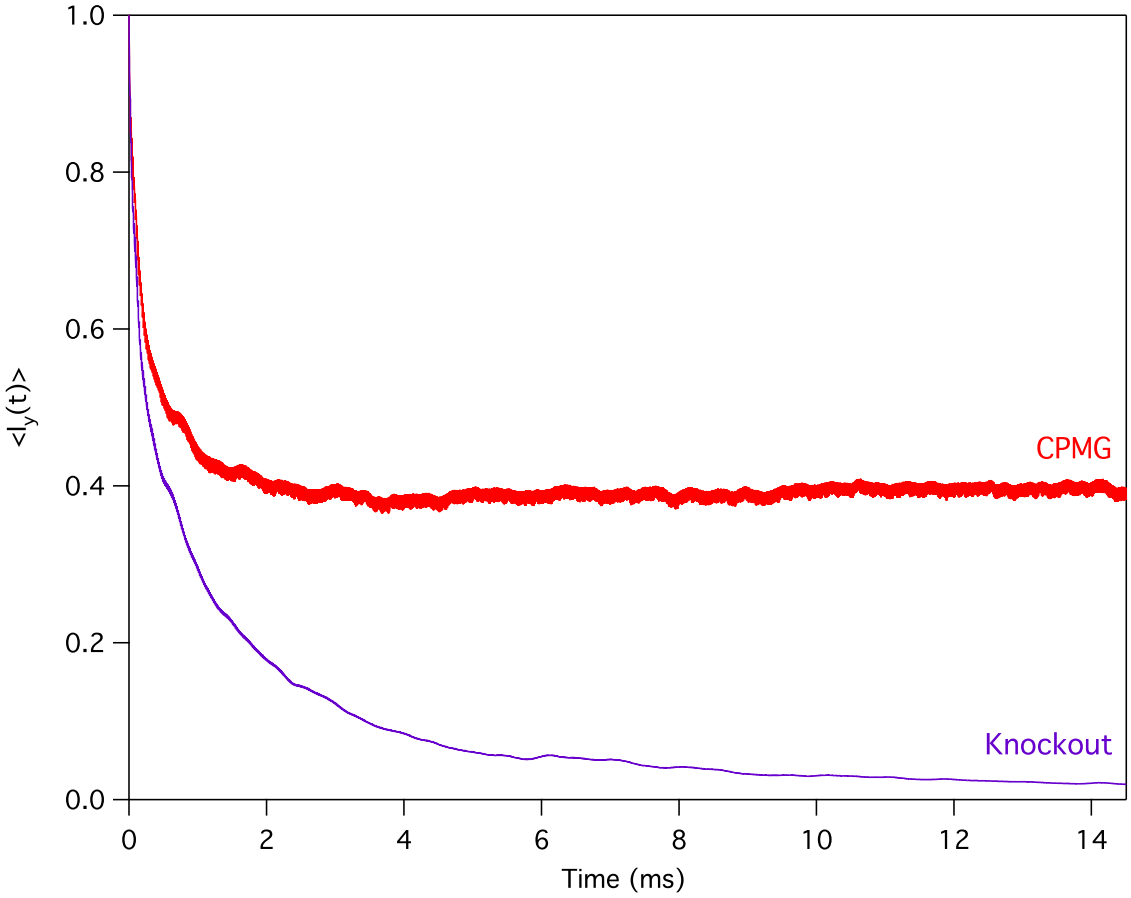

Figure 10.7: Knockout calculations for CPMG. Parameters: N=6, $150 \times B_{jk}$ of ^{29}Si in silicon, $\Omega_z = 0$, $H_1 = 40$ kHz, $2\tau = 2$ μs, and 400 DR average. The "knockout" trace (purple), is calculated by deleting density matrix cells with quantum coherence order $q \neq \pm 1$ after each π pulse. (The delta-function pulse approximation assumes all coherence stays as $q = \pm 1$ for all time.) The long tail in the exact CPMG calculation (red) requires coherence transfer pathways between all quantum coherences [18, 79, 16].

DR]. The red curve in Figure 10.7 is the disorder averaged $\langle I_{y_1}(t)\rangle$ for the CPMG sequence with a long-lived tail. The purple curve is the same CPMG pulse sequence but applies the "knockout" procedure after each π pulse and in each DR. Because of the drastic decay of the "knockout" curve, we infer that not only do these extra coherence transfer pathways exist, but they allow coherence to constructively flow back to the measurable channel leading to the long tail in the CPMG sequence.

These "knockout" calculations were performed by Yanqun Dong. I am grateful to her for allowing me to present them in my thesis.

Chapter 11

Advanced Finite Pulse Sequences

Understanding the underlying causes for the observed finite pulse effects not only enables the identification of quantum coherence transfer pathways but also the manipulation of coherences. In this chapter, we present two advanced pulse sequences based on the the alternating phase pulse sequences described in earlier chapters.

11.1 The Super Hahn Echo

The rapid signal decay in the APCPMG sequence is roughly understood as being caused by the analogous term in the average Hamiltonian that keeps APCP from decaying. The zeroth order average Hamiltonian for APCPMG is

$$\bar{\mathcal{H}}^{(0)}_{\mathrm{APCPMG}} = \frac{1}{t_c}(4\tau\mathcal{H}_{zz} - t_p\mathcal{H}_{yy} - \frac{4\Omega_z}{\pi}t_p I_{x_T}). \tag{11.1}$$

The last term in equation (11.1) acts to dephase any signal that builds up along I_y since it can be interpreted as a constant field along $\hat{x}$.

In comparison, the full Hamiltonian in the absence of pulses is

$$\mathcal{H} = \sum_{i=1}^{N} \Omega_z I_z + \mathcal{H}_{zz}. \tag{11.2}$$

As we have described in Chapter 5, the Zeeman part of the Hamiltonian may cause an initial free induction decay due to the spread of Zeeman energies Ω_z. However, a properly timed π pulse can refocus this spread of Zeeman energies into a Hahn spin echo.

Just as we applied π pulses to refocus the Zeeman energy spread into echoes, we can try to apply π pulses to refocus the loss of signal due to the I_x term in equation (11.1). Note

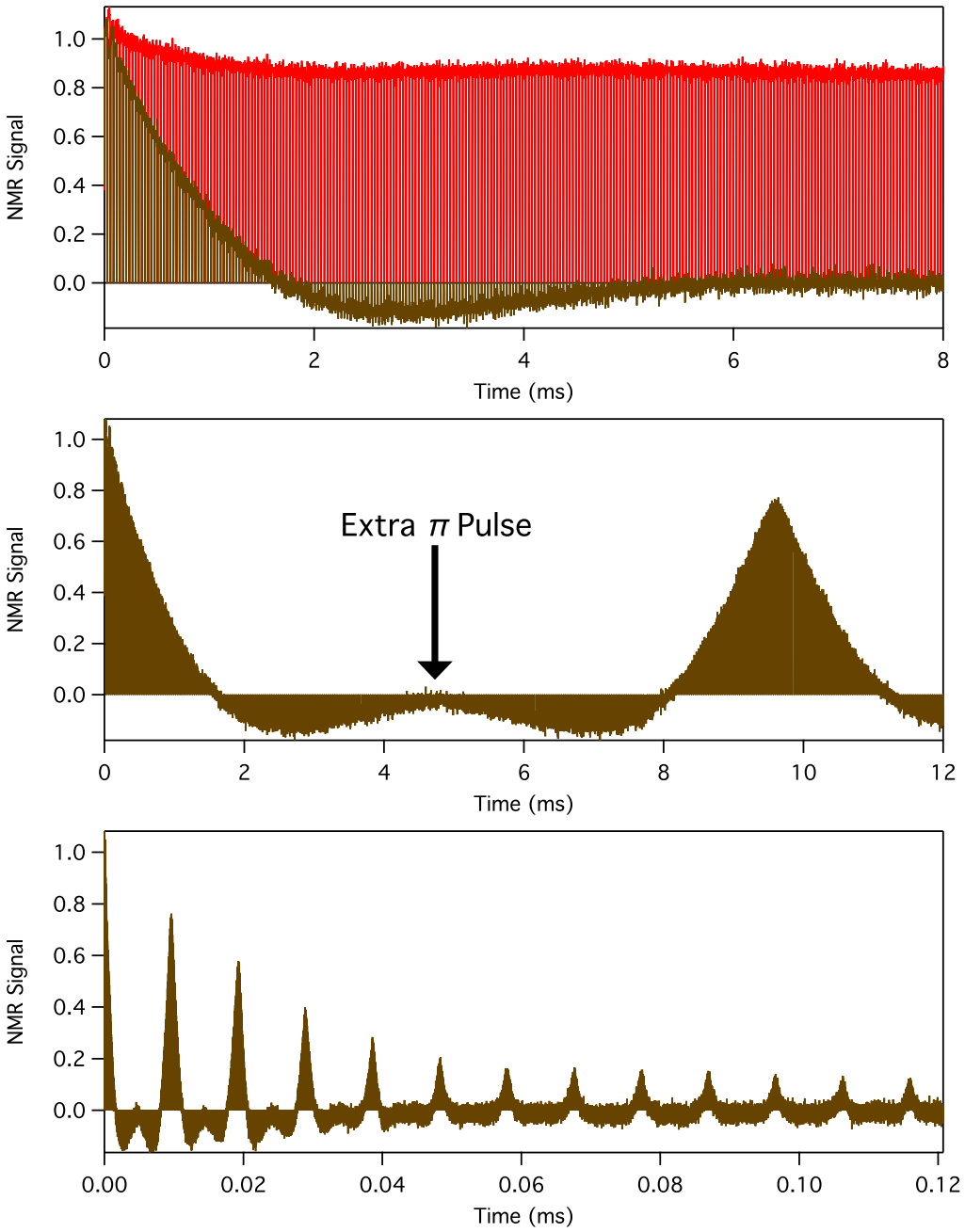

Figure 11.1: NMR data for ^{13}C nuclei in C_{60} at room temperature in a 12 Tesla field. Top graph shows the decaying APCPMG echo train (brown) compared to the long-lived tail in CPMG (red). Middle graph applies one additional π pulse along $\hat{y}$ among the many π pulses already applied in APCPMG. The measurable coherence returns in an echo of echoes. Bottom graph shows the application of 12 additional π pulses to give an echo train of Super Hahn Echoes.

that a π pulse along $\hat{x}$ would do nothing to change the sign of I_x, while a π pulse along $\hat{y}$ changes

$$-\frac{4\Omega_z}{\pi}t_p I_{x_T} \rightarrow +\frac{4\Omega_z}{\pi}t_p I_{x_T}. \tag{11.3}$$

Alternatively, the phase of the π pulses in the APCPMG sequence can be inverted to give the same result. That is, the two sequences

$$\begin{aligned} \text{APCPMG}: &\quad 90_X - \{\tau - 180_{\bar{Y}} - 2\tau - 180_Y - \tau\} \\ \text{flip}-\text{APCPMG}: &\quad 90_X - \{\tau - 180_Y - 2\tau - 180_{\bar{Y}} - \tau\} \end{aligned}$$

differ in their zeroth order average Hamiltonian for the period within the brackets $\{\}$ just in the sign of $-\frac{4\Omega_z}{\pi}t_p I_{x_T}$ for APCPMG and $+\frac{4\Omega_z}{\pi}t_p I_{x_T}$ for flip-APCPMG.

In either case, changing the sign of the dephasing term should produce a time reversal of its effects from one period to the next. Figure 11.1 shows NMR data taken by Rona G. Ramos of ^{13}C in C_{60} where the APCPMG sequence is applied with and without the additional π pulse. The measurable coherence is refocused in the APCPMG echo train. We call this echo of echoes the Super Hahn Echo.

$$\begin{aligned} \text{Super Hahn Echo}: &\quad 90_X - \{\tau - 180_{\bar{Y}} - 2\tau - 180_Y - \tau\}^m 180_Y \{\tau - 180_{\bar{Y}} - 2\tau - 180_Y - \tau\}^n \\ \text{Super Hahn Echo}': &\quad 90_X - \{\tau - 180_{\bar{Y}} - 2\tau - 180_Y - \tau\}^m \{\tau - 180_Y - 2\tau - 180_{\bar{Y}} - \tau\}^n \end{aligned}$$

In the above two sequences the peak of the Super Hahn Echo nominally occurs when $m = n$. The first sequence uses an additional 180_Y pulse between two brackets of APCPMG while the second sequence only changes the second bracket $\{\}$ to flip-APCPMG.

More than one additional π pulse may be applied during the APCPMG sequence to yield a super echo train as shown in Figure 11.1(bottom). Or, to achieve the same effect, one could alternate between blocks of APCPMG and flip-APCPMG sequences.

If we assume delta-function π pulses, then either of these sequences would yield the same decay curve as calculated in Chapter 5. Though we use strong π pulses compared to the spread of Zeeman energies, their finite time duration plays a very crucial role.

11.2 The Super Magic Echo

The total average Hamiltonian during a long continuous pulse along $\hat{y}$ is

$$\bar{\mathcal{H}} = -\frac{1}{2}\mathcal{H}_{yy} \tag{11.4}$$

because the oscillating non-secular terms average away in time. The Lee-Goldburg experiment [41] exploits the minus sign in this Hamiltonian to refocus the decay caused by the dipolar Hamiltonian $\mathcal{H}_{zz}$.

The special trick is to change $\mathcal{H}_{yy}$ into $\mathcal{H}_{zz}$ in equation (11.4). This transformation is achieved by applying two X-phase $\pi/2$ pulses around the long continuous θ_Y pulse.

$$\text{Magic Echo} : 90_{\bar{X}}\theta_Y 90_X$$

Written in operator form, this sequence is

$$\begin{aligned}
\rho(t) &= \mathcal{P}_{90_X}\mathcal{P}_{\theta_Y}\mathcal{P}_{90_{\bar{X}}}\rho(0)\{inv\} && (11.5)\\
&\approx \exp(-i\frac{\pi}{2}I_x)\exp(-\frac{i}{\hbar}\bar{\mathcal{H}}t)\exp(+i\frac{\pi}{2}I_x)\rho(0)\{inv\} && (11.6)\\
&\approx \exp\Big[-\frac{i}{\hbar}(-\frac{1}{2}\mathcal{H}_{zz})t\Big]\rho(0)\{inv\} && (11.7)
\end{aligned}$$

where $\{inv\}$ is the inverse of the operators to the left of $\rho(0)$. We have assume that the 90 degree pulses are delta functions for simplicity and have used the average Hamiltonian form in equation (11.4) for the action during the θ_Y pulse.

After this set of pulses, the spin system would continue to evolve under the dipolar Hamiltonian as

$$\begin{aligned}
\rho(t+t') &\approx \mathcal{U}_z z(t')\exp\Big[-\frac{i}{\hbar}(-\frac{1}{2}\mathcal{H}_{zz})t\Big]\rho(0)\{inv\} && (11.8)\\
&\approx \exp\Big[-\frac{i}{\hbar}(+\mathcal{H}_{zz})t'\Big]\exp\Big[-\frac{i}{\hbar}(-\frac{1}{2}\mathcal{H}_{zz})t\Big]\rho(0)\{inv\}. && (11.9)
\end{aligned}$$

Then, if $t' = \frac{1}{2}t$ the dipolar evolution of the density matrix is canceled and returns to the initial density matrix

$$\rho(3t/2) \approx \rho(0). \tag{11.10}$$

To compensate for the additional presence of the Zeeman Hamiltonian $\mathcal{H}_Z$ one can periodically reverse the phase during the θ_Y pulse.

This Magic Echo sequence works very well in applications to dipolar systems but requires a long continuous pulse θ_Y to force the effective average Hamiltonian to reduce to $-\frac{1}{2}\mathcal{H}_{yy}$. From our understanding of the average Hamiltonian for finite multiple π pulse sequences, we can perform an analogous experiment to the Magic Echo but with short strong π pulses separated by time delays.

In Chapter 9, we introduced the notion of second averaging for the APCP sequence about the effective transverse field in the zeroth average Hamiltonian term

$$\bar{\mathcal{H}}^{(0)}_{\text{APCP}} = \frac{1}{t_c}(4\tau\mathcal{H}_{zz} - t_p\mathcal{H}_{xx} + \frac{4\Omega_z t_p}{\pi}I_{y_T}) \tag{11.11}$$

to yield

$$\bar{\bar{\mathcal{H}}}^{(0)}_{\text{APCP}} = -\frac{1}{t_c}(2\tau - \frac{t_p}{2})\mathcal{H}_{yy}. \tag{11.12}$$

Equation (11.12) is reminiscent of equation (11.4) but the overall sign depends on parameters τ and t_p, the interpulse spacing and the pulse duration respectively. The cycle time $t_c = 4\tau + 2t_p$ acts as an overall scaling factor. By controlling these two parameters, we are able to change the timing when the dipolar evolution is cancelled.

In order to achieve a strong second averaging, a large Zeeman spread Ω_z or a deliberate off-resonance field should be introduced during the APCP sequence. Similarly to the Magic Echo, we define the Super Magic Echo sequence

$$\text{Super Magic Echo} : 90_{\bar{X}}\Big\{90_X - [\tau - 180_{\bar{X}} - 2\tau - 180_X - \tau]^n\Big\}90_X$$

where the subsequence in red brackets {} is the APCP sequence with n cycles and set optionally off-resonance. By noticing that the first two pulses are of opposite phase with no time delay between them, we can simplify the sequence by dropping both pulses

$$\text{Super Magic Echo}' : \Big\{[\tau - 180_{\bar{X}} - 2\tau - 180_X - \tau]^n\Big\}90_X.$$

If we assume the delta-function pulse approximation, the Super Magic Echo′ sequence acting on a system of spins initially aligned along $\hat{z}$ at equilibrium should only produce an FID immediately after the 90_X pulse. In the delta-function pulse approximation, applying a set of π pulses to spins aligned along $\hat{z}$ should do nothing.

Simulations of the Super Magic Echo proved that the concepts were correct. However, when performing the SME sequence on ^{1}H nuclei in Adamantane, successful experimental results were initially not as easily obtained. The span of experimental parameters for

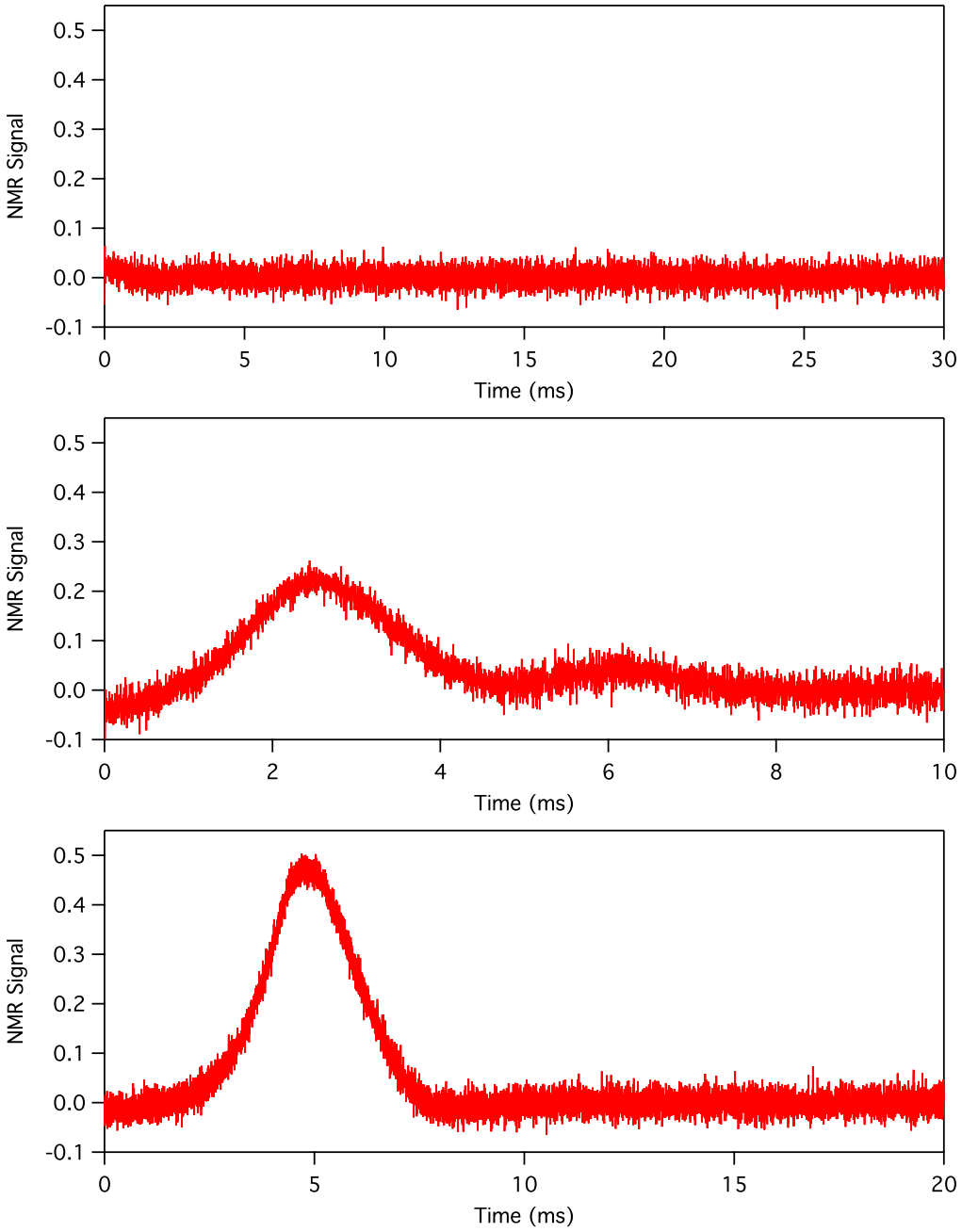

Figure 11.2: NMR data for ^{13}C nuclei in C_{60} at room temperature in a 12 Tesla field. Data is acquired after the last pulse in the sequence. Top graph shows the Super Magic Echo′ sequence but with a $90_{\bar{X}}$ pulse at the end instead of the proper 90_X pulse. No echo or FID forms. Middle graph shows the Super Magic Echo for the proper 90_X pulse. The timing of the Super Magic Echo depends on τ and t_p of the APCP burst. Bottom graph shows the Super Magic Echo″ sequence where the previous 90_X is replaced by $90_{\bar{X}} - t_{f1} - 180_Y$.

this sequence included sensitive timing parameters during the burst like τ, t_p, and t_{burst} as well as the off-resonance offset amount. In practice, only a small range of values led to the formation of the Super Magic Echo. These parameters were first successfully achieved in simulation and subsequently applied in experiment. From the simulations, we learned that the offset resonance frequency could not exceed approximately 25% of the H_1 strength or the average Hamiltonian expressions would require more higher order corrections that would spoil the formation of the Super Magic Echo.

Figure 11.2 shows NMR data by Rona G. Ramos where this sequence is applied to ^{13}C nuclei in C_{60}. The formation of the Super Magic Echo depends on τ and t_p during the APCP burst period as well as the phase of the final 90 degree pulse, which validates our understanding of the average Hamiltonian for multiple finite π pulses. The data in C_{60} was not as sensitive to the resonance frequency and did not require any offset to form the Super Magic Echo. We attribute this difference of the C_{60} sample to the larger spread of Zeeman energies found in C_{60} compared to its weaker dipolar coupling strength between ^{13}C nuclei. In contrast, Adamantane has a naturally smaller spread of Zeeman energies compared to the much stronger dipolar coupling strength between ^{1}H nuclei.

An additional improvement on the Super Magic Echo′ sequence attempts to refocus the Zeeman Hamiltonian $\mathcal{H}_Z$ at the same time as the dipolar Hamiltonian $\mathcal{H}_{zz}$ to produce an even larger echo in the data (Figure 11.2)

$$\text{Super Magic Echo}'' : \left\{[\tau - 180_{\bar{X}} - 2\tau - 180_X - \tau]^n\right\} 90_{\bar{X}} - t_{f1} - 180_Y.$$

The choice of the opposite phase for the 90 degree pulse stalls the refocussing of the Zeeman Hamiltonian for a time t_{f1} after the 180_Y pulse much like the usual Hahn Echo. The delay time t_{f1} is chosen to match the time that the dipolar Hamiltonian is refocused.

For a perfect second averaging of the APCP sequence to equation (11.12), the dipolar Hamiltonian should refocus at a time

$$\frac{1}{t_c}(2\tau - \frac{t_p}{2})t_{\text{burst}} \tag{11.13}$$

after the 90 degree pulse where $t_{\text{burst}} = nt_c$ is the total time of the APCP burst. However, in practice, the timing is slightly shifted due to higher order corrections and possible experimental artifacts [67].

In principle, the Super Magic Echo could be formed using any of the four pulse sequences we have previously described in place of the APCP burst.

$$\begin{aligned}
\mathrm{SME-CP}: &\quad \left\{[\tau - 180_X - 2\tau - 180_X - \tau]^n\right\} 90_Y \\
\mathrm{SME-APCP}: &\quad \left\{[\tau - 180_{\bar{X}} - 2\tau - 180_X - \tau]^n\right\} 90_X \\
\mathrm{SME-CPMG}: &\quad \left\{[\tau - 180_Y - 2\tau - 180_Y - \tau]^n\right\} 90_X \\
\mathrm{SME-APCPMG}: &\quad \left\{[\tau - 180_{\bar{Y}} - 2\tau - 180_Y - \tau]^n\right\} 90_Y .
\end{aligned}$$

Simulation of these sequences is shown in Figure 11.3. For $\tau \rightarrow 0$, the SME-CP and the SME-CPMG simplify to the Lee-Goldberg Magic Echo. Although all four of these effects are observed in simulations, they have yet to be experimentally observed, particularly SME-CP and SME-CPMG [16, 67] .

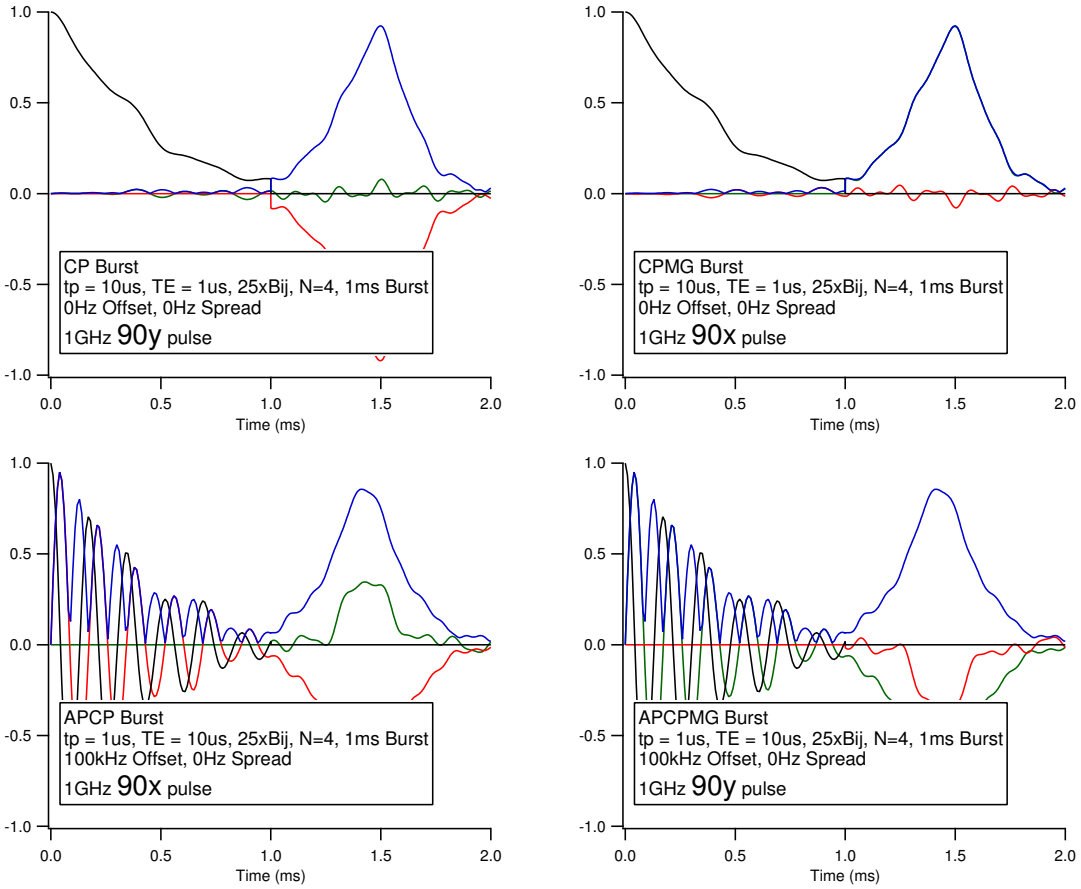

Figure 11.3: Simulations of the Super Magic Echo for the four pulse sequences CP, CPMG, APCP, and APCPMG. The spin system is initially set at equilibrium $\rho(0) = I_{z_T}/(2^{N-2})$ at $t = 0$. For $0 < t < 1$ ms, a burst of π pulses is applied with pulse spacing TE=2τ and pulse duration t_p as given in each legend. The burst time is simulated using the average Hamiltonian for that sequence $\bar{\mathcal{H}}^{(0)} + \bar{\mathcal{H}}^{(1)}$. Immediately following the burst, a $\pi/2$ pulse is applied with a special phase to convert $\mathcal{H}_{xx} \rightarrow \mathcal{H}_{zz}$ for CP and APCPMG or $\mathcal{H}_{yy} \rightarrow \mathcal{H}_{zz}$ for CPMG and APCP. After a delay that depends on t_p, τ, and Ω_z in the burst, the Super Magic Echo is formed. In each graph red is $\langle I_x \rangle$, green is $\langle I_y \rangle$, blue is $\sqrt{\langle I_x \rangle^2 + \langle I_y \rangle^2}$, and black is $\langle I_z \rangle$.

Chapter 12

Implications for Quantum Computation

Pulse action is crucial for many fields of study such as nuclear magnetic resonance (NMR), electron spin resonance (ESR), magnetic resonance imaging (MRI), and quantum information processing (QIP). In these fields, approximating a real pulse as a delta-function with infinite amplitude and infinitesimal duration is a common practice when the pulses are much stronger than the spectral width of the system under study [79, 1, 55, 18, 28, 22]. Delta-function π pulses, in particular, play a key role in bang-bang control, [93] an important technique designed to isolate qubits from their environments [88, 59, 8, 19, 90].

In real experiments, all pulses are finite in amplitude and have nonzero duration. Nevertheless, for pulse sequences with a large number of $\pi/2$ pulses, [62, 64] such as in NMR line-narrowing sequences [28, 51, 55, 69, 70, 68, 98], using the delta-function pulse approximation yields qualitatively correct predictions. Furthermore, a more rigorous analysis that includes finite pulse effects only introduces relatively small quantitative corrections [55]. For this reason, reports [45, 14, 21, 39, 48, 97] of finite pulse effects in dipolar solids including ^{29}Si in silicon, ^{13}C in C_{60}, ^{89}Y in Y_2O_3, and electrons in Si:P are surprising. In all of these studies, multiple high-powered π pulses much stronger than both the spread of Zeeman energies and the dipolar coupling were used, yet the delta-function pulse approximation failed to predict the observed behavior. The missing key ingredient is the action of time-dependent terms during the real π pulse.

We have shown experimental evidence of pulse sensitivity in dipolar solids for a variety of samples and experimental conditions. We find that the spin system is intrinsically sensitive to the phase and presence of real finite pulses even when these pulses are much stronger

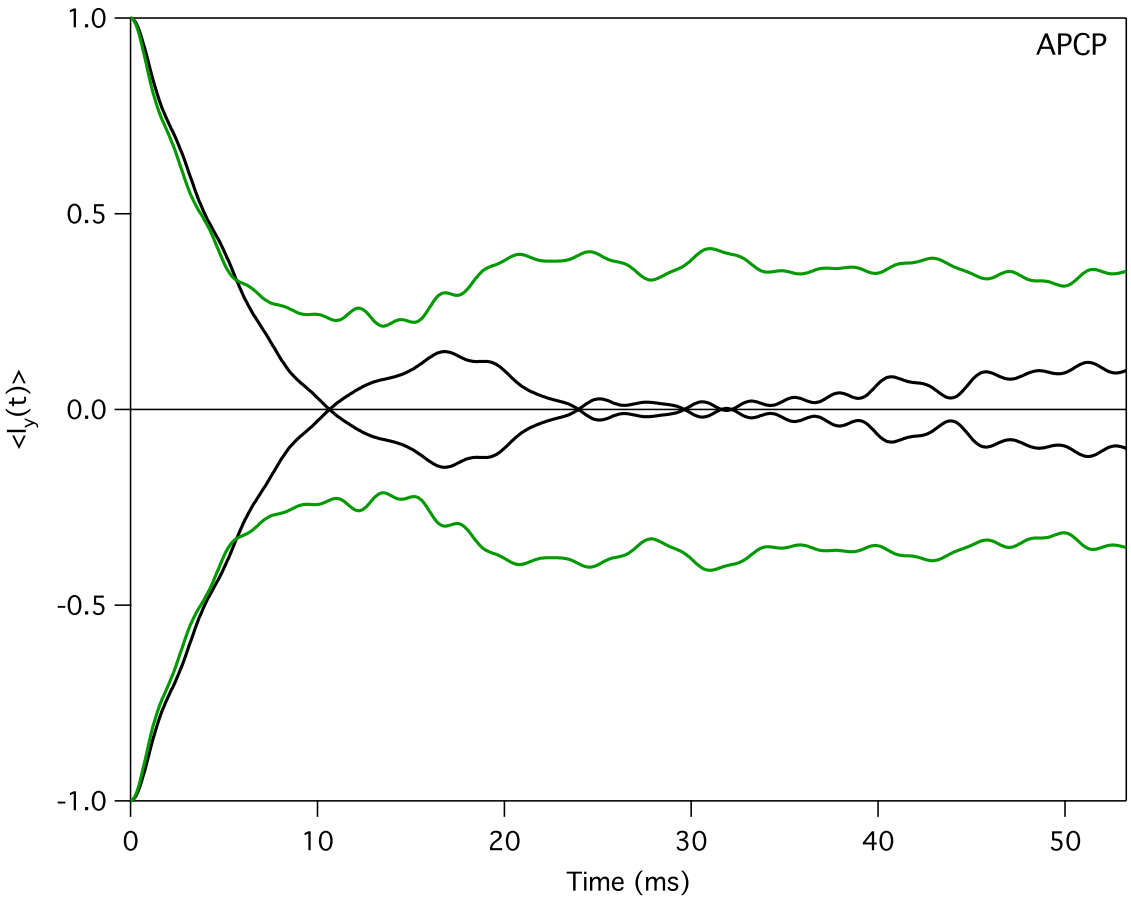

Figure 12.1: Calculations for APCP with $N = 4$, Ω_z drawn from a 290 Hz wide Gaussian, $1 \times B_{jk}$ of ^{29}Si in silicon, H_1 = 1.5 MHz, $2\tau = 2$ μs, and 100 DR average. Even for H_1/FWHM = 5000, the delta-function pulse approximation (black) misses important physics from the exact calculation (green).

than the spectral linewidth. Furthermore, exact calculations show this pulse sequence sensitivity in small clusters of spins with large coupling strength. We suggest that our findings should apply to large numbers of spins with weaker coupling based on a phenomenological scaling of our exact results. The results of the exact calculation and average Hamiltonian analysis show that no extrinsic effects are needed to describe the phenomena.

Conventional expectations from NMR theory suggest that the delta-function pulse approximation is applicable when the pulse is much stronger than the spread of Zeeman energies ($\omega_1 \gg \Omega_z$) and much stronger than the coupling strength ($\omega_1 \gg B_{jk}$). However, we have conclusively shown that the delta-function pulse approximation misses important

physics for any real pulse in the presence of an always-on internal Hamiltonian. These effects are especially pronounced when considering the action of π pulses since the unique pulse-dependent terms have no analog in the delta-function pulse approximation [45].

Simply ignoring the intrinsic effects under real finite pulses can lead to dramatic consequences as shown in Figure 12. The green trace shows the exact calculation of $\langle I_{y_1}(t)\rangle$ for the APCP sequence under the action of finite pulses. The black trace is the same calculation but where we have artificially set the internal Hamiltonian to zero during the pulses. It is particularly alarming to note that we have used a pulse strength that is 5000 times stronger than the full-width-at-half-maximum of the NMR spectrum, yet the two curves do not agree. The delta-function pulse approximation is therefore a completely invalid assumption, at least in the limit of many spins, many π pulses, or both.

Our findings have an important connection to the field of quantum information processing since many quantum algorithms call for the application of repeated π pulses to a quantum system [88, 59, 8, 19, 90, 93]. Typically, the delta-function pulse approximation is used in the analysis. In order to salvage these schemes, the internal Hamiltonian must be completely set to zero during the action of any real pulse. It is not enough to simply reduce the coupling strength even by an order of magnitude. Furthermore, any effective transverse field during the pulses will also change the system's expected response after many pulses are applied. The effects of real pulses need to be taken into account if the promise of quantum control is to be realized.

Glossary of Terms

T_1	Spin-lattice relaxation time	10
T_2	Transverse relaxation time	10
$T_2^\star$	Extrinsic relaxation time caused by static field inhomogeneities	36
$\hbar$	Planck's constant	11
$\rho(t)$	The Density Matrix as a function of time	15
HE	Hahn Echo	29
FFT	Fast Fourier Transform	25
CP	Carr-Purcell multiple π pulse sequence	32
CPMG	Carr-Purcell-Meiboom-Gill multiple π pulse sequence	32
APCP	Alternating-Phase CP multiple π pulse sequence	32
APCPMG	Alternating-Phase CPMG multiple π pulse sequence	32
SEn	Spin Echo number n	36
STEa	Anomalous Stimulated Echo	42
B^{ext}	Externally applied magnetic field	44
B^{loc}	Local magnetic field on the microscopic scale	44
FID	Free Induction Decay	46

Bibliography

[1] A. Abragam. *The principles of nuclear magnetism*. The International series of monographs on physics. Clarendon Press, Oxford, 1983.

[2] A. Allerhand. Analysis of carr-purcell spin-echo nmr experiments on multiple-spin systems i. the effect of homonuclear coupling. *Journal of Chemical Physics*, 44(1):1, 1966.

[3] H. Alloul and P. Dellouve. Spin localization in s-p - direct evidence from p-31 nuclear-magnetic-resonance. *Physical Review Letters*, 59(5):578–581, 1987.

[4] George B. Arfken and Hans-Jurgen Weber. *Mathematical methods for physicists*. Elsevier, Boston, 6th edition, 2005.

[5] D. Barnaal and I. J. Lowe. Effects of rotating magnetic fields on free-induction decay shapes. *Physical Review Letters*, 11(6):258, 1963.

[6] E. Belorizky, W. Gorecki, M. Jeannin, P. H. Fries, P. Maldivi, and E. Gout. Sample-shape dependence of the inhomogeneous nmr line broadening and line shift in diamagnetic liquids. *Chemical Physics Letters*, 175(6):579–584, 1990.

[7] D. Burstein. Stimulated echoes: Description, applications, practical hints. *Concepts in Magnetic Resonance*, 8(4):269–278, 1996.

[8] P. Cappellaro, J. S. Hodges, T. F. Havel, and D. G. Cory. Principles of control for decoherence-free subsystems. *Journal of Chemical Physics*, 125(4):10, 2006.

[9] H. Y. Carr and E. M. Purcell. Effects of diffusion on free precession in nuclear magnetic resonance experiments. *Physical Review*, 94(3):630–638, 1954.

[10] J. R. Carson. Wave propagation over parallel wires - the proximity effect. *Philosophical Magazine*, 41(244):607–633, 1921.

[11] H. Cho, T. D. Ladd, J. Baugh, D. G. Cory, and C. Ramanathan. Multispin dynamics of the solid-state nmr free induction decay. *Physical Review B*, 72(5):6, 2005.

[12] D. C. Cronemeyer. Demagnetization factors for general ellipsoids. *Journal of Applied Physics*, 70(6):2911–2914, 1991.

[13] H. K. Cummins, G. Llewellyn, and J. A. Jones. Tackling systematic errors in quantum logic gates with composite rotations. *Physical Review A*, 67(4):7, 2003.

[14] A. E. Dementyev, D. Li, K. MacLean, and S. E. Barrett. Anomalies in the nmr of silicon: Unexpected spin echoes in a dilute dipolar solid. *Physical Review B*, 68(15):4, 2003.

[15] D. P. DiVincenzo and D. Loss. Quantum computers and quantum coherence. *Journal of Magnetism and Magnetic Materials*, 200(1-3):202–218, 1999.

[16] Yanqun Dong, Dale Li, R. Ramos, and S. E. Barrett. Theoretical approaches to understanding the finite π pulse. unpublished.

[17] L. E. Drain. Broadening of magnetic resonance lines due to field inhomogeneities in powdered samples. *Proceedings of the Physical Society of London*, 80(518):1380, 1962.

[18] Richard R. Ernst, Geoffrey Bodenhausen, and Alexander Wokaun. *Principles of nuclear magnetic resonance in one and two dimensions*, volume 14. Clarendon Press, Oxford, 1987.

[19] P. Facchi, S. Tasaki, S. Pascazio, H. Nakazato, A. Tokuse, and D. A. Lidar. Control of decoherence: Analysis and comparison of three different strategies. *Physical Review A*, 71(2):22, 2005.

[20] E. B. Fel'dman and S. Lacelle. Configurational averaging of dipolar interactions in magnetically diluted spin networks. *Journal of Chemical Physics*, 104(5):2000–2009, 1996.

[21] M. B. Franzoni and P. R. Levstein. Manifestations of the absence of spin diffusion in multipulse nmr experiments on diluted dipolar solids. *Physical Review B*, 72(23):5, 2005.

[22] Ray Freeman. *Spin choreography : basic steps in high resolution NMR*. Spektrum, Oxford, 1997.

[23] Eiichi Fukushima and Stephen B.W Roeder. *Experimental pulse NMR : a nuts and bolts approach*. Addison-Wesley Pub. Co., Advanced Book Program, Reading, Mass., 1981.

[24] S. E. Fuller, E. M. Meintjes, and W. W. Warren. Impurity nmr study of the acceptor band in si(b). *Physical Review Letters*, 76(15):2806–2809, 1996.

[25] T. Gullion, D. B. Baker, and M. S. Conradi. New, compensated carr-purcell sequences. *Journal of Magnetic Resonance*, 89(3):479–484, 1990.

[26] U. Haeberlen, J. D. Ellett, and J. S. Waugh. Resonance offset effects in multiple-pulse nmr experiments. *Journal of Chemical Physics*, 55(1):53, 1971.

[27] U. Haeberlen and J. S. Waugh. Coherent averaging effects in magnetic resonance. *Physical Review*, 175(2):453, 1968.

[28] Ulrich Haeberlen. *High resolution NMR in solids : selective averaging*, volume 1. Academic Press, New York, 1976.

[29] E. L. Hahn. Spin echoes. *Physical Review*, 80(4):580–594, 1950.

[30] D. I. Hoult. Nmr receiver - description and analysis of design. *Progress in Nuclear Magnetic Resonance Spectroscopy*, 12:41–77, 1978.

[31] S. Hudgens, M. Kastner, and H. Fritzsche. Diamagnetic susceptibility of tetrahedral semiconductors. *Physical Review Letters*, 33(26):1552–1555, 1974.

[32] M. D. Hurlimann and D. D. Griffin. Spin dynamics of carr-purcell-meiboom-gill-like sequences in grossly inhomogeneous b-o and b-1 fields and application to nmr well logging. *Journal of Magnetic Resonance*, 143(1):120–135, 2000.

[33] John David Jackson. *Classical electrodynamics*. Wiley, New York, 3rd ed edition, 1999.

[34] B. E. Kane. A silicon-based nuclear spin quantum computer. *Nature*, 393(6681):133–137, 1998.

[35] B. E. Kane. Silicon-based quantum computation. *Fortschritte Der Physik-Progress of Physics*, 48(9-11):1023–1041, 2000.

[36] P. A. Keifer. 90 degrees pulse width calibrations: How to read a pulse width array. *Concepts in Magnetic Resonance*, 11(3):165–180, 1999.

[37] S. Lacelle and L. Tremblay. Dipolar interactions in magnetically very diluted spin networks. *Journal of Chemical Physics*, 102(2):947–955, 1995.

[38] T. D. Ladd, J. R. Goldman, F. Yamaguchi, Y. Yamamoto, E. Abe, and K. M. Itoh. All-silicon quantum computer. *Physical Review Letters*, 89(1):4, 2002.

[39] T. D. Ladd, D. Maryenko, Y. Yamamoto, E. Abe, and K. M. Itoh. Coherence time of decoupled nuclear spins in silicon. *Physical Review B*, 71(1):12, 2005.

[40] G. Lampel. Nuclear dynamic polarization by optical electronic saturation and optical pumping in semiconductors. *Physical Review Letters*, 20(10):491, 1968.

[41] Moses Lee and Walter I. Goldburg. Nuclear-magnetic-resonance line narrowing by a rotating rf field. *Physical Review*, 140:A1261, 1965.

[42] S. Lee, W. Richter, S. Vathyam, and W. S. Warren. Quantum treatment of the effects of dipole-dipole interactions in liquid nuclear magnetic resonance. *Journal of Chemical Physics*, 105(3):874–900, 1996.

[43] M. H. Levitt. Composite pulses. *Progress in Nuclear Magnetic Resonance Spectroscopy*, 18:61–122, 1986.

[44] M. H. Levitt and R. Freeman. Nmr population-inversion using a composite pulse. *Journal of Magnetic Resonance*, 33(2):473–476, 1979.

[45] Dale Li, A. E. Dementyev, Yanqun Dong, R. Ramos, and S. E. Barrett. Generating unexpected spin echoes in dipolar solids with π pulses. *Physical Review Letters*, 98(19):190401, 2007.

[46] Dale Li, Yanqun Dong, Rona G. Ramos, John D. Murray, Kenneth MacLean, Anatoly E. Dementyev, and Sean E. Barrett. The intrinsic origin of spin echoes in dipolar solids generated by strong π pulses. Submitted to Physical Review B, 2007.

[47] I. J. Lowe and R. E. Norberg. Free-induction decays in solids. *Physical Review*, 107(1):46–61, 1957.

[48] S. A. Lyon. Si:p esr cpmg. private communication.

[49] D. E. Maclaughlin. Suppression of nutation angle variation in pulsed nuclear magnetic resonance. *Review of Scientific Instruments*, 41(8):1202, 1970.

[50] W. Magnus. On the exponential solution of differential equations for a linear operator. *Communications on Pure and Applied Mathematics*, 7(4):649–673, 1954.

[51] P. Mansfield. Symmetrized pulse sequences in high resolution nmr in solids. *Journal of Physics Part C Solid State Physics*, 4(11):1444, 1971.

[52] M. M. Maricq. Application of average hamiltonian theory to the nmr of solids. *Physical Review B*, 25(11):6622–6632, 1982.

[53] M. M. Maricq. Thermodynamics for many-body systems evolving under a periodic time-dependent hamiltonian - application to pulsed magnetic-resonance. *Physical Review B*, 31(1):127–141, 1985.

[54] M. M. Maricq. Equilibrium in periodically time-dependent 2-level systems. *Physical Review Letters*, 56(14):1433–1436, 1986.

[55] M. Mehring. *Principles of high-resolution NMR in solids*. Springer-Verlag, Berlin, 2nd, rev. and enl. ed edition, 1983.

[56] M. Mehring and G. Sinning. Dynamics of heteronuclear spin coupling and decoupling in solids. *Physical Review B*, 15(5):2519–2532, 1977.

[57] M. Mehring and J. S. Waugh. Phase transients in pulsed nmr spectrometers. *Review of Scientific Instruments*, 43(4):649, 1972.

[58] S. Meiboom and D. Gill. Modified spin-echo method for measuring nuclear relaxation times. *Review of Scientific Instruments*, 29(8):688–691, 1958.

[59] J. J. L. Morton, A. M. Tyryshkin, A. Ardavan, S. C. Benjamin, K. Porfyrakis, S. A. Lyon, and G. A. D. Briggs. The n@c-60 nuclear spin qubit: Bang-bang decoupling and ultrafast phase gates. *Physica Status Solidi B-Basic Solid State Physics*, 243(13):3028–3031, 2006.

[60] G. Mozurkewich, H. I. Ringermacher, and D. I. Bolef. Effect of demagnetization on magnetic-resonance line-shapes in bulk samples - application to tungsten. *Physical Review B*, 20(1):33–38, 1979.

[61] J. A. Osborn. Demagnetizing factors of the general ellipsoid. *Physical Review*, 67(11-1):351–357, 1945.

[62] E. D. Ostroff and J. S. Waugh. Multiple spin echoes and spin locking in solids. *Physical Review Letters*, 16(24):1097, 1966.

[63] A. Pines and J. S. Waugh. Quantitative aspects of coherent averaging - simple treatment of resonance offset processes in multiple-pulse nmr. *Journal of Magnetic Resonance*, 8(4):354, 1972.

[64] J. G. Powles and P. Mansfield. Double-pulse nuclear-resonance transients in solids. *Physics Letters*, 2(2):58–59, 1962.

[65] V. Privman, I. D. Vagner, and G. Kventsel. Quantum computation in quantum-hall systems. *Physics Letters A*, 239(3):141–146, 1998.

[66] Edward M Purcell. *Electricity and magnetism*, volume v. 2 of *Berkeley physics course*. McGraw-Hill, New York, 2nd ed edition, 1985.

[67] R. Ramos, Dale Li, Yanqun Dong, and S. E. Barrett. Advanced pulse sequences exploiting the time-dependence of real pulses. unpublished.

[68] W. K. Rhim, D. D. Elleman, and R. W. Vaughan. Enhanced resolution for solid-state nmr. *Journal of Chemical Physics*, 58(4):1772–1773, 1973.

[69] W. K. Rhim, A. Pines, and J. S. Waugh. Violation of spin-temperature hypothesis. *Physical Review Letters*, 25(4):218, 1970.

[70] W. K. Rhim, A. Pines, and J. S. Waugh. Time-reversal experiments in dipolar-coupled spin systems. *Physical Review B*, 3(3):684, 1971.

[71] D. Rugar, R. Budakaian, H.J. Mamin, and B.W. Chui. Single spin detection by magnetic resonance force microscopy. *Nature*, 430:329–332, 2004.

[72] D. Sakellariou, P. Hodgkinson, and L. Emsley. Quasi equilibria in solid-state nmr. *Chemical Physics Letters*, 293(1-2):110–118, 1998.

[73] D. Sakellariou, P. Hodgkinson, S. Hediger, and L. Emsley. Experimental observation of periodic quasi-equilibria in solid-state nmr. *Chemical Physics Letters*, 308(5-6):381–389, 1999.

[74] J. J Sakurai and San Fu Tuan. *Modern quantum mechanics*. Addison-Wesley Pub. Co., Reading, Mass., rev. ed edition, 1994.

[75] A. Samoson, T. Tuherm, and Z. Gan. High-field high-speed mas resolution enhancement in h-1 nmr spectroscopy of solids. *Solid State Nuclear Magnetic Resonance*, 20(3-4):130–136, 2001.

[76] A. J. Shaka, S. P. Rucker, and A. Pines. Iterative carr-purcell trains. *Journal of Magnetic Resonance*, 77(3):606–611, 1988.

[77] P. V. Sharma. Rapid computation of magnetic anomalies and demagnetization effects caused by bodies of arbitrary shape. *Pure and Applied Geophysics*, 64(2):89, 1966.

[78] R. G. Shulman and B. J. Wyluda. Nuclear magnetic resonance of si-29 in n-type and p-type silicon. *Physical Review*, 103(4):1127–1129, 1956.

[79] Charles P. Slichter. *Principles of magnetic resonance*, volume 1. Springer, Berlin, 3rd enl. and updated ed edition, 1996.

[80] I. Solomon. Rotary spin echoes. *Physical Review Letters*, 2(7):301–302, 1959.

[81] O. W. Sorensen, G. W. Eich, M. H. Levitt, G. Bodenhausen, and R. R. Ernst. Product operator-formalism for the description of nmr pulse experiments. *Progress in Nuclear Magnetic Resonance Spectroscopy*, 16:163–192, 1983.

[82] R. K. Sundfors and D. F. Holcomb. Nuclear magnetic resonance studies of metallic transition in doped silicon. *Physical Review A*, 136(3A):A810, 1964.

[83] D. Suwelack and J. S. Waugh. Quasistationary magnetization in pulsed spin-locking experiments in dipolar solids. *Physical Review B*, 22(11):5110–5114, 1980.

[84] Frederick Emmons Terman. *Radio engineers' handbook*. McGraw-Hill Book Company, inc., New York, 1st ed edition, 1943.

[85] H. C. Torrey. Transient nutations in nuclear magnetic resonance. *Physical Review*, 76(8):1059–1068, 1949.

[86] R. Tycko, R. C. Haddon, G. Dabbagh, S. H. Glarum, D. C. Douglass, and A. M. Mujsce. Solid-state magnetic-resonance spectroscopy of fullerenes. *Journal of Physical Chemistry*, 95(2):518–520, 1991.

[87] R. Tycko, E. Schneider, and A. Pines. Broad-band population-inversion in solid-state nmr. *Journal of Chemical Physics*, 81(2):680–688, 1984.

[88] G. S. Uhrig. Keeping a quantum bit alive by optimized pi-pulse sequences. *Physical Review Letters*, 98(10):4, 2007.

[89] J. H. Van Vleck. The dipolar broadening of magnetic resonance lines in crystals. *Physical Review*, 74(9):1168–1183, 1948.

[90] L. M. K. Vandersypen and I. L. Chuang. Nmr techniques for quantum control and computation. *Reviews of Modern Physics*, 76(4):1037–1069, 2004.

[91] R. W. Vaughan, L. M. Stacey, J. W. Lee, D. D. Elleman, and W. K. Rhim. A simple, low-power, multiple pulse nmr spectrometer. *Review of Scientific Instruments*, 43(9):1356, 1972.

[92] A. J. Vega. Controlling the effects of pulse transients and rf inhomogeneity in phase-modulated multiple-pulse sequences for homonuclear decoupling in solid-state proton nmr. *Journal of Magnetic Resonance*, 170(1):22–41, 2004.

[93] L. Viola and S. Lloyd. Dynamical suppression of decoherence in two-state quantum systems. *Physical Review A*, 58(4):2733–2744, 1998.

[94] R. Vrijen, E. Yablonovitch, K. Wang, H. W. Jiang, A. Balandin, V. Roychowdhury, T. Mor, and D. DiVincenzo. Electron-spin-resonance transistors for quantum computing in silicon-germanium heterostructures. *Physical Review A*, 62(1):art. no.–012306, 2000.

[95] J. D. Walls and Y. Y. Lin. Constants of motion in nmr spectroscopy. *Solid State Nuclear Magnetic Resonance*, 29(1-3):22–29, 2006.

[96] W. S. Warren, W. Richter, A. H. Andreotti, and B. T. Farmer. Generation of impossible cross-peaks between bulk water and biomolecules in solution nmr. *Science*, 262(5142):2005–2009, 1993.

[97] S. Watanabe and S. Sasaki. Si-29 nuclear-spin decoherence process directly observed by multiple spin-echoes for pure and carrier-less silicon. *Japanese Journal of Applied Physics Part 2-Letters*, 42(11B):L1350–L1352, 2003.

[98] J. S. Waugh, L. M. Huber, and Haeberle.U. Approach to high-resolution nmr in solids. *Physical Review Letters*, 20(5):180, 1968.

[99] S. Wimperis. Broad-band, narrow-band, and passband composite pulses for use in advanced nmr experiments. *Journal of Magnetic Resonance Series A*, 109(2):221–231, 1994.

[100] C. S. Yannoni, R. D. Johnson, G. Meijer, D. S. Bethune, and J. R. Salem. C-13 nmr-study of the c60 cluster in the solid-state - molecular-motion and carbon chemical-shift anisotropy. *Journal of Physical Chemistry*, 95(1):9–10, 1991.

[101] W. X. Zhang, N. Konstantinidis, K. A. Al-Hassanieh, and V. V. Dobrovitski. Modelling decoherence in quantum spin systems. *Journal of Physics-Condensed Matter*, 19(8):28, 2007.